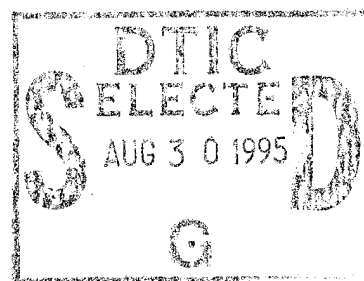


**Woods Hole
Oceanographic
Institution**



**Collection and Processing of Shipboard ADCP velocities from
the Barents Sea Polar Front Experiment**

by

Carolyn L. Harris, Albert J. Plueddemann, Robert H. Bourke,
Marla D. Stone and Richard A. Pawlowicz

January 1995

Technical Report

Funding was provided by the Office of Naval Research under
Grant No. N00014-90-J-1359.

Approved for public release; distribution unlimited.

19950828 015

DTIC QUALITY INSPECTED 8

WHOI-95-03

**Collection and Processing of Shipboard ADCP velocities from the Barents Sea
Polar Front Experiment**

by

Carolyn L. Harris, Albert J. Plueddemann, Robert H. Bourke,
Marla D. Stone and Richard A. Pawlowicz

Woods Hole Oceanographic Institution
Woods Hole, Massachusetts 02543

January 1995

Technical Report

Funding was provided by the Office of Naval Research under
Grant No. N00014-90-J-1359.

Reproduction in whole or in part is permitted for any purpose of the United States
Government. This report should be cited as Woods Hole Oceanog. Inst. Tech. Rept.,
WHOI-95-03.

Approved for public release; distribution unlimited.

Approved for Distribution:



Philip L. Richardson, Chair
Department of Physical Oceanography

Abstract

The Barents Sea Polar Front Experiment was a combined physical oceanography and acoustic tomography field study which took place from 6-26 August 1992. Both shipboard and moored data were collected in a 80 x 70 km experimental region on the south flank of Spitsbergen Bank about 60 km east of Bear Island. Of principal interest in this report are the data from an Acoustic Doppler Current Profiler (ADCP) which was operated continuously during the experimental period as a part of the shipboard instrumentation aboard the USNS BARTLETT. The data from eight current meters deployed on three moorings in the experimental region are used to supplement the ADCP analysis. Preliminary results showed that velocities in the experimental region were dominated by semi-diurnal tides. The strong tidal oscillations dictated the use of a tide removal scheme to extract a steady flow component from the space-time grid of ADCP velocities. This report describes the configuration and operation of the ADCP, the space-time sampling grid on which the data were collected, the determination of absolute velocity from the ADCP measurements, and the application and results of a tide removal technique which allowed estimation of the sub-tidal flow.

Accession For	
NTIS	CRA&I <input checked="" type="checkbox"/>
DTIC	TAB <input type="checkbox"/>
Unannounced <input type="checkbox"/>	
Justification	
By	
Distribution /	
Availability Codes	
Dist	Avail and/or Special
A-1	

Contents

Abstract	1
List of Figures	3
List of Tables	5
1 Introduction	6
2 Data collection	10
2.1 Bathymetry	10
2.2 The BARTLETT cruise track	10
3 Determination of absolute velocity	17
3.1 Initial data processing	17
3.2 Absolute velocity	17
3.3 Absolute velocity error estimates	19
4 Determination of sub-tidal flow	25
4.1 Current meter data	25
4.2 ADCP data	35
4.3 Combined current meter and ADCP data	51
4.4 Sub-tidal error estimates	64
Acknowledgments	70
References	71

List of Figures

1	The western Barents Sea	8
2	Regional bathymetry	11
3	Survey plan views	13
4	Absolute water velocities	20
5	Plan views of ADCP absolute velocity	22
6	Current meter velocities from 20 m depth	26
7	Current meter model tidal ellipses from 20 m depth	27
8	Current meter model tidal phases from 20 m depth	28
9	Current meter velocities from 50 m depth	29
10	Current meter model tidal ellipses from 50 m depth	30
11	Current meter model tidal phases from 50 m depth	31
12	Depth averaged current meter velocities	32
13	Depth averaged current meter model tidal ellipses	33
14	Depth averaged current meter model tidal phases	34
15	ADCP/current meter data comparison	37
16	ADCP velocities from 20 m depth	39
17	ADCP model tidal ellipses from 20 m depth	40
18	ADCP model tidal phases from 20 m depth	41
19	ADCP velocities from 50 m depth	42
20	ADCP model tidal ellipses from 50 m depth	43
21	ADCP model tidal phases from 50 m depth	44
22	ADCP velocities from 80 m depth	45
23	ADCP model tidal ellipses from 80 m depth	46
24	ADCP model tidal phases from 80 m depth	47
25	Depth averaged ADCP velocities	48
26	Depth averaged ADCP model tidal ellipses	49

27	Depth averaged ADCP model tidal phases	50
28	ADCP and current meter velocities from 20 m depth	52
29	ADCP and current meter model tidal ellipses from 20 m depth	53
30	ADCP and current meter model tidal phases from 20 m depth	54
31	ADCP and current meter velocities from 50 m depth	55
32	ADCP and current meter model tidal ellipses from 50 m depth	56
33	ADCP and current meter model tidal phases from 50 m depth	57
34	ADCP and current meter velocities from 80 m depth	58
35	ADCP and current meter model tidal ellipses from 80 m depth	59
36	ADCP and current meter model tidal phases from 80 m depth	60
37	Depth averaged ADCP and current meter velocities	61
38	Depth averaged ADCP and current meter model tidal ellipses	62
39	Depth averaged ADCP and current meter model tidal phases	63
40	Observed and modelled power spectral density	66
41	Current meter sub-tidal standard errors	67
42	ADCP sub-tidal standard errors	68
43	ADCP and current meter sub-tidal standard errors	69

List of Tables

1	ADCP parameter settings	9
2	CTD sampling	12
3	Model polynomial misfit	38

1 Introduction

A coordinated physical oceanographic and acoustic field study of the Barents Sea Polar Front (BSPF) was conducted in the summer of 1992 under the sponsorship of the Office of Naval Research. The goals of the work were to provide a detailed physical description of the front, to improve understanding of frontal dynamics, and to investigate acoustic propagation and tomographic methods in a region with a shallow, sloping bottom. The experiment took place between 6 and 26 August 1992 within a 80 x 70 km region centered on the southern slope of Spitsbergen Bank, about 60 km east of Bear Island (Figure 1).

The principal platforms for the field work were the USNS BARTLETT and four moorings. The BARTLETT performed a series of hydrographic surveys using a profiling Conductivity, Temperature, Depth (CTD) system and an Acoustic Doppler Current Profiler (ADCP). Three sub-surface moorings were deployed near the northeast (NE), northwest (NW), and southwest (SW) corners of the survey area and served as platforms for nine current meters at nominal depths of 20, 50, and 80 m. The moored instrumentation included four Neil Brown Acoustic Current Meters (22 and 52 m at NE, 19 m at NW, 20 m at SW) and five Aanderaa RCM-8 current meters (82 m at NE, 49 and 159 m at NW, 50 and 80 m at SW). The data from 159 m on the NW mooring were not usable due to a mechanical problem with the instrument. The three current meter moorings were also used as platforms for two 400 Hz acoustic transceivers and a 224 Hz acoustic source. A fourth mooring was dedicated to a vertical hydrophone array. The acoustic propagation measurements and tomographic analyses from these deployments will not be discussed here.

Of principal interest in this report are the data from the shipboard ADCP (the moored current meter data are used for comparative purposes at several stages of the ADCP data analysis). The BARTLETT was outfitted with a 300 kHz ADCP manufactured by RD Instruments. Originally configured as a self-contained unit, the ADCP was converted to vessel mount operation for the field program and installed in the ship's well with the transducers at a depth of 4 m below the waterline. The complete ADCP installation included an IBM-PC compatible computer, a Magnavox MX4200 Global Positioning System (GPS) receiver and hardware interfaces to connect the ADCP, the GPS receiver, and the ship's gyro-compass to the computer. Data Acquisition Software (DAS Ver. 2.48), a gyro-compass interface program (Head248), and a navigation interface program (Navsoft) supplied by RD Instruments were used to merge heading and position information with the ADCP data stream.

The ADCP was configured to alternate "water-track" pulses and "bottom-track" pulses within a 3 minute ensemble averaging interval. Both the transmitted pulse length and the bin length were set to nominal values of 8 m. In general these nominal values need to be corrected for the *in situ* soundspeed. However, since the

observed soundspeed in the experimental region was within 1% of the reference value of 1475 m s^{-1} used generating the nominal pulse and bin lengths, no correction was made. Thirty depth bins were recorded for each ensemble, with the center of the first and last bins at 14 m and 246 m, respectively. Velocity data corrected for tilt and converted to geographic coordinates were recorded for each ensemble, along with ship's heading and navigation data from the GPS receiver. The principal ADCP parameter settings are summarized in Table 1.

The purpose of this report is to describe the collection and processing of ship-board ADCP velocity data from the Barents Sea Polar Front Experiment. In Section 2 the regional bathymetry is described and the ship's track during the experiment is shown in a series of sub-sections. In the third section, the determination of absolute velocity from the ADCP water-track data is described. Initial processing steps included the correction of timing problems and the editing of bad points. ADCP bottom tracking, rather than GPS navigation, was used to convert the water-track velocities to absolute velocities. Thus the portion of the ship's track for which ADCP bottom tracking was available defines the space-time grid on which the velocity data were sampled. Estimates of the errors in magnitude and direction of absolute velocity are presented. In the final section, the tide removal technique of Candela *et al.* (1992) and its application are described. The technique assumes that the observations can be modelled as a temporally steady (but spatially varying) part and a sum of harmonic functions at the tidal frequencies. The coefficients of the harmonic functions may vary in space. The tide removal technique was applied first to the moored current meter data. These results were used as a "benchmark" for evaluating the the performance of the technique when applied to the ADCP data. The optimal model coefficients for use with the ADCP data were determined by minimizing the difference between the modelled flow (both tidal and steady) from the ADCP and the modelled flow from the current meters. The modelled tidal flow, the steady flow, the residuals from the model fit, and error estimates for the fitted fields are presented.

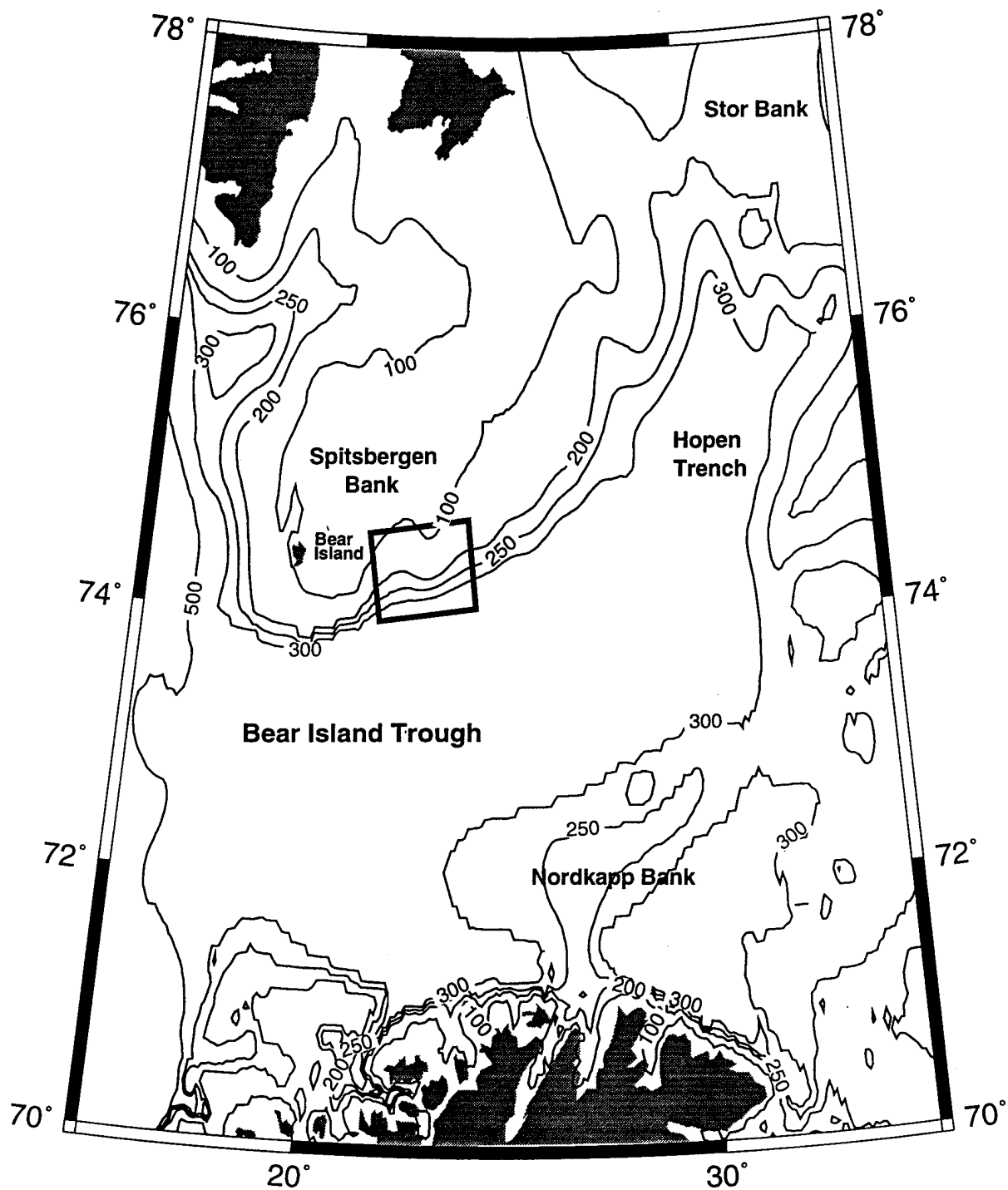


Figure 1: A map of the southwestern Barents Sea with topographic contours to highlight the major features of the basin. The rectangle encloses the 80 x 70 km experimental region.

<u>parameter</u>	<u>value</u>
DAS sample interval (sec)	180
pings per ADCP ensemble	1
number of depth bins	30
depth bin length (m)	8
transmit pulse length (m)	8
blank after transmit (m)	2
transducer depth (m)	4
pitch/roll compensation	on
heading compensation	on
bottom track	on
water track pings between bottom track pings	1
water track pings before re-acquiring bottom	80

Table 1: Principal parameter settings for the shipboard ADCP. Parameters not shown in the table were set to their default values.

2 Data collection

2.1 Bathymetry

The bathymetry for the experimental region was determined by combining data from several sources. A bottom depth was available at each CTD station from the ship's echosounder. The ADCP provided depth estimates along the ship's track with horizontal resolution of order 1 km (varying with ship speed). However, these depth estimates were not continuous since the maximum depth of successful bottom tracking (320 to 400 m) was less than the water depth in the southern part of the region. A comparison at the CTD station locations showed that the ADCP and echosounder depths agreed within a few meters for water depths less than 325 m. ADCP bottom depths in deeper water showed increasing disagreement with the echosounder depths and were not used. Additional bathymetry was extracted by hand from historical chart data (Norsk Polarinstitutt Chart 7421, 1986). Bottom depths from the echosounder, ADCP, and chart data were combined and interpolated to a 1 km grid to produce a composite bathymetry for the region. The resulting bottom topography is contoured in Figure 2. The depth increases smoothly from about 150 m to 450 m in the eastern portion of the survey area. Finger Canyon and other topographic variability result in a more complex shelf-slope transition to the west.

2.2 The BARTLETT cruise track

The cruise track was divided chronologically into four sections for presentation. These four sections correspond roughly to how the cruise track was divided for use in processing the CTD data (Table 2). Plan views of these sections are shown in Figures 3a-3d.

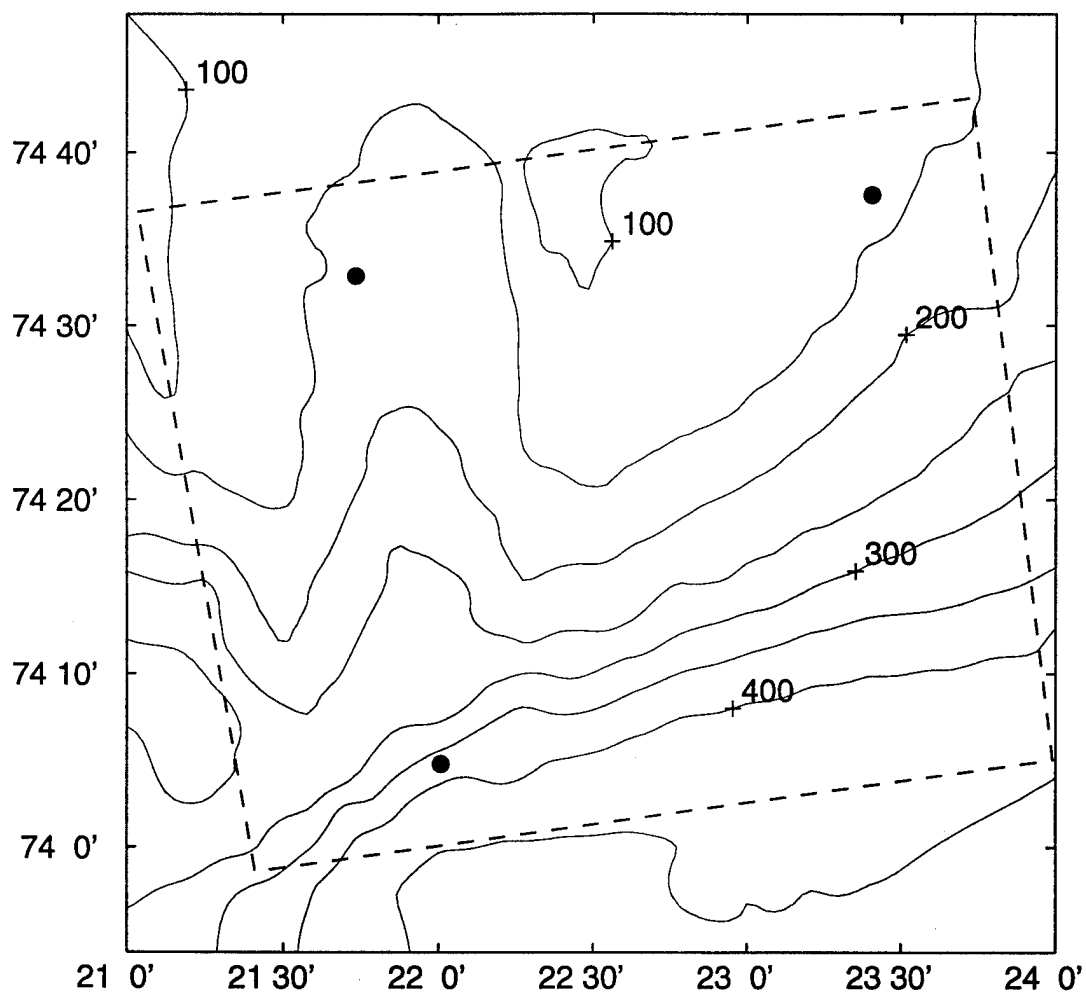


Figure 2: Contour plot of bottom topography in the region of the BSPF Experiment. Depths are shown in meters. The bathymetry is a composite of CTD station depths, ADCP bottom depths, and historical chart data. The dashed rectangle encloses the experimental area. The locations of the three current meter moorings are shown by solid circles.

section	sub-section	start	end	casts
1	Grid 1	8-06-92 2030	8-09-92 2300	72
2	Grid 2	8-10-92 0610	8-14-92 1050	58
3	Dense section	8-14-92 1200	8-15-92 0230	18
	Time series	8-17-92 0600	8-18-92 0800	27
	Grid 3	8-21-92 2050	8-23-92 0430	25
4	Grid 4	8-23-92 1445	8-26-92 1550	92

Table 2: The four cruise track sections are described in terms of the six CTD sampling sub-sections. Each cruise track section consists of one grid except section 3 which combines three CTD sub-sections: Dense section, Time series, and Grid 3. Grids 1 and 4 represent complete occupations of the nominal sampling grid; 72 CTD stations with 10 km spacing within the 80 x 70 km experimental region. Grids 2 and 3 are incomplete occupations of the nominal sampling grid. The dense section is a frontal transect with CTD stations at 2.5 km spacing. The time series is a sequence of hourly CTD casts at a fixed location (near the maximum frontal gradients). All times are UTC.

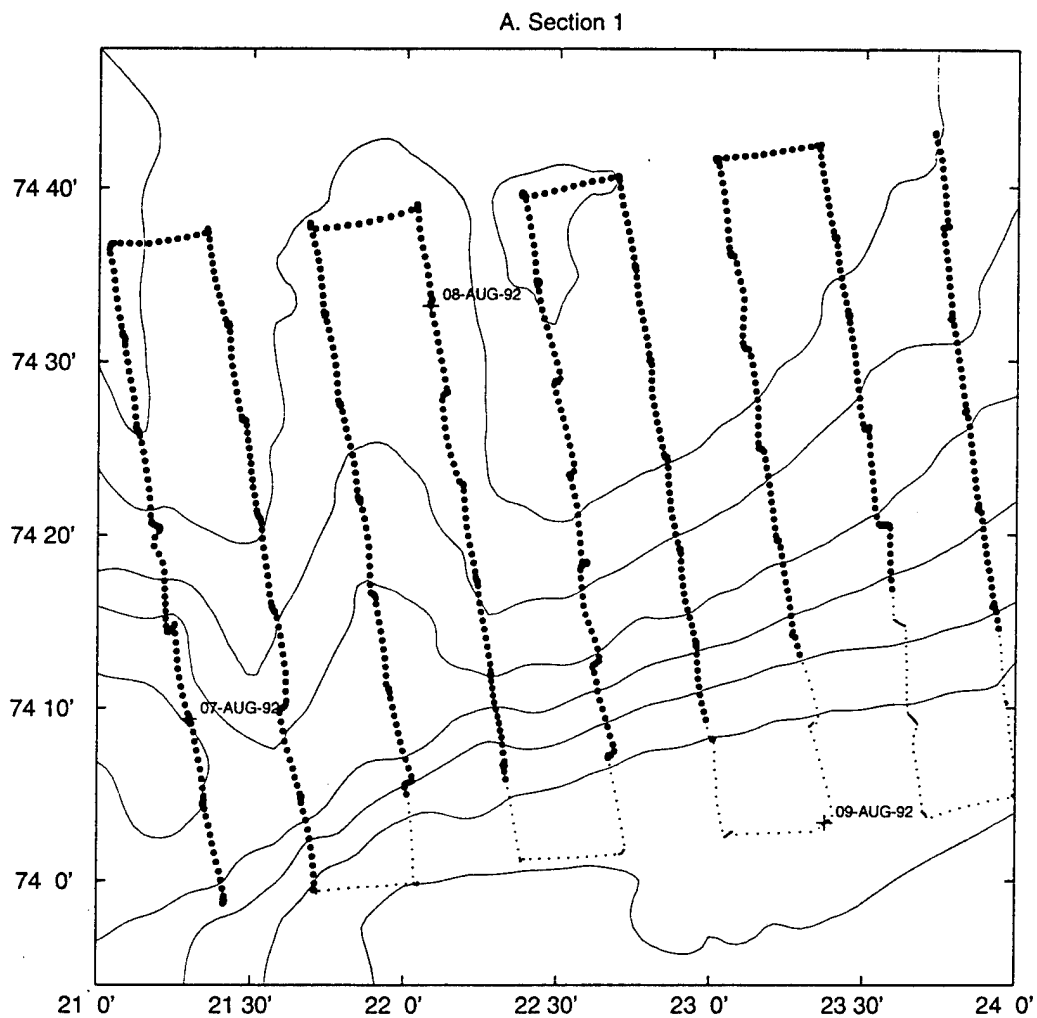


Figure 3a: Plan view of the ship's survey, section 1. Each ADCP station is shown by a small dot. A large dot represents an ADCP station with bottom tracking.

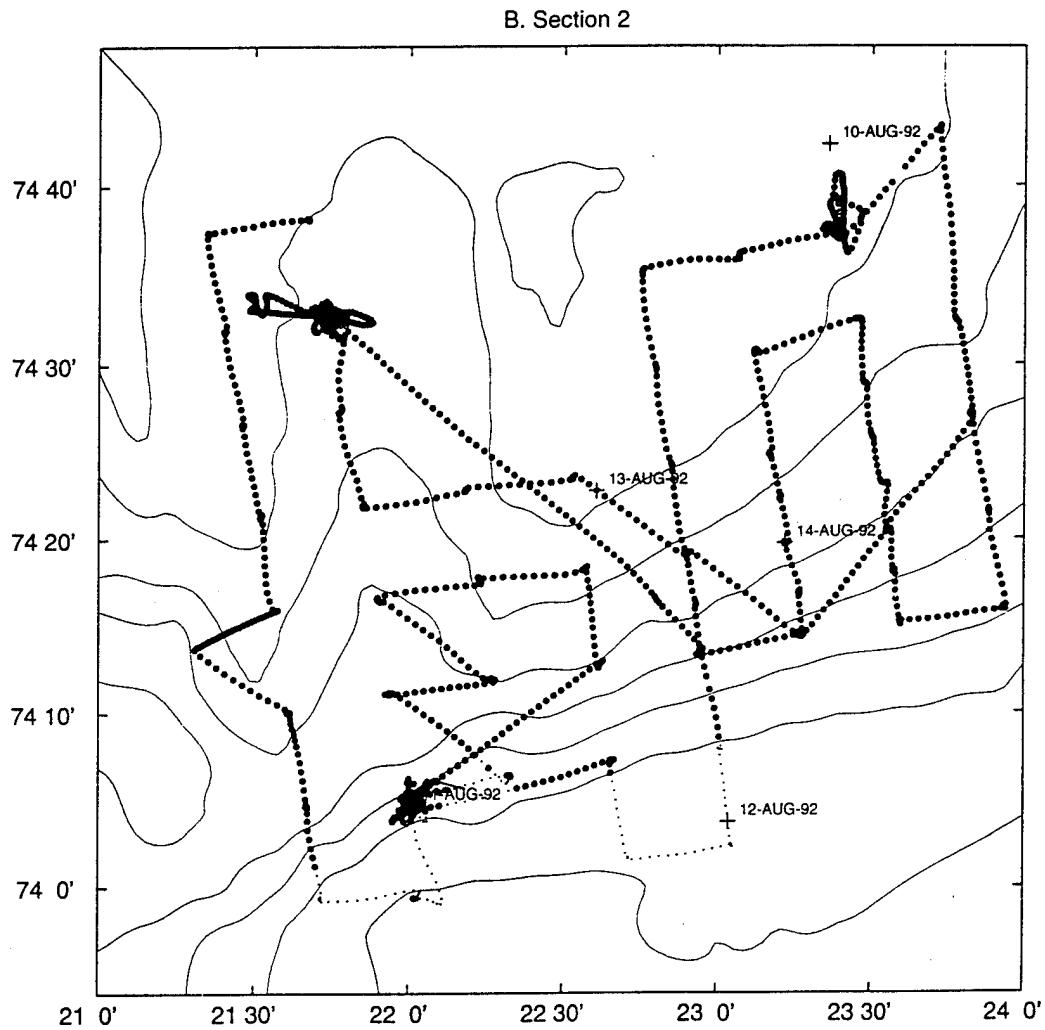


Figure 3b: Plan view of the ship's survey, section 2. Each ADCP station is shown by a small dot. A large dot represents an ADCP station with bottom tracking.

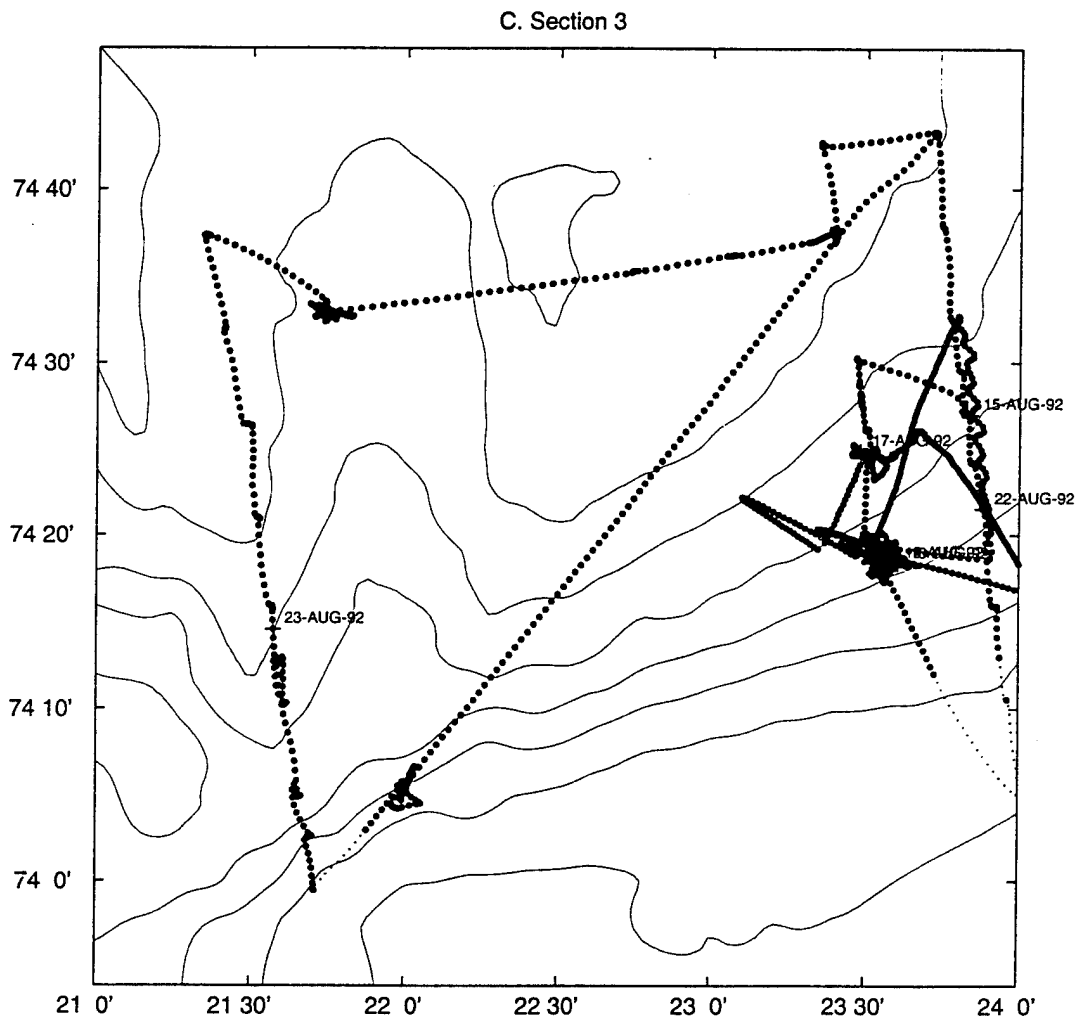


Figure 3c: Plan view of the ship's survey, section 3. Each ADCP station is shown by a small dot. A large dot represents an ADCP station with bottom tracking.

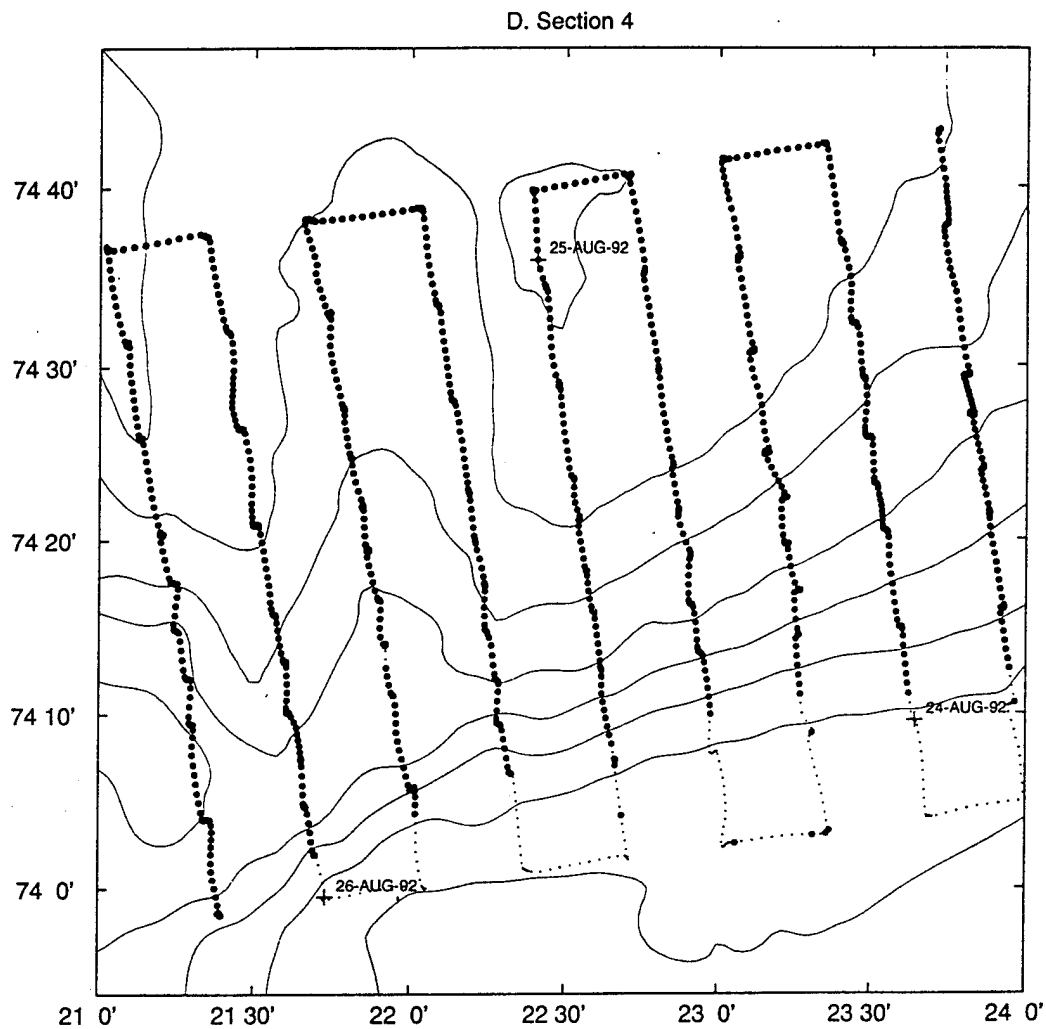


Figure 3d: Plan view of the ship's survey, section 4. Each ADCP station is shown by a small dot. A large dot represents an ADCP station with bottom tracking.

3 Determination of absolute velocity

3.1 Initial data processing

The raw ADCP data were decoded from the binary pingdata files and two preliminary filters were performed as recommended by RD Instruments (1989). The first filter removed (i.e. marked "bad") all velocities which were recorded with an accompanying percent good less than 30%. The second filter removed all velocity data in the last 15% of the water column, where the depth of the water column was determined by the ADCP bottom tracking.

There were two problems in the data associated with timing. The first occurred when the date on the clock of the personal computer recording the ADCP data was not advanced between 8-11-92 and 8-12-92 even though the time fields (hour, minute, second) advanced as usual. This problem was found onboard and corrected on 8-13-92. The second problem was discovered during the data analysis. A section of data approximately two hours long beginning on 8-20-92 02:21:04 was inexplicably saved out of sequence in the pingdata files beginning after ensemble 7729, 08-22-92 04:53:26. The problem was resolved by inserting the section into the proper sequence.

3.2 Absolute velocity

The bottom track velocities were used to remove the ship's velocity from the water track data to get absolute velocities:

$$u_{abs} = u_{wt} - u_{bt}$$

$$v_{abs} = v_{wt} - v_{bt}$$

where (u_{abs}, v_{abs}) are the absolute water velocities, (u_{wt}, v_{wt}) are the water track velocities given by the ADCP, and (u_{bt}, v_{bt}) are the bottom track velocities. As shown above (Figure 3), the bottom tracking did not give an entirely continuous record. Therefore, for all subsequent analysis, the ADCP velocity data were used only in regions where bottom tracking existed.

After removing the ship's velocity using the bottom track velocity, a filter was applied. The velocity data were first differenced in time at each depth bin and the standard deviation of these differenced values provided the basis for a two-step filter. First, at each depth, all data more than two standard deviations from the mean for that depth were removed. Second, all profiles which had at least 23 bad bins after performing step one of this filter were removed entirely. The cutoff number 23 was chosen from examining a histogram of the number of bad bins the initial

data processing marked in each ADCP profile. The histogram results showed that no profile had between 23 and 27 bad bins after the initial data processing. We elected to ignore profiles with 3 or fewer good depth bins and therefore accepted the “natural” cutoff present in the data of 23 bad depth bins.

This two-step filter removed both individual depth bins and entire profiles. The filter was applied twice resulting in the removal of 311 out of 10195 entire profiles, or 3% of the total, as well as additional individual depth bins.

To obtain accurate absolute water velocities, the ADCP velocities must be corrected for misalignment of the doppler transducer with the ship’s hull, actual sound-speed, and gyro bias. These corrections can be collapsed into a single transformation (Joyce, 1989; Pollard and Read, 1989):

$$\hat{u} = A(u \cos\phi + v \sin\phi) \quad (1a)$$

$$\hat{v} = A(v \cos\phi - u \sin\phi) \quad (1b)$$

where \hat{u}, \hat{v} are the corrected values of u, v , ϕ is the unknown rotation angle and A is the unknown scaling amplitude.

The GPS navigation data and ADCP bottom tracking give two different measurements of the ship’s velocity, although only the bottom track values need to be transformed as above. The error between the GPS and bottom tracking can be minimized by the method of least squares to find A and ϕ :

$$\epsilon_u = u_{GPS} + \hat{u}_{bt} \quad (2)$$

$$\epsilon_v = v_{GPS} + \hat{v}_{bt} \quad (3)$$

where (u_{bt}, v_{bt}) are the ADCP bottom track velocities, the hat (^) indicates the operation in Equation 1, (u_{GPS}, v_{GPS}) are the velocities calculated from GPS positions, and ϵ_u and ϵ_v are the quantities to be minimized. To avoid noisy data when the ship was on station, only data collected while the ship was moving faster than a cutoff velocity were used in determining A and ϕ . For this analysis, data was kept when the ship was steaming at 8-12 knots.

The angle ϕ was calculated as a sinusoidal function of the DAS ensemble average heading, ψ . To gain confidence in determining the function $\phi(\psi)$, the average heading was divided into 36 10° heading bins. Each heading bin was required to have a minimum of 15 DAS ensembles in order to be included in the least squares fit of a sine wave to ϕ . The amplitude A was also calculated as a function of heading but no trend was observed thus a constant value was used. A and ϕ were determined to be:

$$A = 0.9926$$

$$\phi = -2.7 + 4.1 \sin(\psi - 18^\circ)$$

with standard deviations of .01 and 1° respectively.

Once A and ϕ were found, the following transformation was performed, using Equation 1, to get the calibrated absolute water velocities:

$$\hat{u}_{abs} = A(u_{abs} \cos\phi + v_{abs} \sin\phi)$$

$$\hat{v}_{abs} = A(v_{abs} \cos\phi - u_{abs} \sin\phi)$$

One final filter was applied on the calibrated velocity data to produce the absolute water track velocities used in all further analyses. The first difference of the depth-mean velocity was calculated and all profiles with a first difference more than 5 standard deviations beyond the mean were removed. The absolute velocities from Grid 4 are shown in Figures 4a-4b. Plan views from 22 m, 54 m, and 78 m depth are shown in Figures 5a-5c.

3.3 Absolute velocity error estimates

According to RD Instruments (1989), the random error in the horizontal velocity components is approximately:

$$\sigma = (1.6 \times 10^5)/(FDN^{1/2})$$

where σ is the standard deviation (m/s), F is the frequency (Hz), D is the depth cell size (m) (assumed equal to the transmit pulse length), and N is the number of pings averaged together to get the velocity estimate.

Analysis of the data showed that on average, $N = 60$ pings per DAS ensemble. For $F = 300 \text{ kHz}$ and $D = 8 \text{ m}$, we find a random error of $\sigma = .9 \text{ cm/s}$.

The uncertainties in A and ϕ result in an additional bias in the data. Using the standard deviation of the two quantities this bias is found to be less than 1 cm/s.

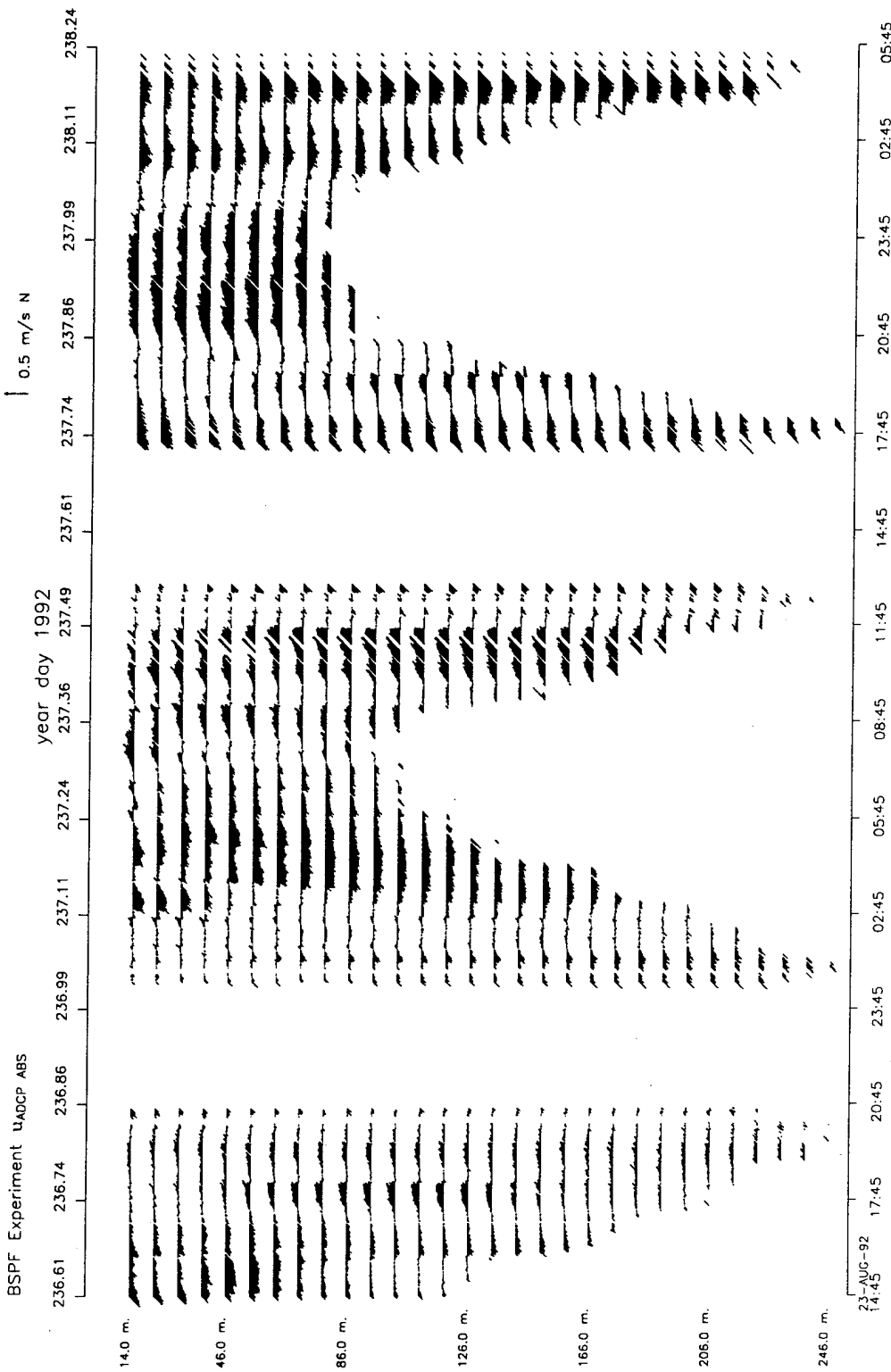


Figure 4a: Grid 4 absolute water velocities. The horizontal axis is time and the vertical axis is depth. Bins where velocities have been removed by a filter or due to the lack of a bottom track reference are shown as white space. The spacing between depth bins represents 50 cm/s. The velocity sticks are drawn from the baseline toward the direction the water is flowing, where north is toward the top axis.

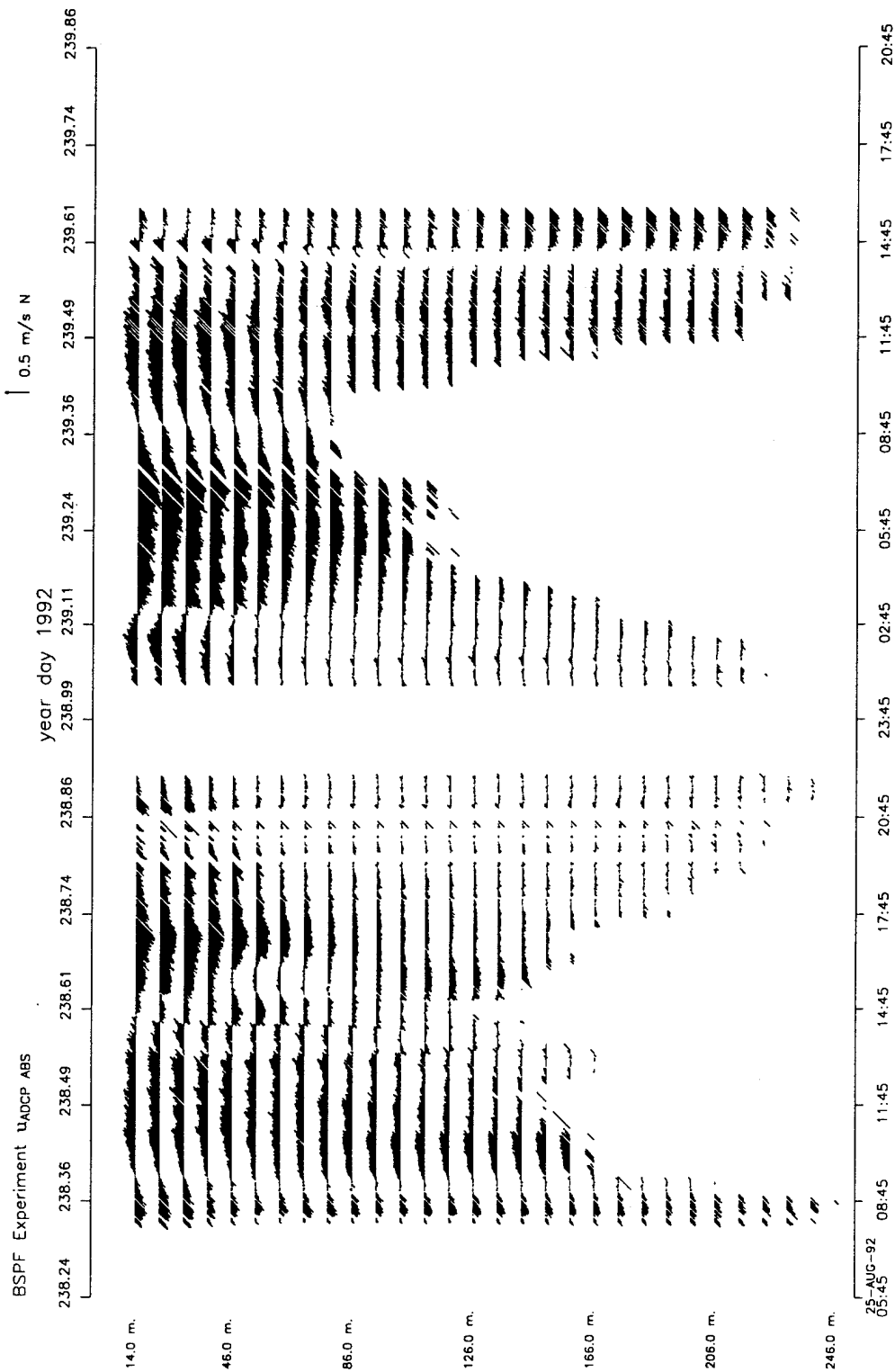


Figure 4b: Grid 4 (continued)

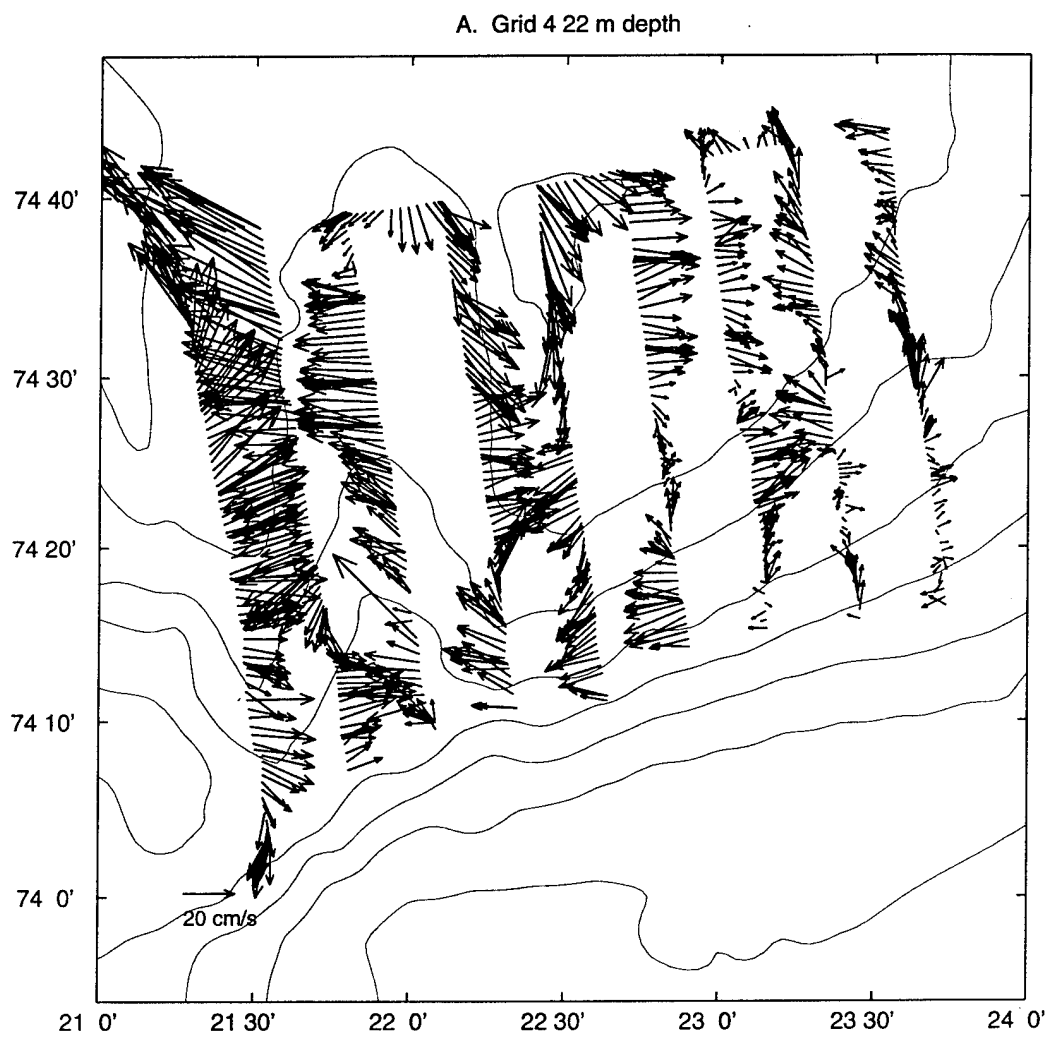


Figure 5a: Plan views of ADCP absolute velocity from 22 m depth.

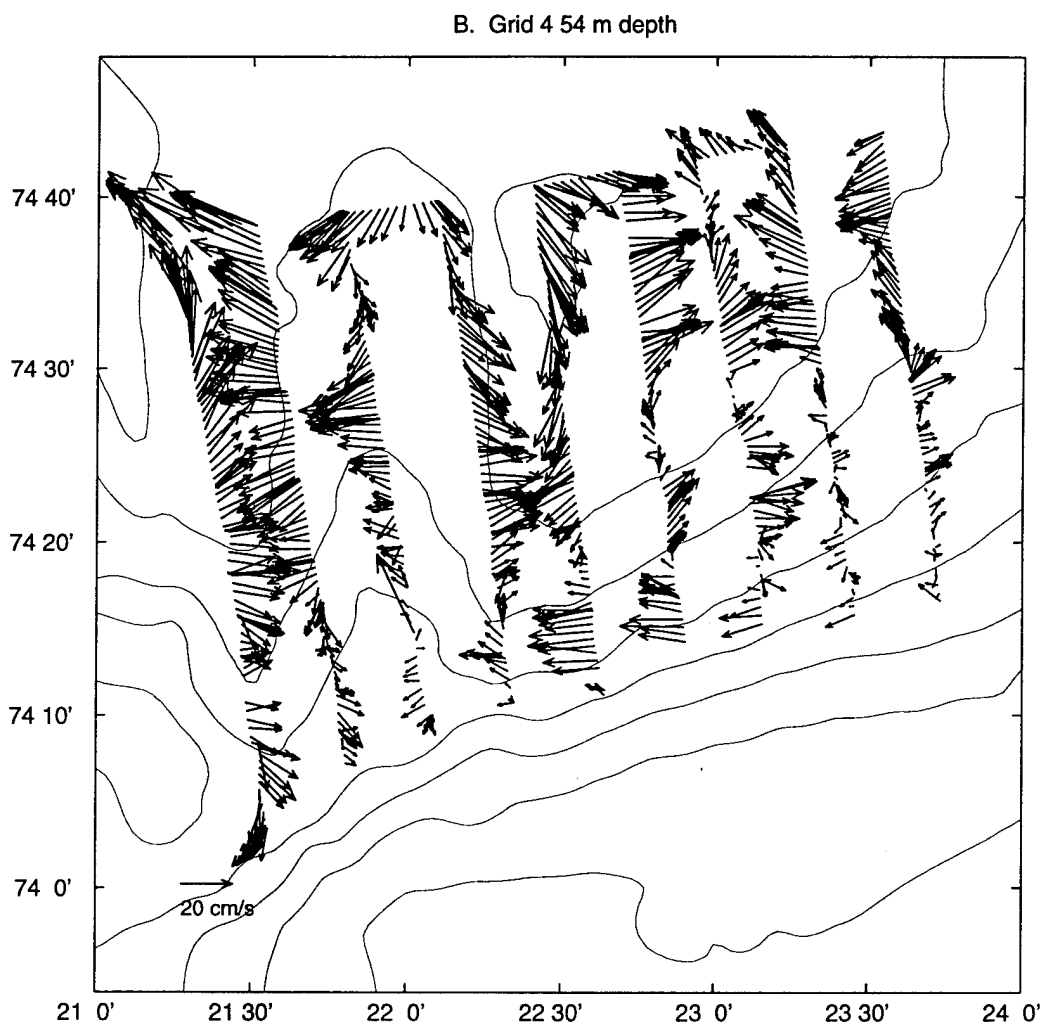


Figure 5b: Plan views of ADCP absolute velocity from 54 m depth.

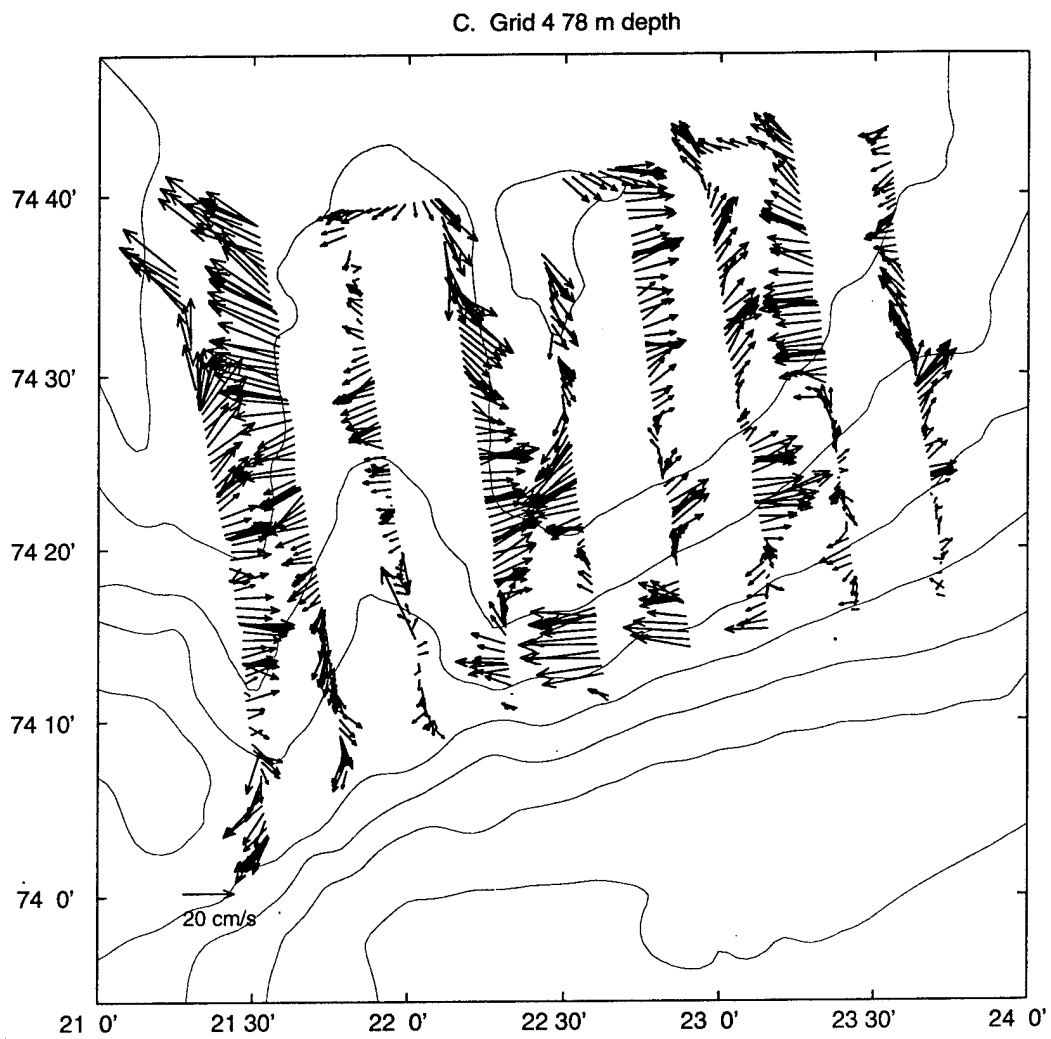


Figure 5c: Plan views of ADCP absolute velocity from 78 m depth.

4 Determination of sub-tidal flow

4.1 Current meter data

The current meter records at all locations were dominated by tidal oscillations (Figure 15). A tidal analysis (Parsons *et al.*, submitted) showed the M_2 tide to be dominant with amplitudes of 12–17 cm/s on the shelf (NE and NW) and 10 cm/s in deeper water (SW). S_2 and K_1 constituents were also significant. The space-time grid of ADCP velocities also shows a strong tidal influence (Figures 5a–5c, and 15). The strong tidal oscillations dictated the use of a tide removal scheme to extract a steady flow component. This was done using the tide removal technique described by Candela *et al.*, (1992). The technique, based on a least-squares fit, assumes the space-time grid of data can be modelled as a sum of harmonic functions at specified frequencies (the tidal constituents) and a temporally steady flow. Both the tidal currents and the steady flow may vary spatially. All available velocity data can be combined and used in this model to get the best possible time and space resolution.

As discussed by Candela *et al.* (1992), it is necessary to choose an order for the model polynomial to be fit to the data. A first degree polynomial (a plane in space) gave the best possible fit to the current meter data because there were only three mooring locations. Although ultimately the current meter and ADCP data were used together in the model, the current meter data were first detided separately and used to determine the optimal model order for the ADCP data.

Figures 6–11 show the results from detiding the hourly current meter data at 20 m and 50 m depth. Although current meters existed at 80 m depth on the NE and SW moorings, the 80 m depth data were not used alone in the model because data at three locations are required for the first order fit. Figures 12–14 show the results from detiding the depth-averaged current meter data. This average contains information from 20 m, 50 m, and 80 m depth at the SW and NE moorings. At the NW mooring the average is over the 20 m and 50 m current meters. Note that from this analysis alone the tidal phases have a 180° ambiguity relative to Greenwich. However, comparison with the model results of Kowalik and Proshutinsky (1994) indicates that the phases are correct as presented.

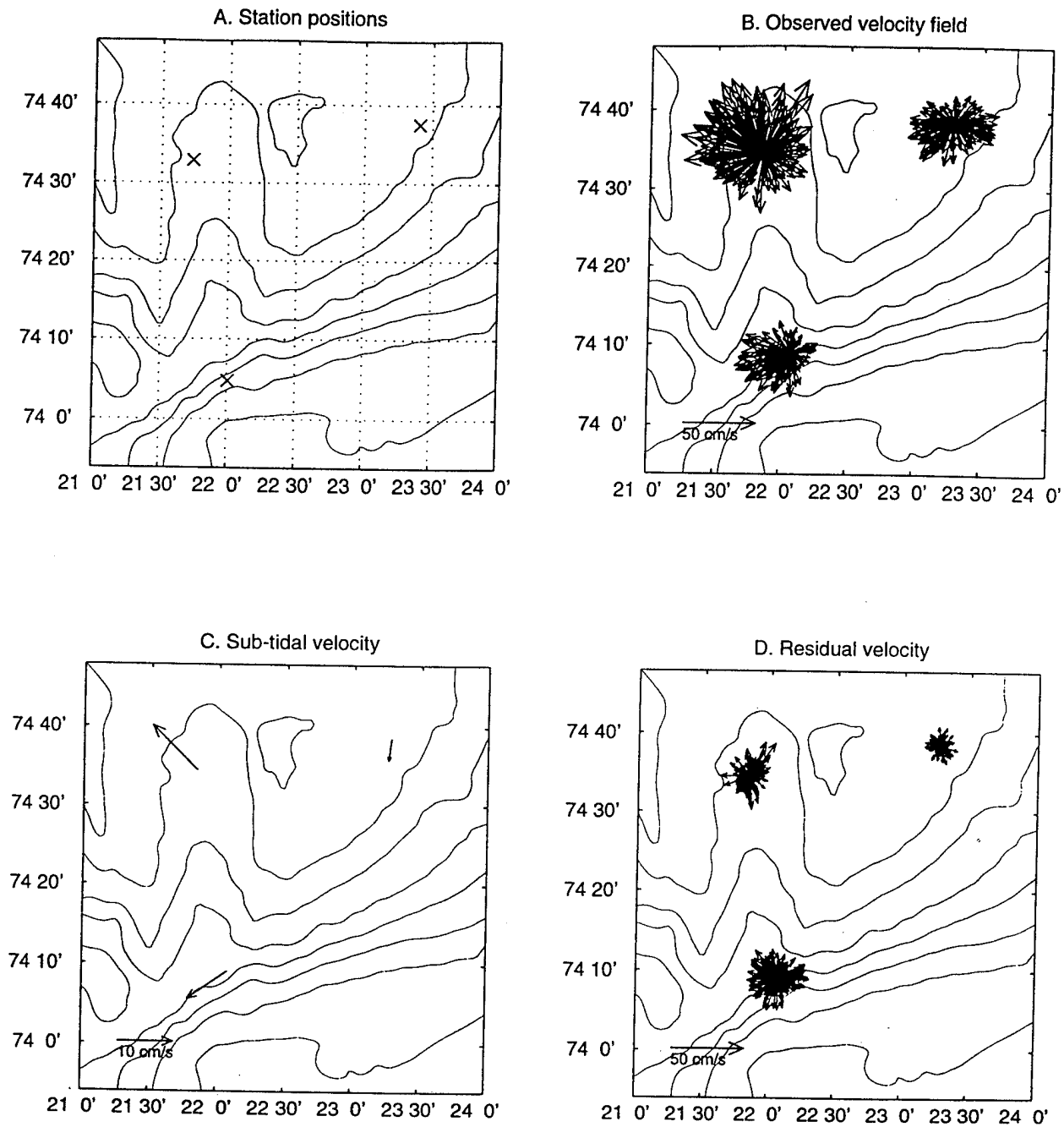


Figure 6: Plan views of current meter velocities from 20 m depth. Shown are (A) input data positions, (B) input current vectors, (C) sub-tidal steady velocity, and (D) model residual velocity.

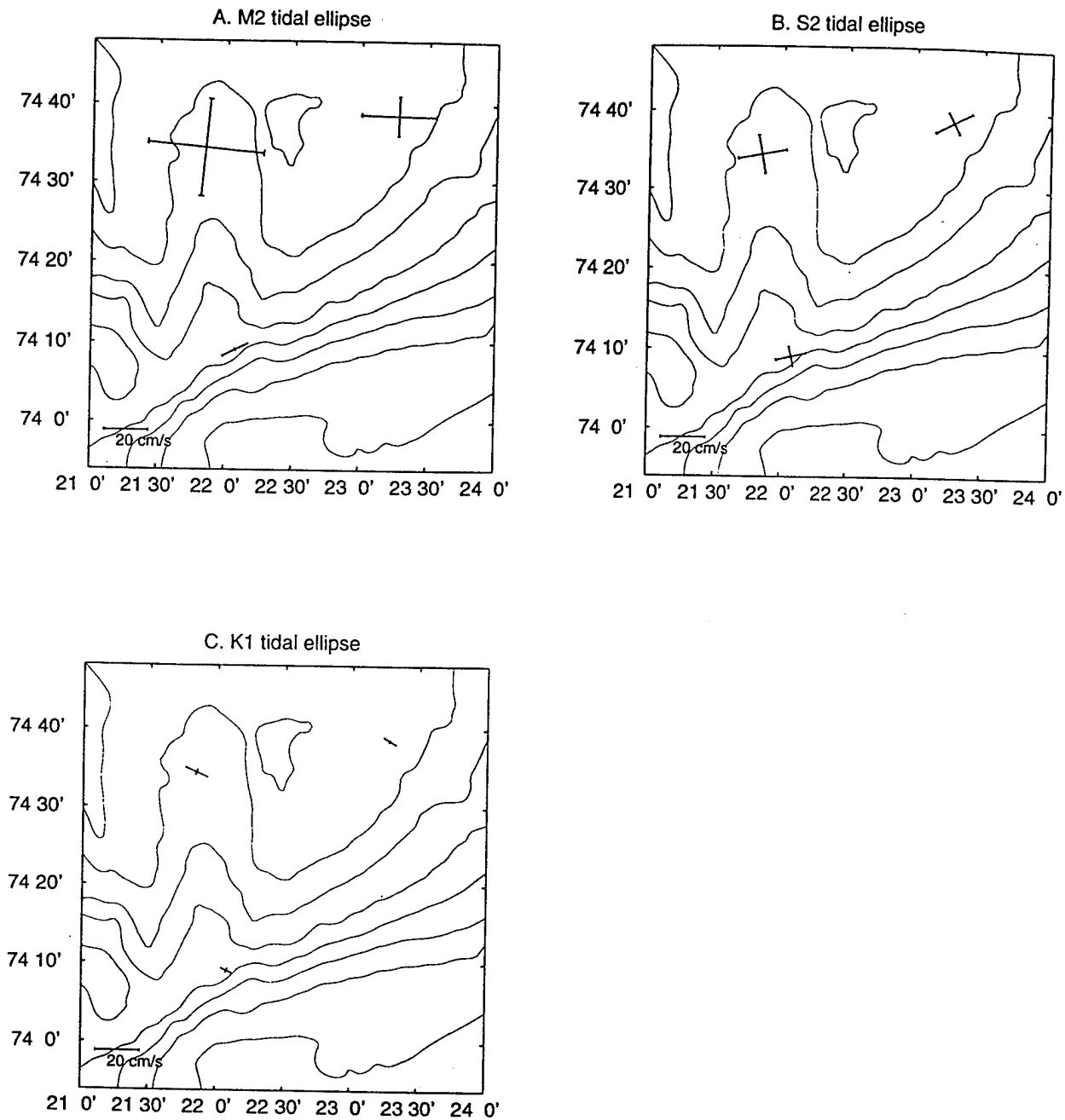


Figure 7: Plan views of model tidal ellipses from current meter data at 20 m depth. Shown are (A) M_2 tidal ellipses, (B) S_2 tidal ellipses, and (C) K_1 tidal ellipses.

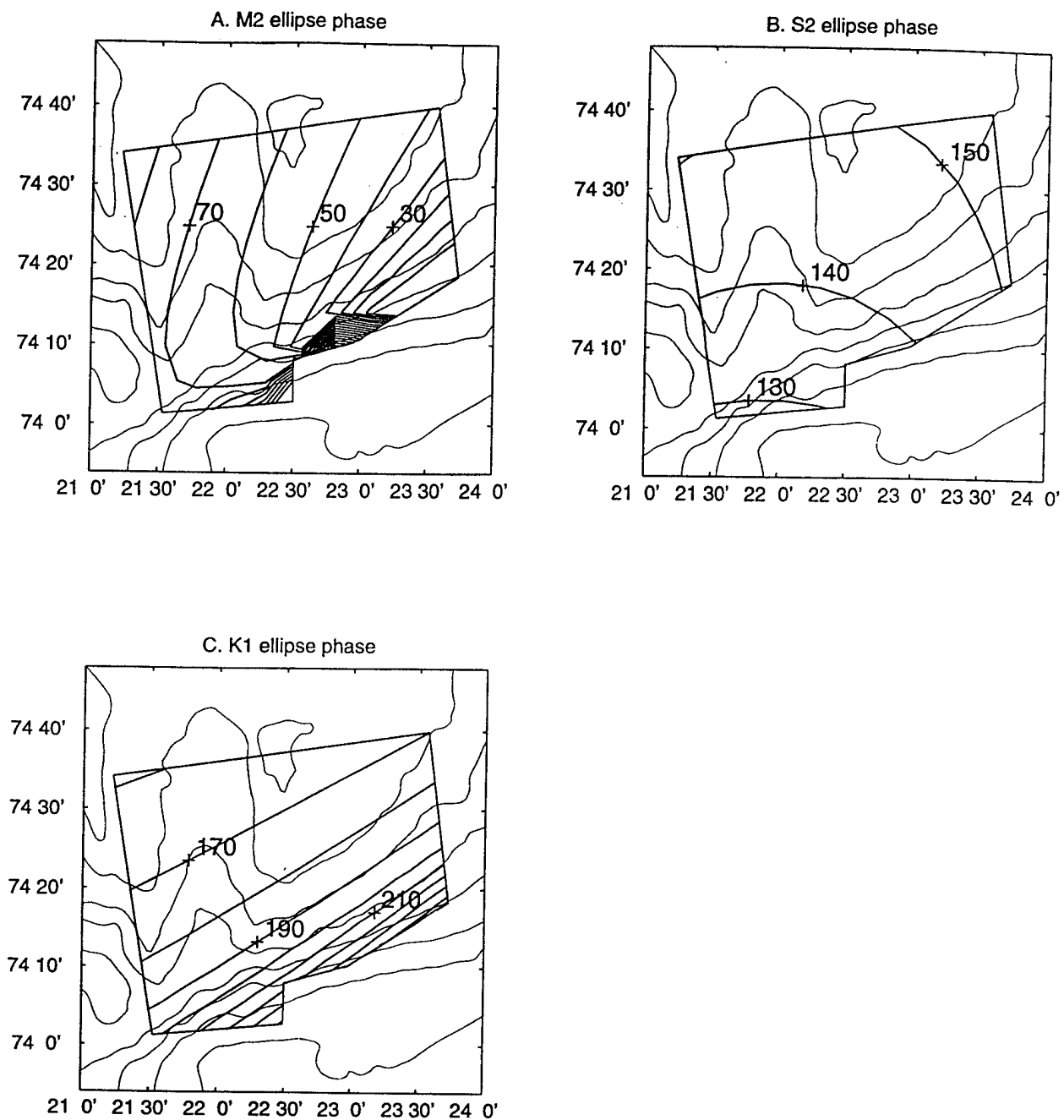


Figure 8: Plan views of model tidal phases from current meter data at 20 m depth. Shown are (A) M_2 tidal phase, (B) S_2 tidal phase, and (C) K_1 tidal phase.

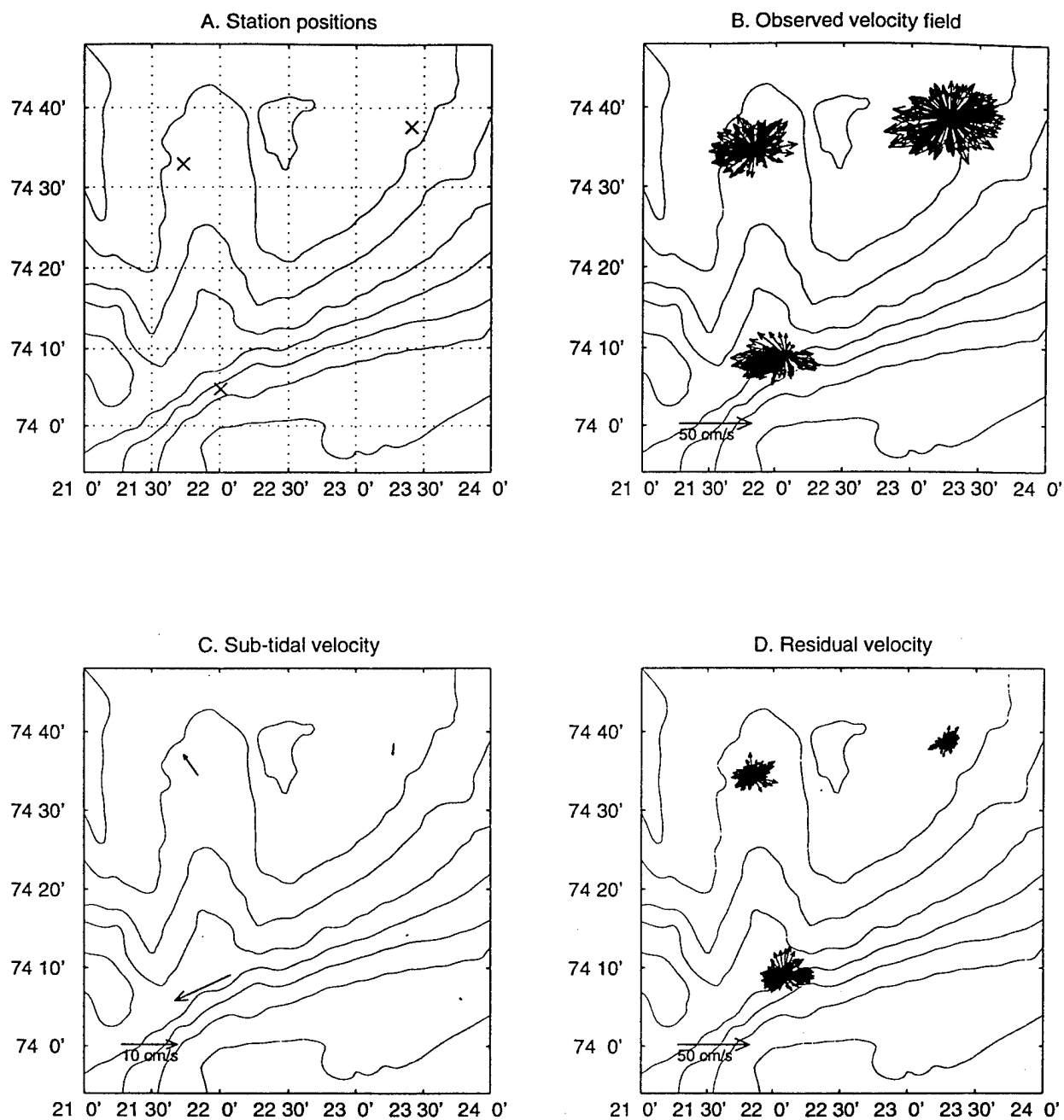


Figure 9: Plan views of current meter velocities from 50 m depth. Shown are (A) input data positions, (B) input current vectors, (C) sub-tidal steady velocity, and (D) model residual velocity.

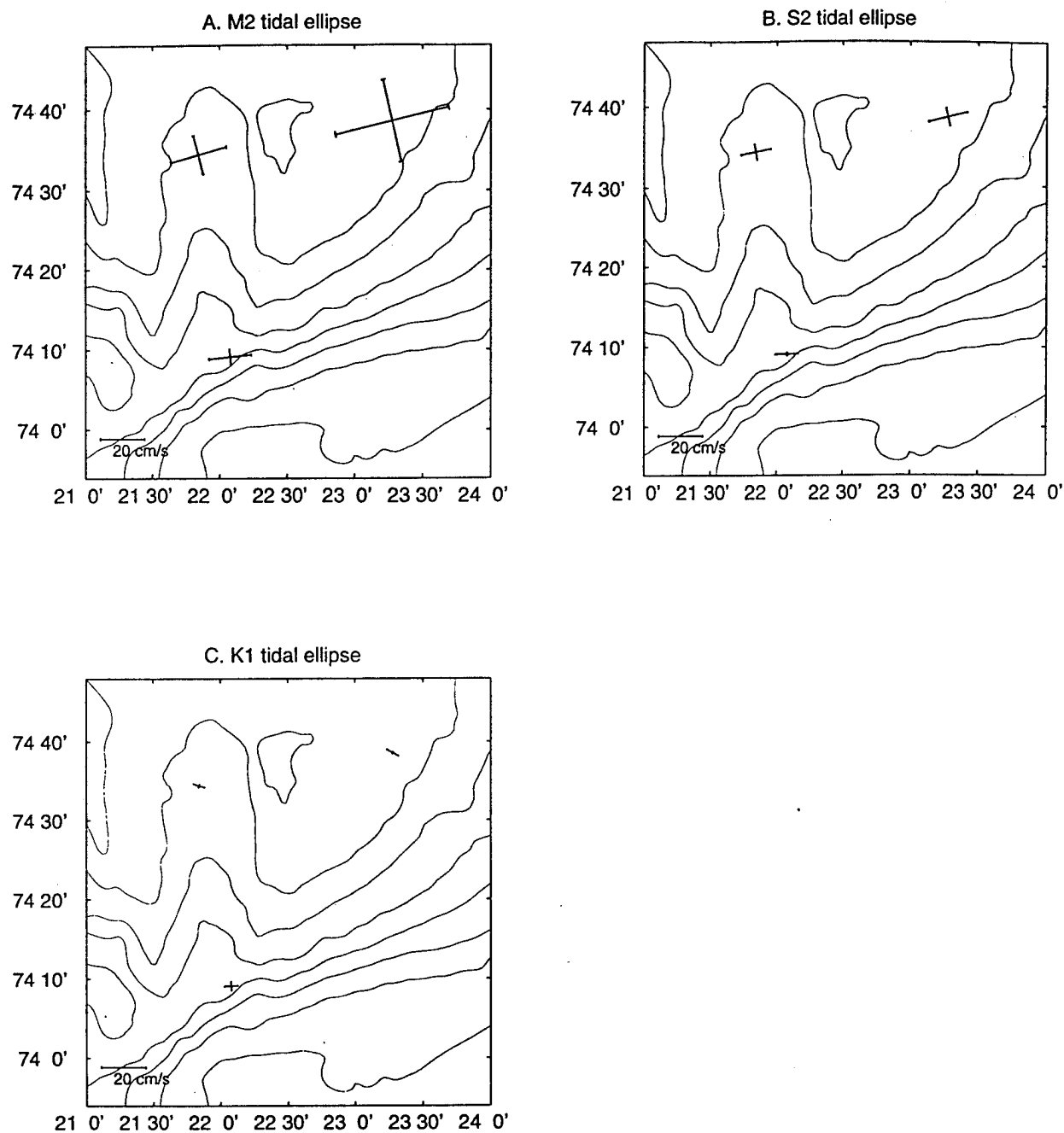


Figure 10: Plan views of model tidal ellipses from current meter data at 50 m depth. Shown are (A) M₂ tidal ellipses, (B) S₂ tidal ellipses, and (C) K₁ tidal ellipses.

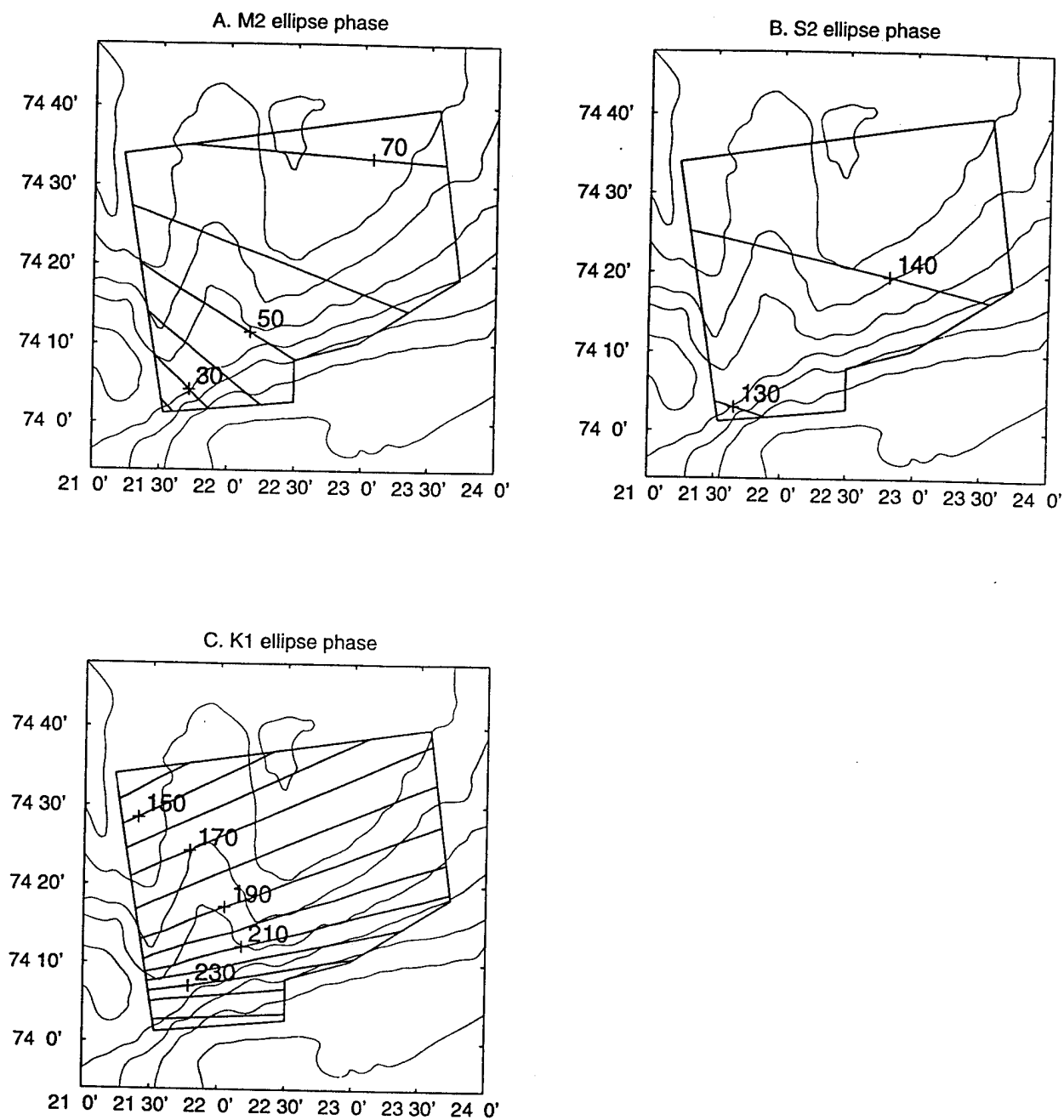


Figure 11: Plan views of model tidal phases from current meter data at 50 m depth. Shown are (A) M_2 tidal phase, (B) S_2 tidal phase, and (C) K_1 tidal phase.

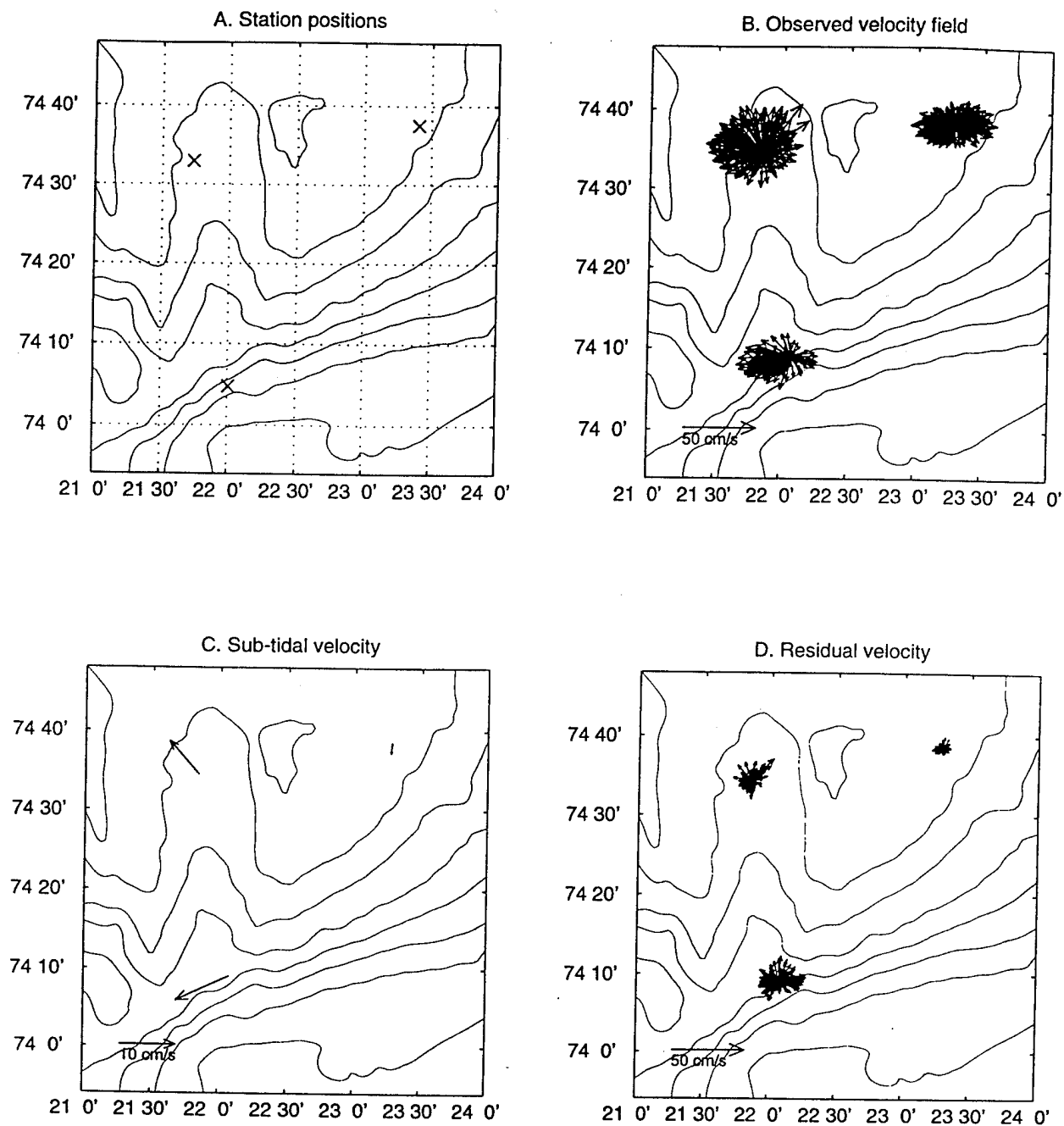


Figure 12: Plan views of depth averaged current meter velocities. Shown are (A) input data positions, (B) input current vectors, (C) sub-tidal steady velocity, and (D) model residual velocity.

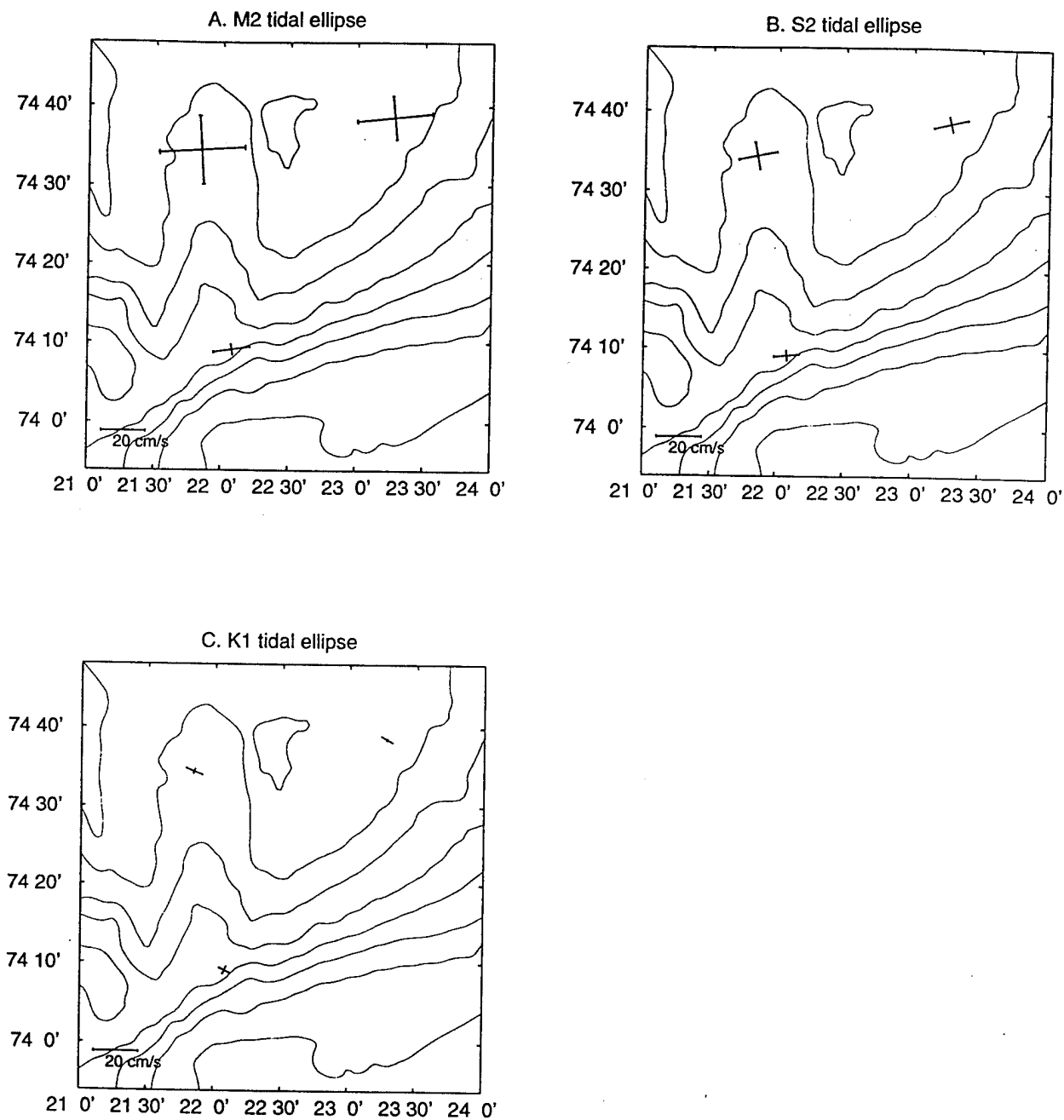


Figure 13: Plan views of model tidal ellipses from depth averaged current meter data. Shown are (A) M_2 tidal ellipses, (B) S_2 tidal ellipses, and (C) K_1 tidal ellipses.

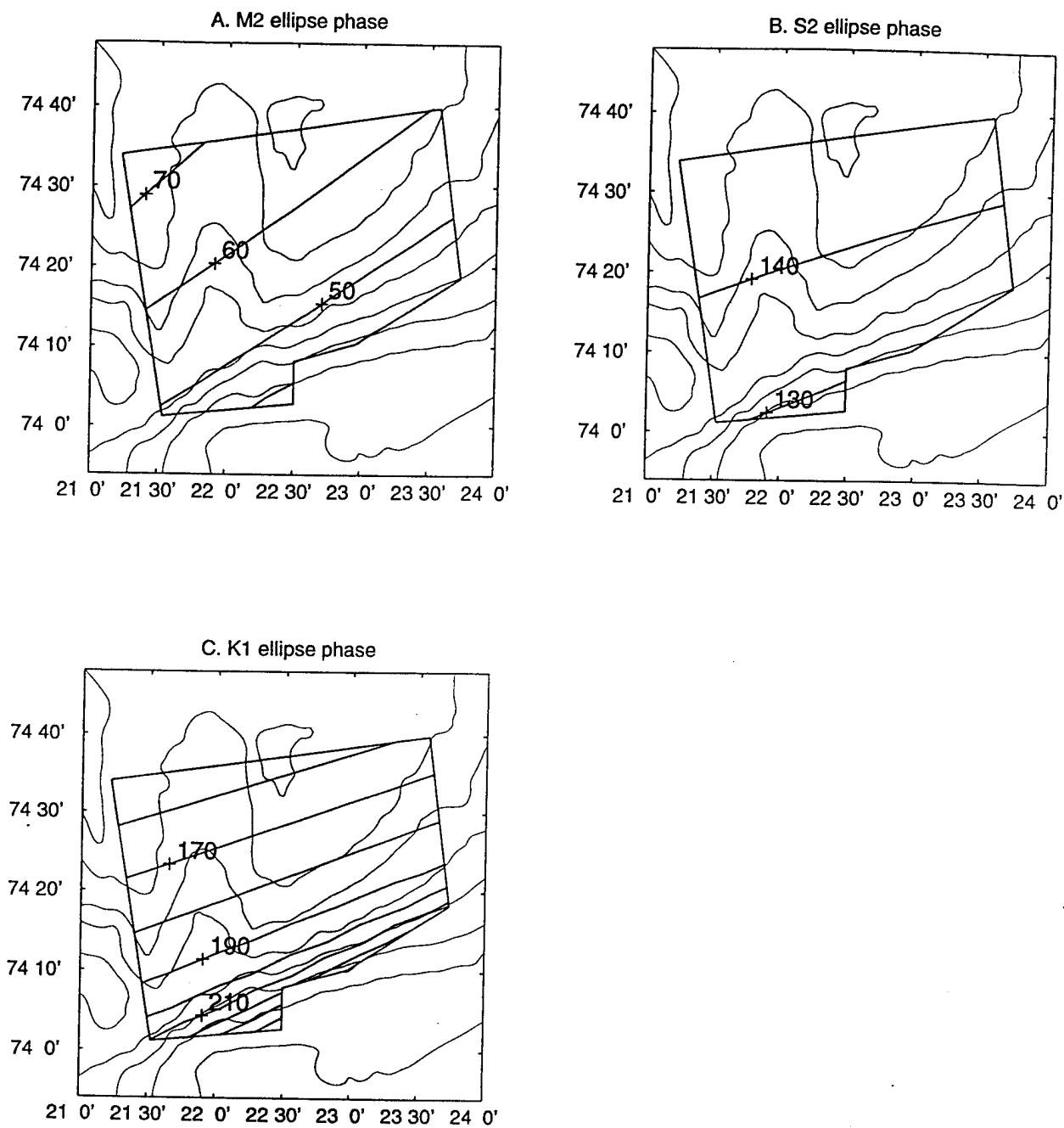


Figure 14: Plan views of model tidal phases from depth averaged current meter data. Shown are (A) M_2 tidal phase, (B) S_2 tidal phase, and (C) K_1 tidal phase.

4.2 ADCP data

In this section we determine the model order for the ADCP data and present the results from detiding the ADCP data.

The information in the ADCP and the current meter data sets can be combined to get the best possible representation of the tidal and sub-tidal fields. Conceptually, the ADCP data is used to fill in the gaps between the current meter data which is well resolved in time, but poorly resolved in space. Reasonable agreement between the ADCP and current meter component velocities shows that combining the data is sensible (Figure 15).

The optimal model order for the space-time grid of ADCP data, or for the combined ADCP/current meter data set, is more difficult to determine than for the current meter data alone. The ADCP data give greater spatial coverage, presumably allowing one to resolve a higher order polynomial in the data. As noted by Candela *et al.* (1992), higher order polynomials will generally reduce the model residual. However, lower order polynomials are preferable because increasing the model order too far allows the model to fit the noise in the data, rather than the signal. When the proper model order has been chosen for the ADCP data, the detided results at the three mooring locations should agree with the results from the current meters because the current meter data contain the best coverage at these locations. Therefore, the detided current meter results were used as a benchmark in evaluating the success of detiding the ADCP data.

Prior to detiding, the ADCP profiles outside of the survey region (e.g. those from when the ship was steaming to the survey site) were removed from the dataset. This reduced the number of ADCP ensembles from 10195 to 9523. In addition, the ADCP data were averaged in time/space to give one velocity per depth bin for every 1 hour or 10 km alongtrack distance, whichever came first. This averaging made the ADCP data more comparable to the hourly current meter data.

To find the optimal model order, a misfit error was defined using the difference between the detided ADCP data and the detided current meter data. For the purpose of computing the misfit, the detided ADCP results, available over the entire survey region, were computed only at the current meter locations. For direct comparison with the 20 m, 50 m, and 80 m depth current meter data, only ADCP data centered at depth bins of 22 m, 54 m, and 78 m were used. For ease of notation we refer to these depths as 20 m, 50 m, and 80 m, respectively.

The sum of the squared error was used to compare results from model fits using different polynomial orders. For the sub-tidal steady components the detided results are in the form of northward and eastward velocities. The sub-tidal error at each

mooring i is defined as:

$$\epsilon_{u_i} = u_{CM_i} - u_{ADCP_i}$$

$$\epsilon_{v_i} = v_{CM_i} - v_{ADCP_i}$$

The total sub-tidal error is found by summing over the number of moorings p :

$$\text{Total sub-tidal error} = \sum_{i=1}^p \epsilon_{u_i}^2 + \epsilon_{v_i}^2$$

For each tidal component j , the detided results are in the form of the equation of an ellipse: $a_{j,1}x^2 + a_{j,2}y^2 + a_{j,3}xy + a_{j,4} = 0$ and the errors are defined using the ellipse equation coefficients:

$$\epsilon_{tide_j} = \sum_{k=1}^4 a_{CM_{j,k}} - a_{ADCP_{j,k}}$$

$$\text{Total tidal error} = \sum_{j=1}^t \epsilon_{tide_j}^2$$

where a_{CM} is a current meter data ellipse coefficient, a_{ADCP} is an ADCP data ellipse coefficient, and t is the number of tidal constituents in the model, in our case, three.

To reduce the number of trials necessary to determine the proper order, the three tidal constituents (M_2 , S_2 , K_1) were assigned the same order polynomial and only model polynomials of order 1–3 were examined. In all model runs, the total tidal error was minimized with a model order of one, indicating that the tides varied linearly across the survey region (Table 3). As discussed above (see page 35), the sub-tidal part of the solution generally showed a decreasing error with increasing model order rather than an absolute minimum. However, the maximum decrease in the total sub-tidal error took place between the model orders one and two so it was assumed that the maximum goodness-of-fit to the signal would be found for a model order of two. Thus the tidal order was chosen to be one and the sub-tidal order was chosen to be two.

The model runs of ADCP data comparable to the 20 m and 50 m depth current meter data are shown in Figures 16–21. Note that the results of the tidal model are shown for only a subset of the input data locations. Results at the western, northern, and eastern edge of the survey region are not presented because of the larger errors there. The errors are discussed in greater detail in section 4.4.

The ADCP data from 80 m was not used to determine the model polynomial order because of the lack of a comparison at 80 m in the current meter data (see section 4.1). However, for completeness of presentation, the results from the 80 m ADCP model and the ADCP three depth average model (20 m, 50 m, 80 m) are shown in Figures 22–27.

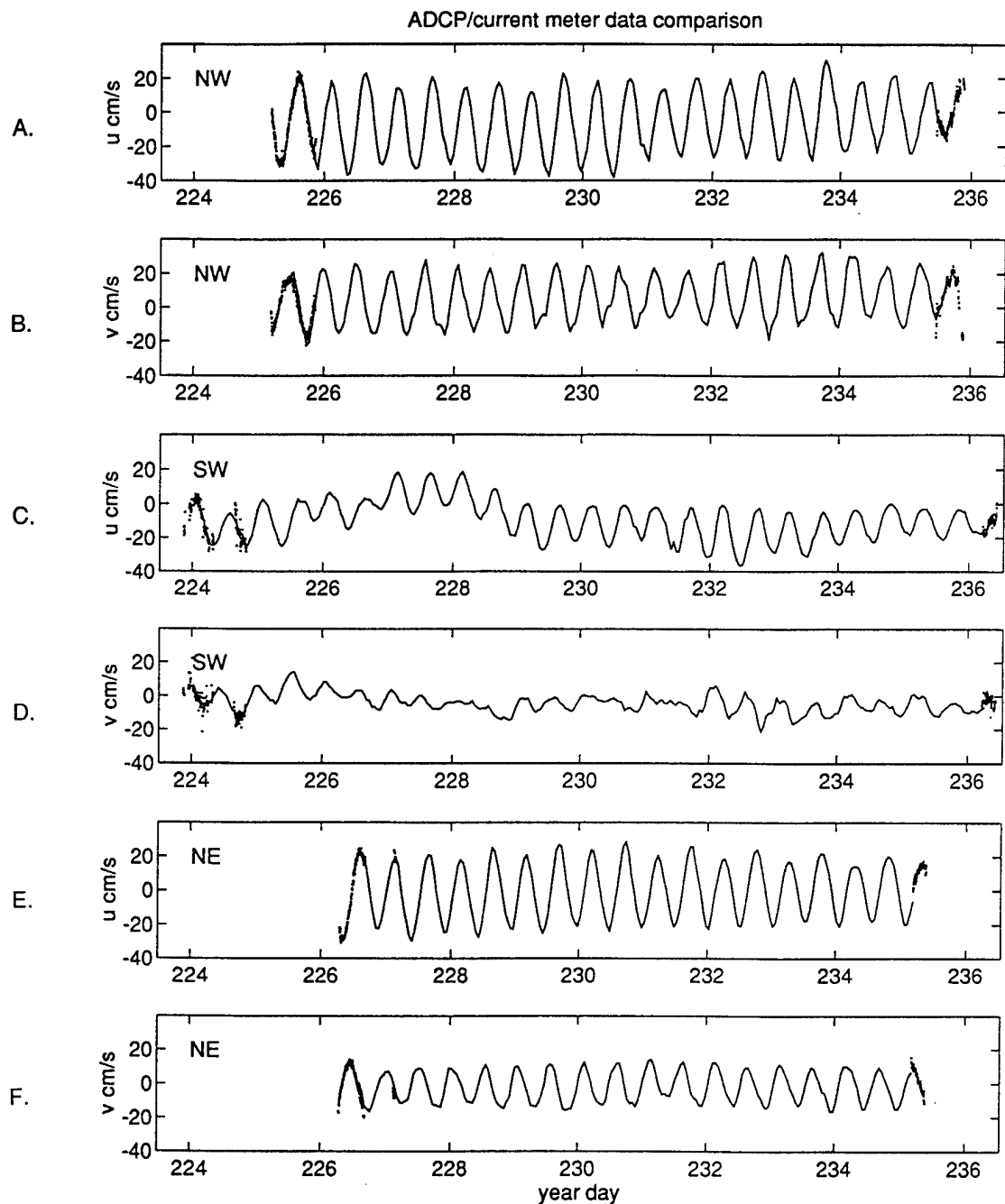


Figure 15: Time series of ADCP velocity within 10 km of the mooring locations. The thin line shows the depth-averaged eastward and northward current meter velocities at (A), (B) the NW mooring, (C), (D) the SW mooring, and (E), (F) the NE mooring. The thick dots show the ADCP velocity averaged over depth bins corresponding to the current meter depths. The current meters were at nominal depths of 20 m, 50 m, and 80 m and the ADCP depth bins were centered at 22 m, 54 m, and 78 m depth.

depth (m)	tidal polynomial degree	sub-tidal polynomial degree	tidal misfit	sub-tidal misfit	sub-tidal misfit change
20	1	1	0.097	70.8	
20	1	2	0.111	32.7	-38.1
20	1	3	0.109	36.4	3.7
20	2	1	0.143	83.0	
20	2	2	0.155	85.8	2.8
20	2	3	0.206	75.2	-10.6
20	3	1	0.227	76.1	
20	3	2	0.293	58.5	-17.6
20	3	3	0.351	52.7	- 5.8
50	1	1	0.010	95.5	
50	1	2	0.007	50.7	-44.8
50	1	3	0.008	41.2	- 9.5
50	2	1	0.048	87.5	
50	2	2	0.030	75.8	- 5.7
50	2	3	0.020	66.4	- 9.4
50	3	1	0.072	84.3	
50	3	2	0.070	71.2	-13.1
50	3	3	0.036	51.2	-20.0

Table 3: The model polynomial misfits are shown for two separate depths as a function of tidal polynomial degree and sub-tidal polynomial degree for model orders 1–3. The three tidal components M_2 , S_2 , and K_1 are always given the same polynomial degree. As defined, the units of the tidal misfit and sub-tidal misfit are not the same. The final column shows the change in sub-tidal misfit found by increasing the sub-tidal polynomial degree but keeping the tidal polynomial degree constant. The table shows a minimum in tidal misfit for a first degree tidal polynomial and a maximum decrease in sub-tidal misfit between sub-tidal polynomial degrees 1 and 2.

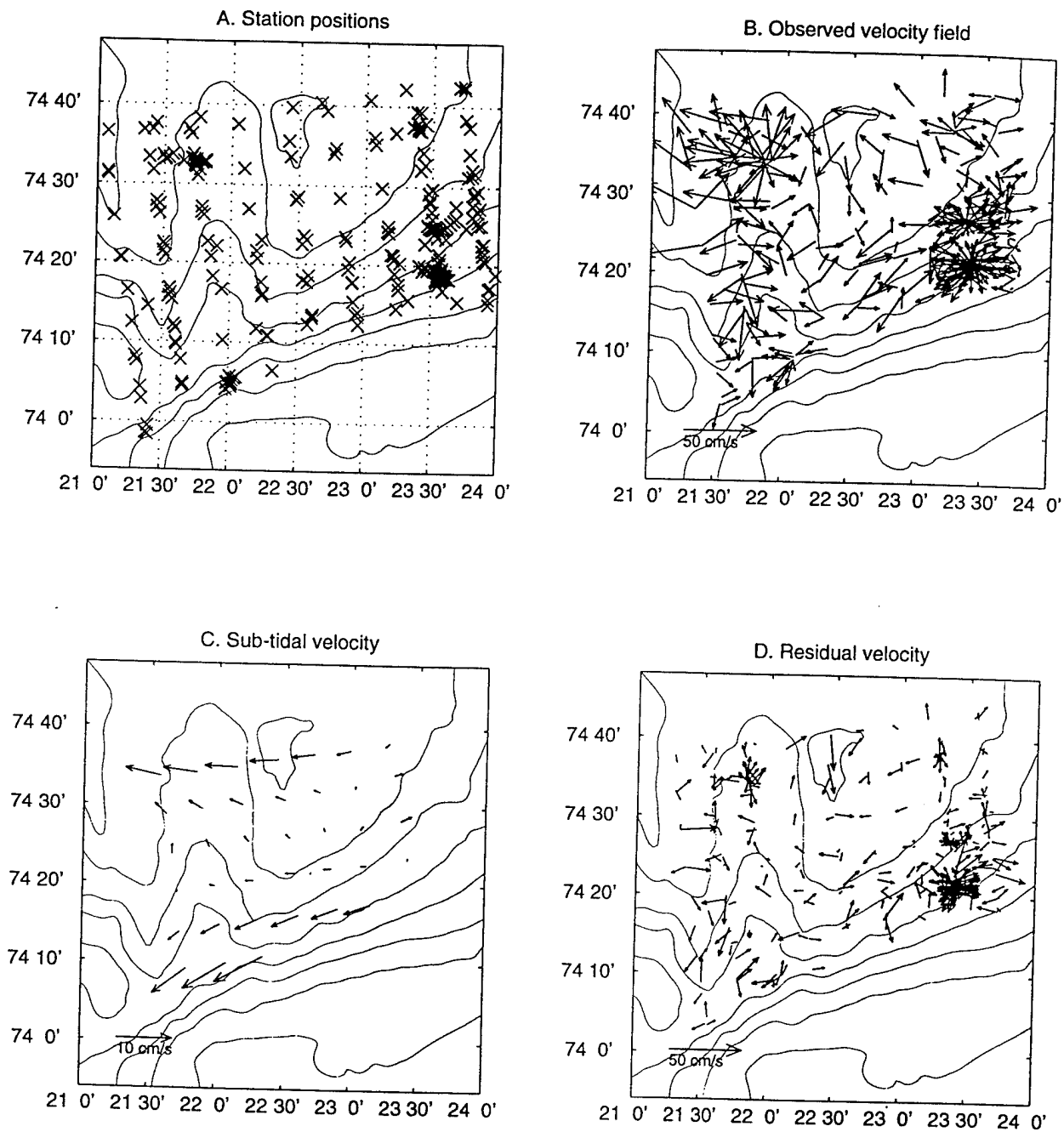


Figure 16: Plan views of ADCP velocities from 20 m depth. Shown are (A) input data positions, (B) input current vectors, (C) sub-tidal steady velocity, and (D) model residual velocity. Compare with Figure 6.

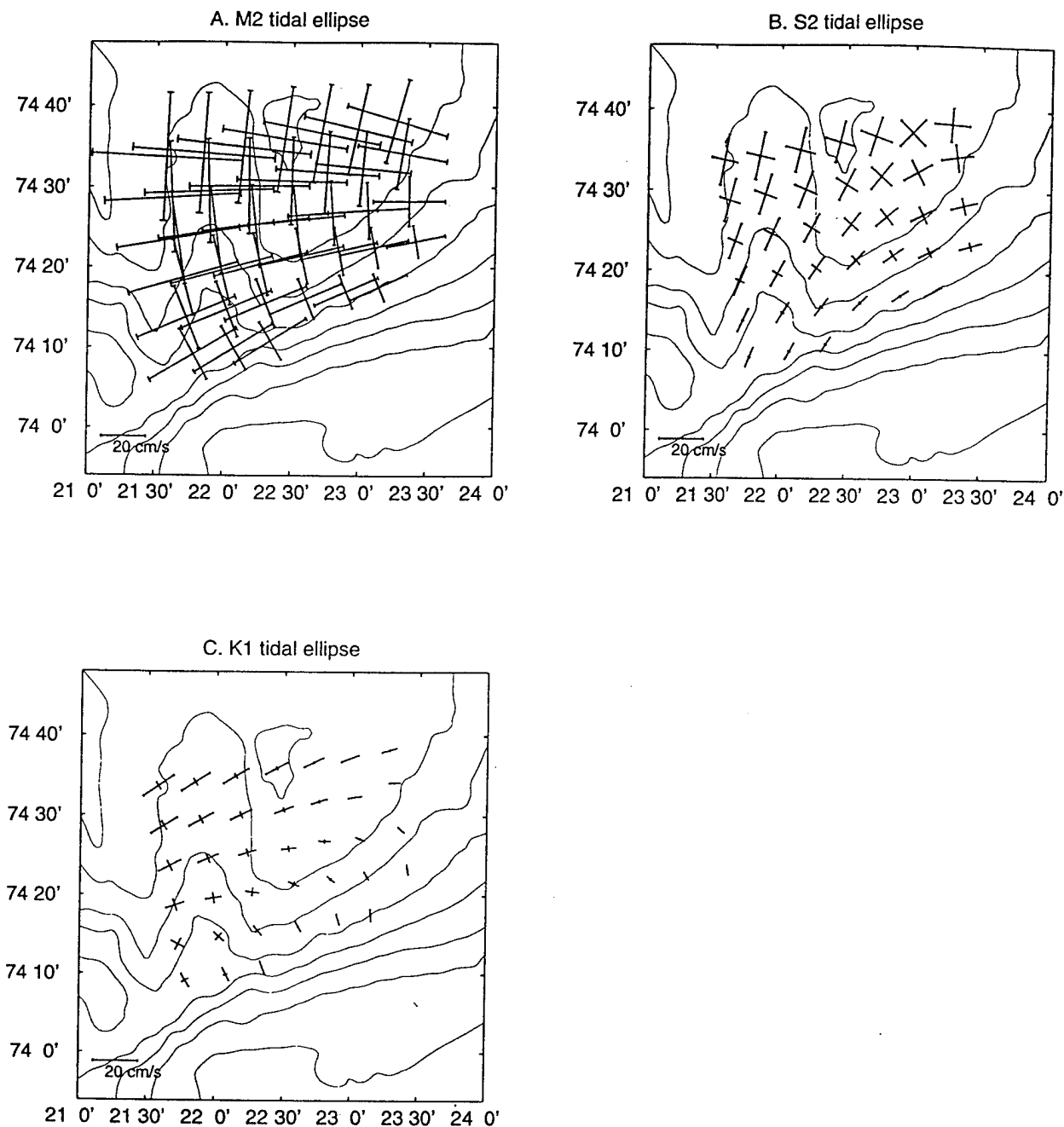


Figure 17: Plan views of model tidal ellipses from ADCP data at 20 m depth. Shown are (A) M_2 tidal ellipses, (B) S_2 tidal ellipses, and (C) K_1 tidal ellipses. Compare with Figure 7.

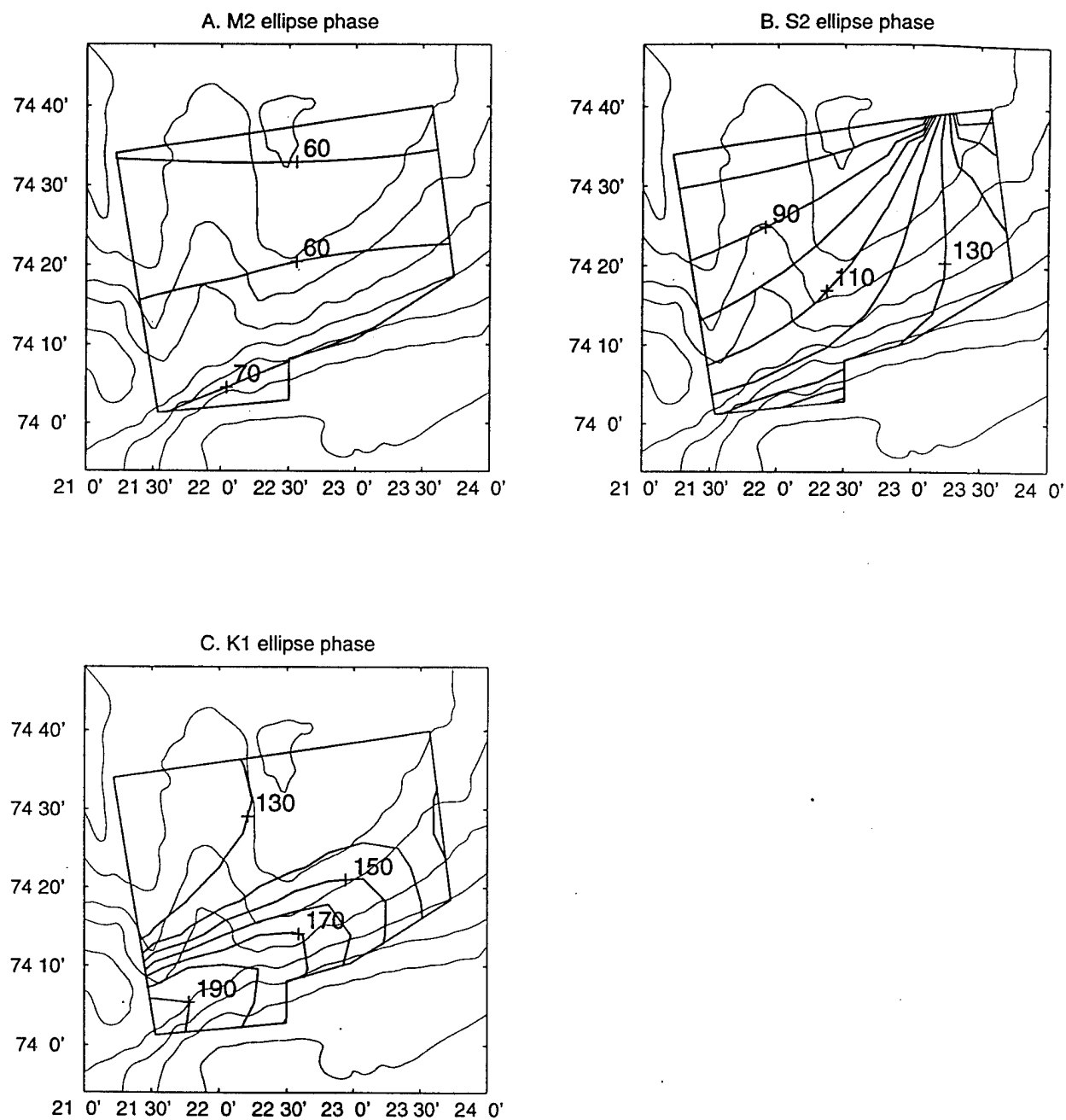


Figure 18: Plan views of model tidal phases from ADCP data at 20 m depth. Shown are (A) M_2 tidal phase, (B) S_2 tidal phase, and (C) K_1 tidal phase. Compare with Figure 8.

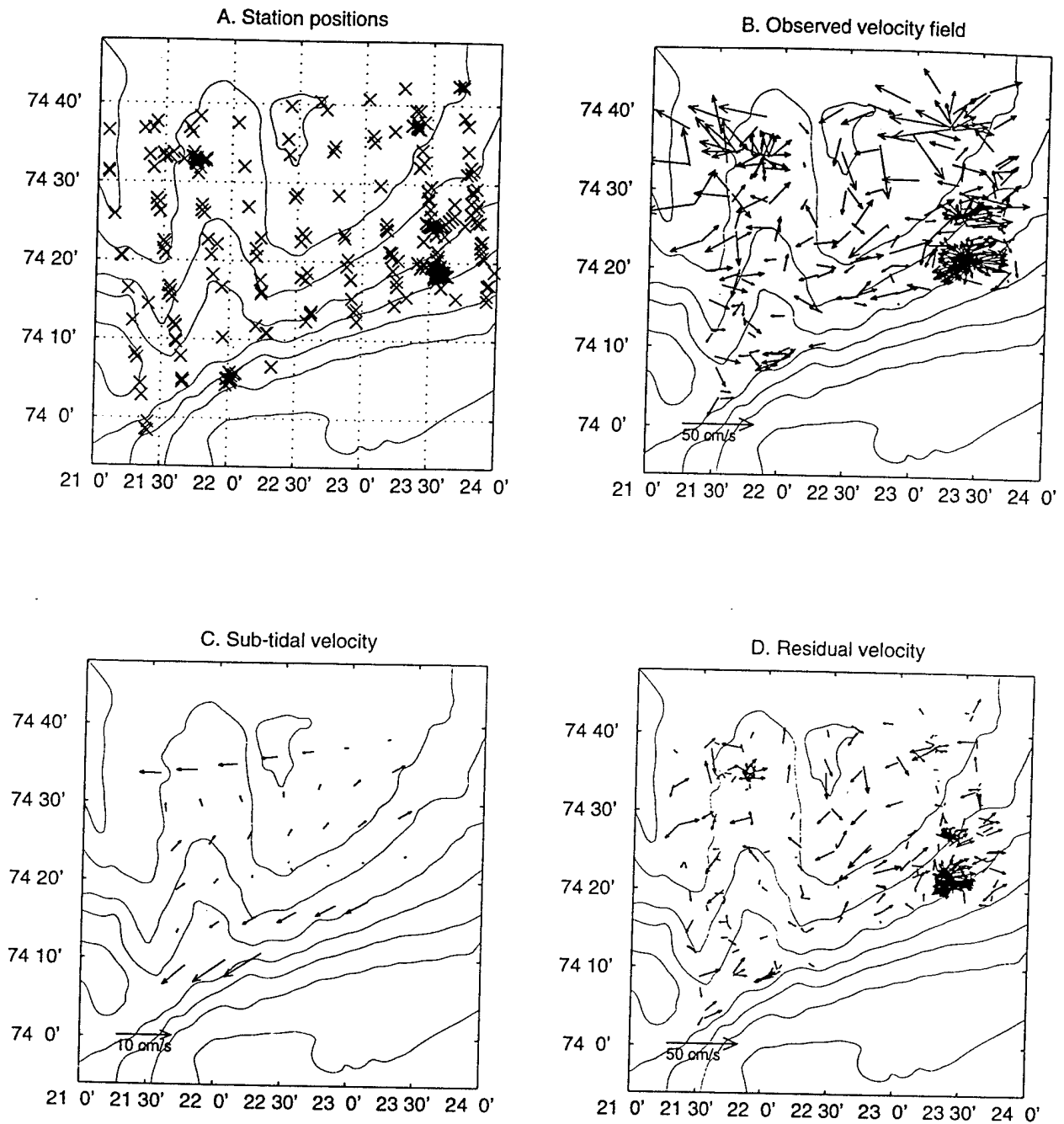


Figure 19: Plan views of ADCP velocities from 50 m depth. Shown are (A) input data positions, (B) input current vectors, (C) sub-tidal steady velocity, and (D) model residual velocity. Compare with Figure 9.

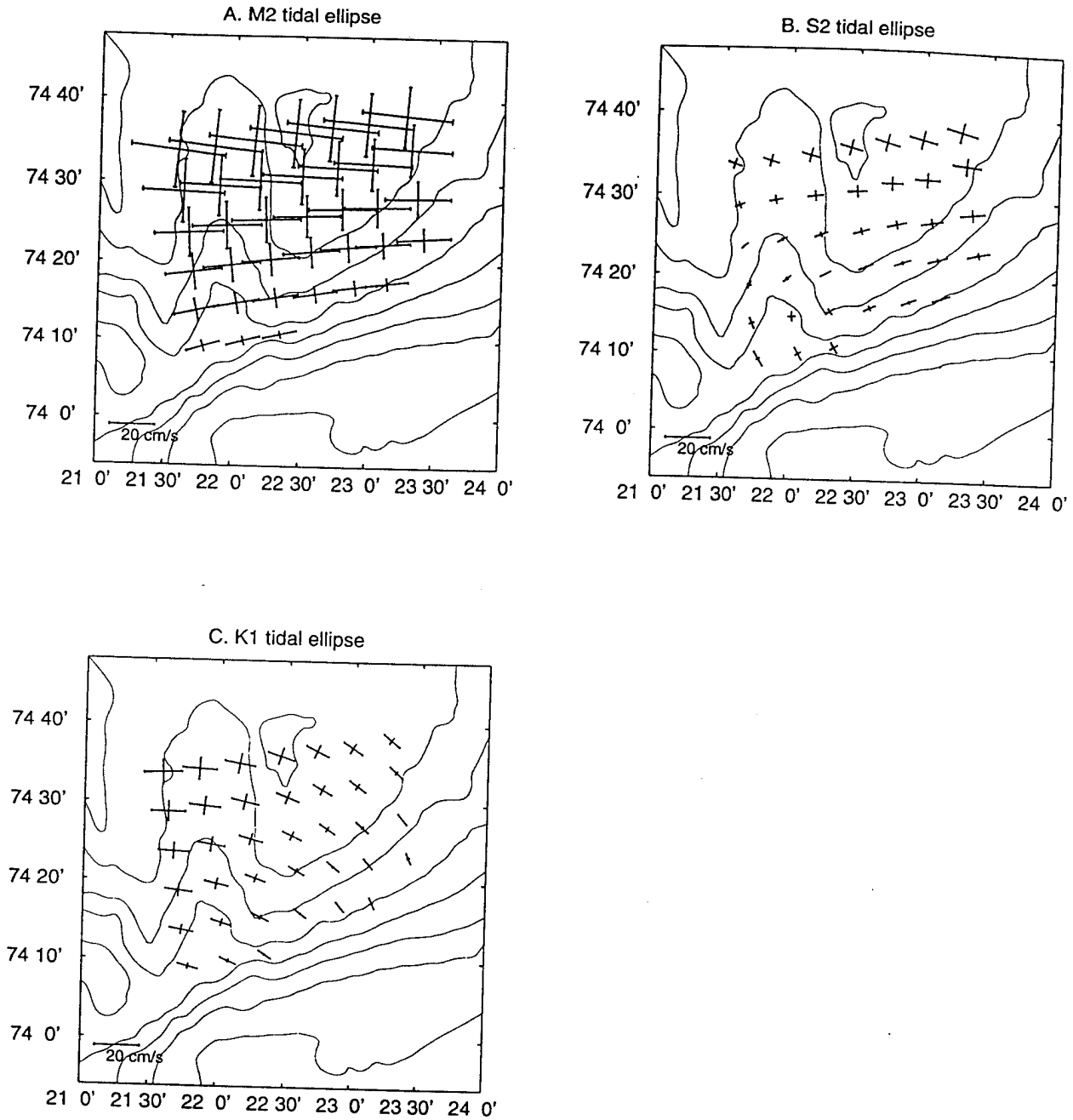


Figure 20: Plan views of model tidal ellipses from ADCP data at 50 m depth. Shown are (A) M_2 tidal ellipses, (B) S_2 tidal ellipses, and (C) K_1 tidal ellipses. Compare with Figure 10.

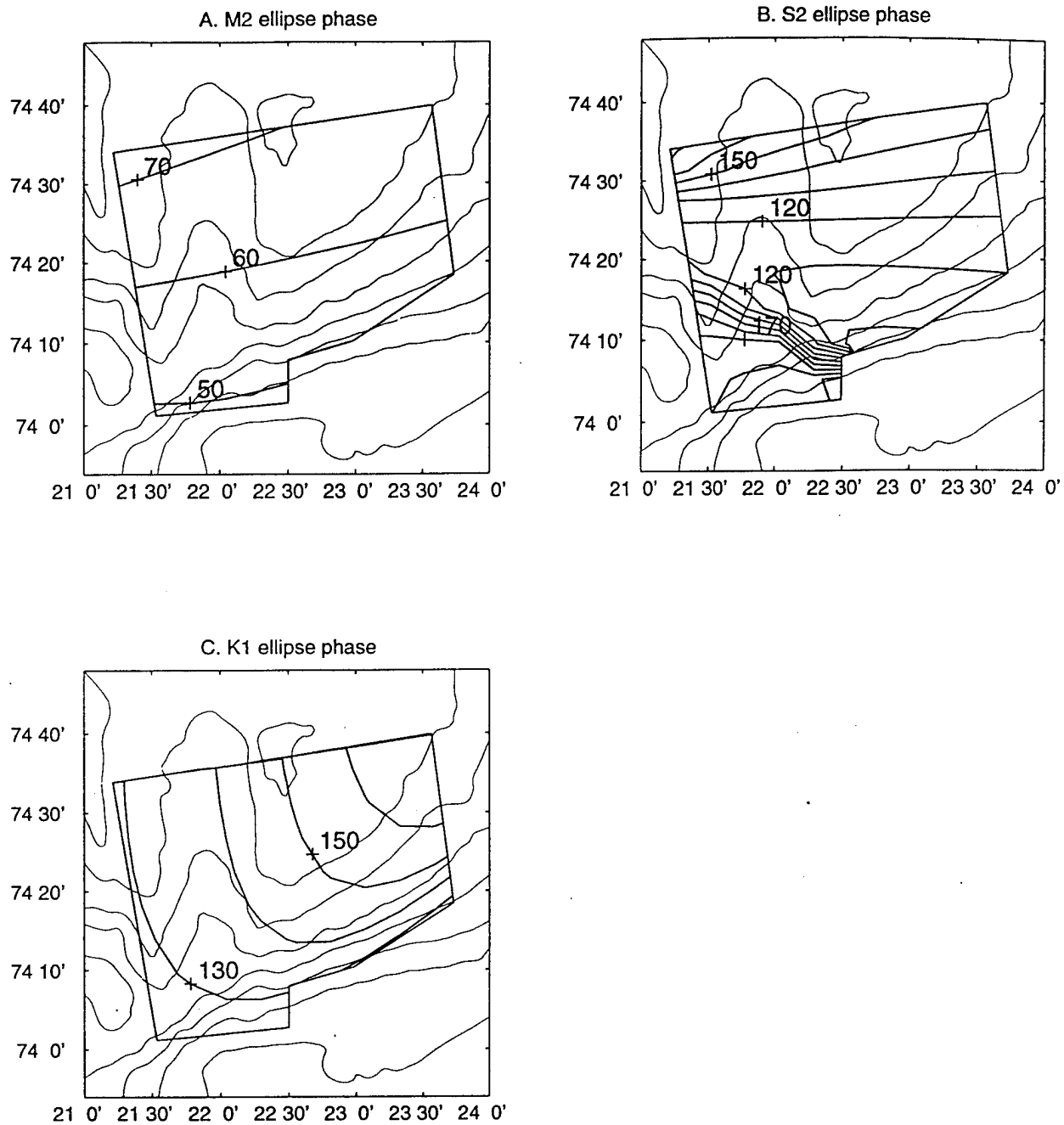


Figure 21: Plan views of model tidal phases from ADCP data at 50 m depth. Shown are (A) M_2 tidal phase, (B) S_2 tidal phase, and (C) K_1 tidal phase. Compare with Figure 11.

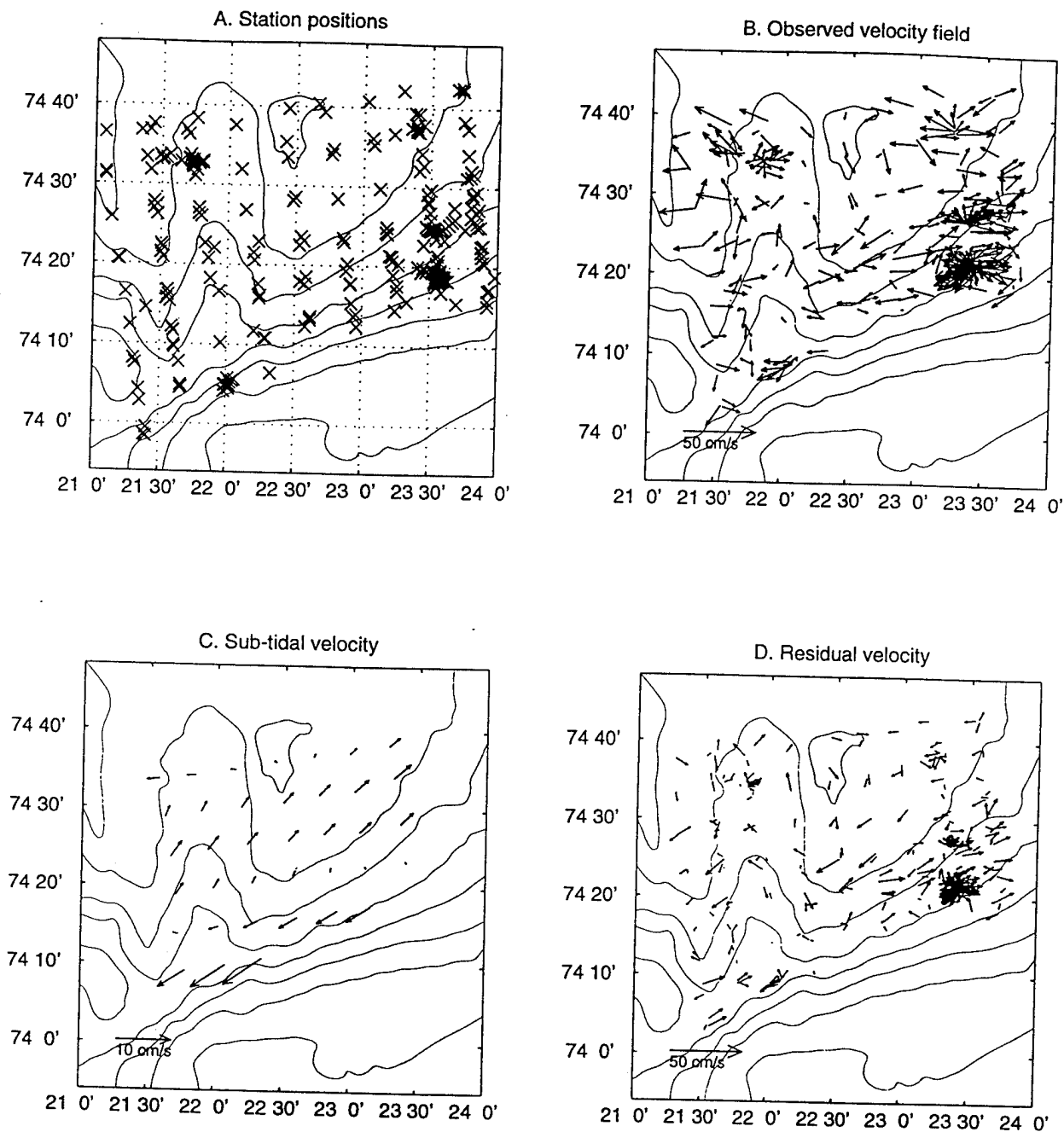


Figure 22: Plan views of ADCP velocities from 80 m depth. Shown are (A) input data positions, (B) input current vectors, (C) sub-tidal steady velocity, and (D) model residual velocity.

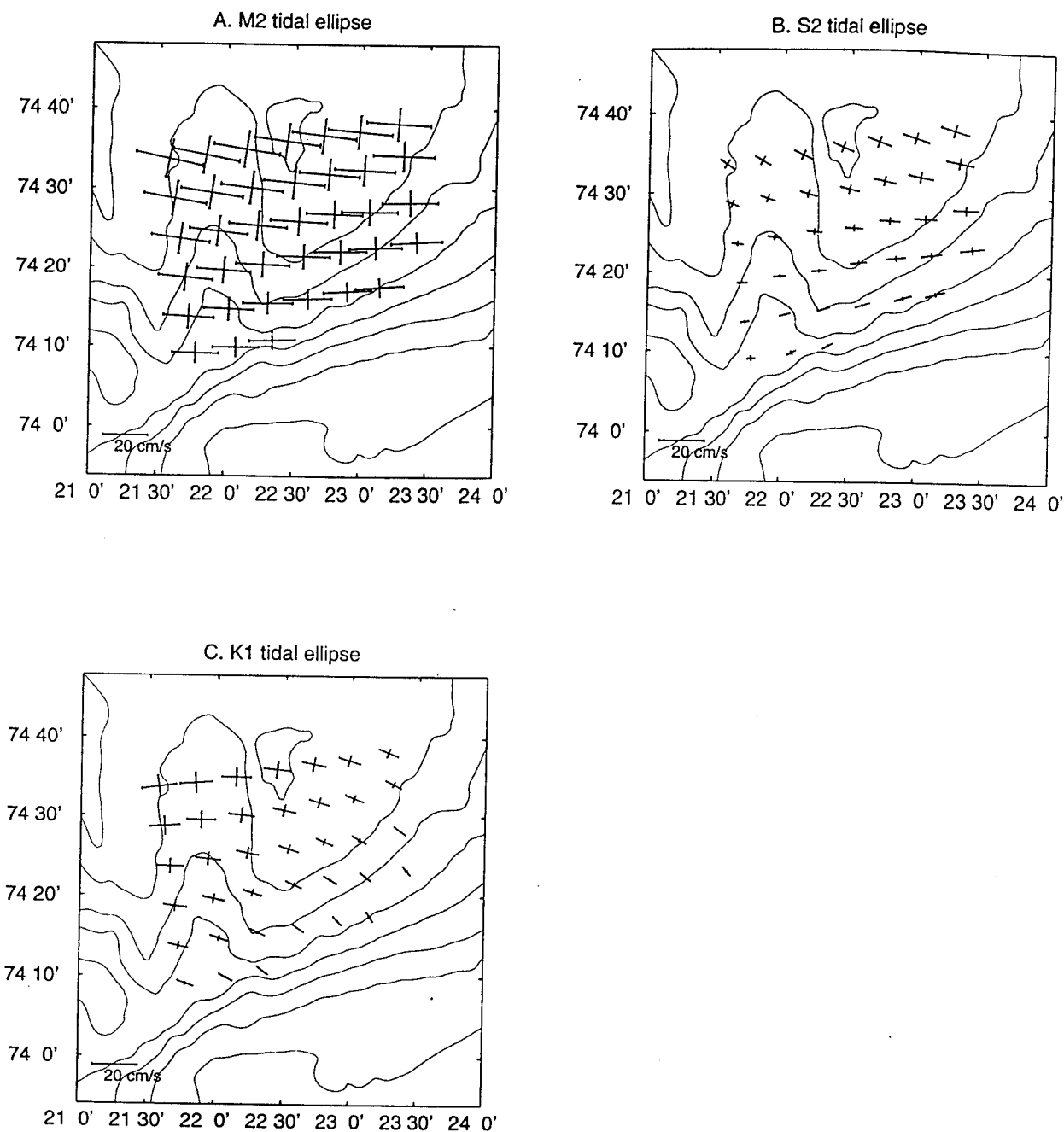


Figure 23: Plan views of model tidal ellipses from ADCP data at 80 m depth. Shown are (A) M_2 tidal ellipses, (B) S_2 tidal ellipses, and (C) K_1 tidal ellipses.

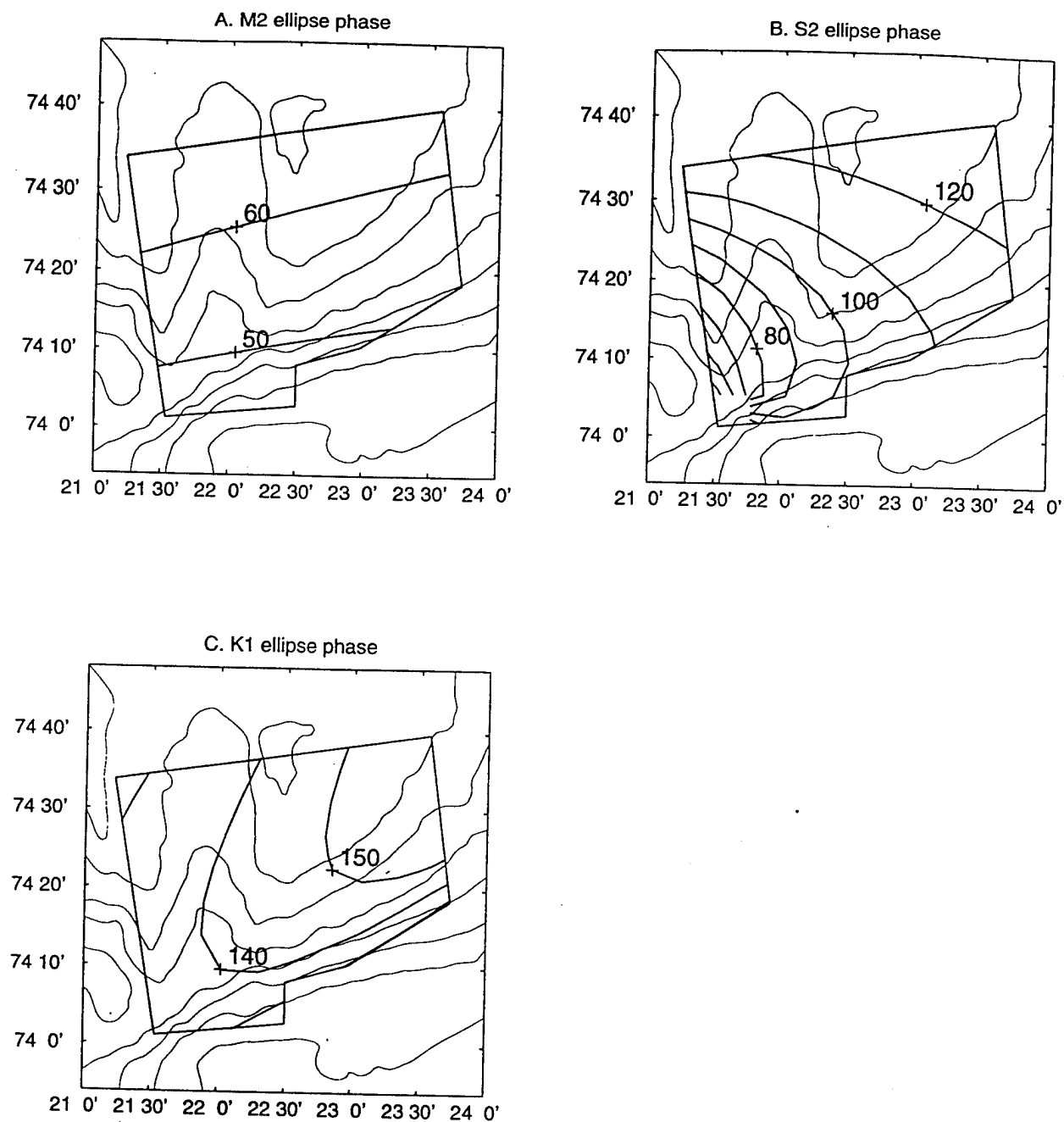


Figure 24: Plan views of model tidal phases from ADCP data at 80 m depth. Shown are (A) M₂ tidal phase, (B) S₂ tidal phase, and (C) K₁ tidal phase.

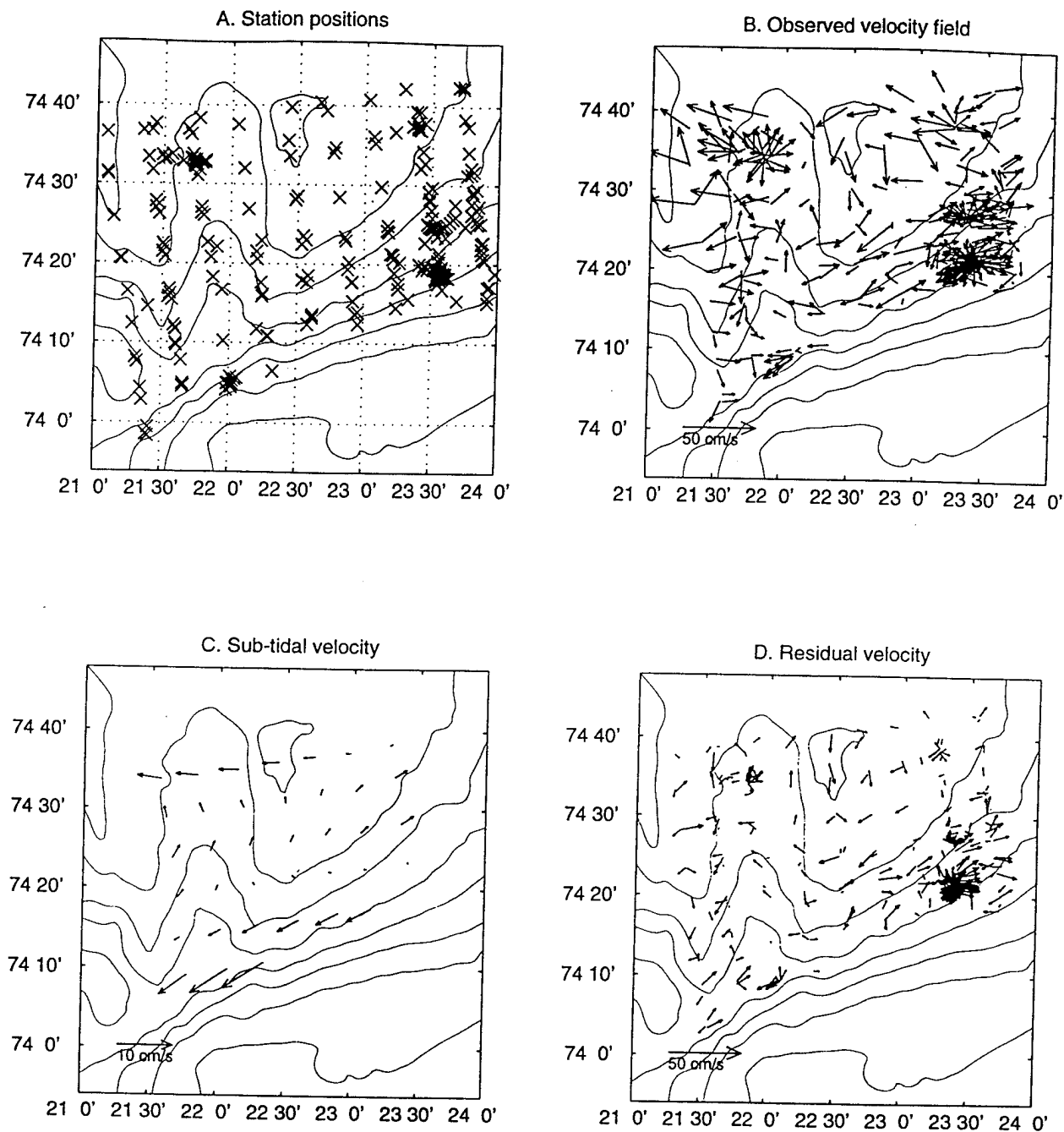


Figure 25: Plan views of ADCP velocities averaged over 20 m, 50 m, and 80 m depth. Shown are (A) input data positions, (B) input current vectors, (C) sub-tidal steady velocity, and (D) model residual velocity.

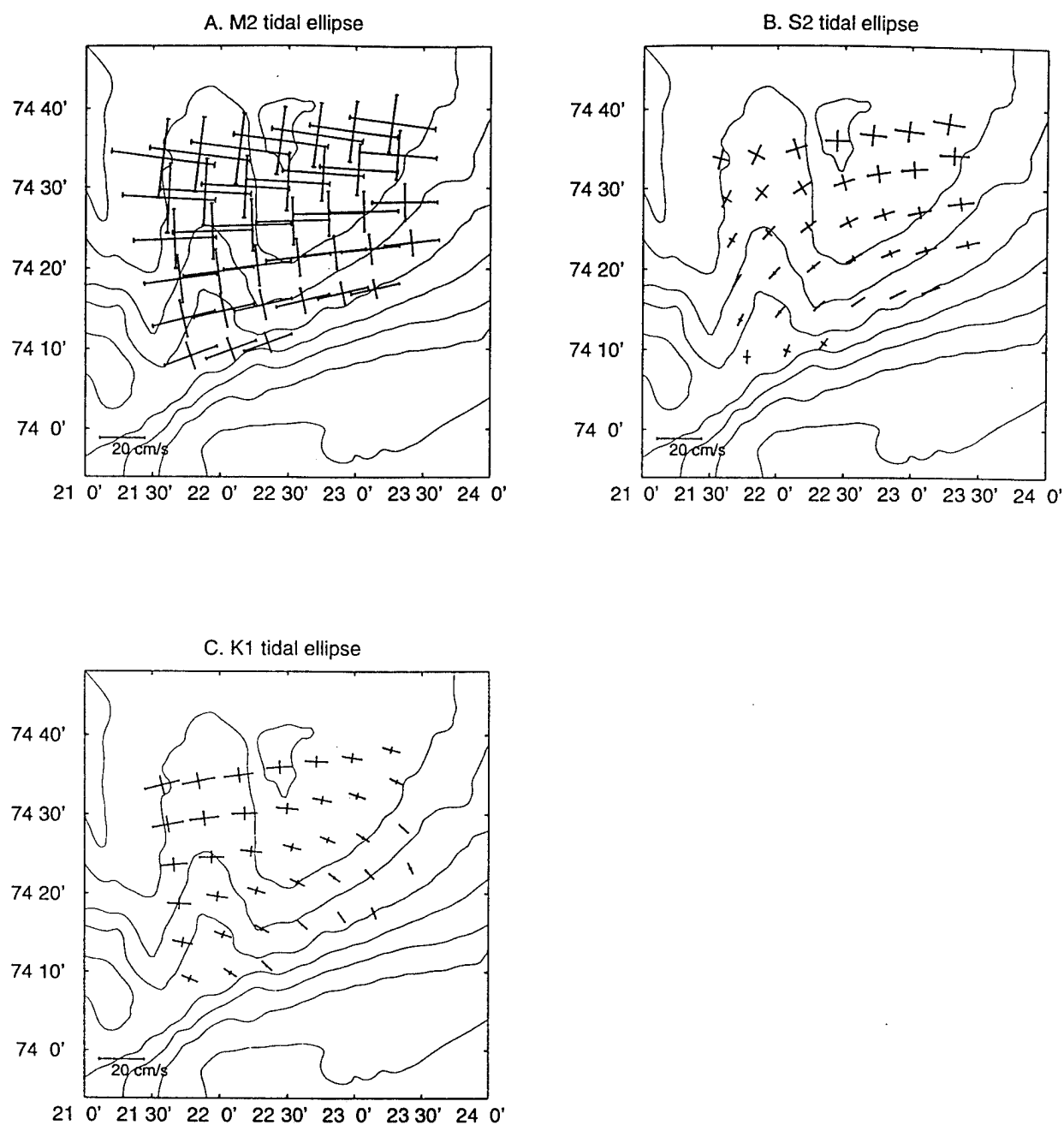


Figure 26: Plan views of model tidal ellipses from ADCP data averaged over 20 m, 50 m, and 80 m depth. Shown are (A) M₂ tidal ellipses, (B) S₂ tidal ellipses, and (C) K₁ tidal ellipses.

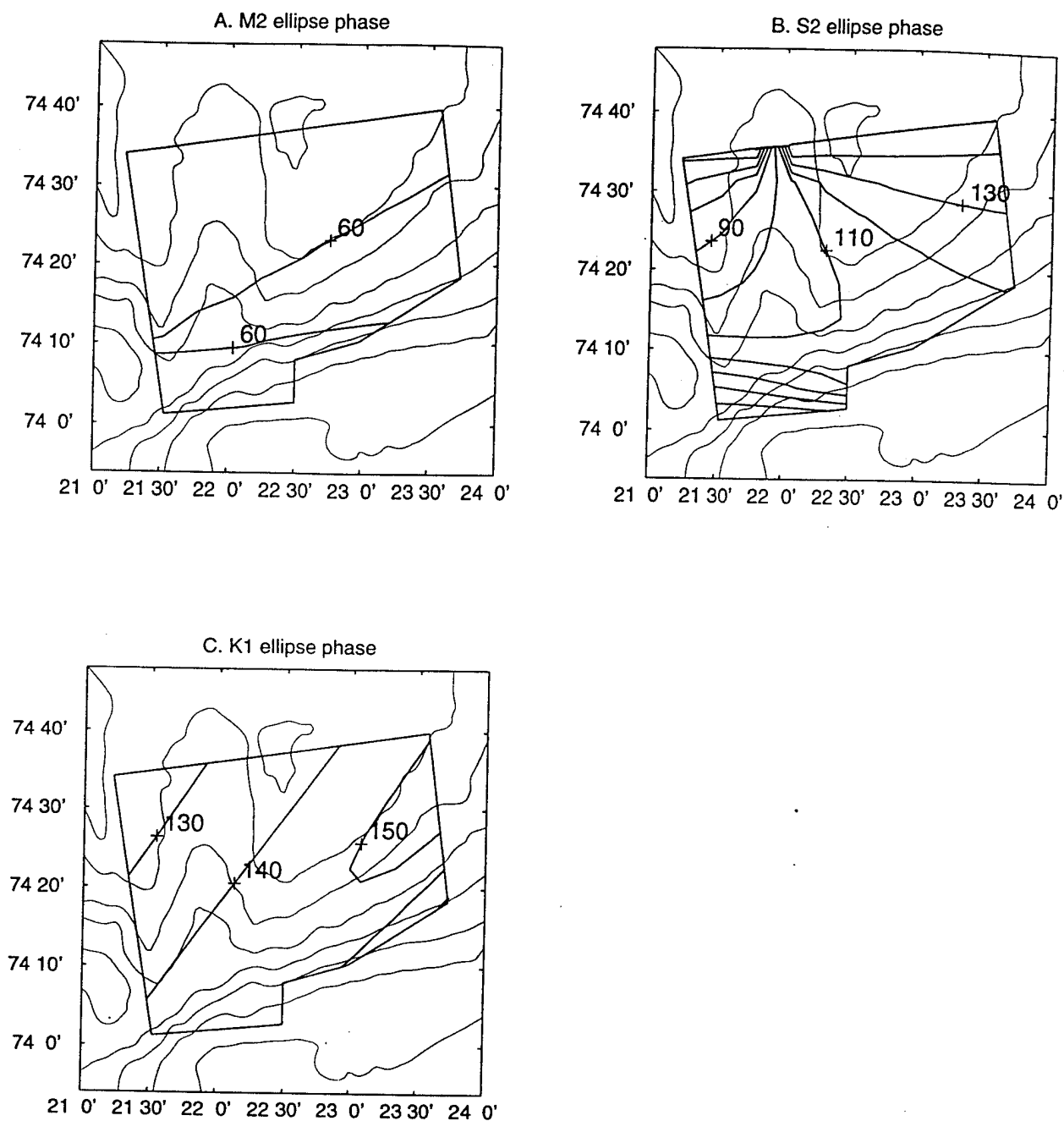


Figure 27: Plan views of model tidal phases from ADCP data averaged over 20 m, 50 m, and 80 m depth. Shown are (A) M_2 tidal phase, (B) S_2 tidal phase, and (C) K_1 tidal phase.

4.3 Combined current meter and ADCP data

In section 4.2 we found that minimizing the difference between detided ADCP data and detided current meter data indicated that the fit to the ADCP data was best when the polynomial order for the steady flow was two, the number of tidal constituents was three (M_2 , S_2 and K_1), and the polynomial order for the tides was one. Here we show the results of detiding using these parameters for the model, but with the combined current meter data and ADCP data as input. Using the combined data set restricts the analysis to the nominal current meter depths. The results of the tidal fit using the combined data set are shown in Figures 28-39 including data from 20 m depth (Figures 28-30), 50 m depth (Figures 31-33), 80 m depth (Figures 34-36) and the three depth average (Figures 37-39).

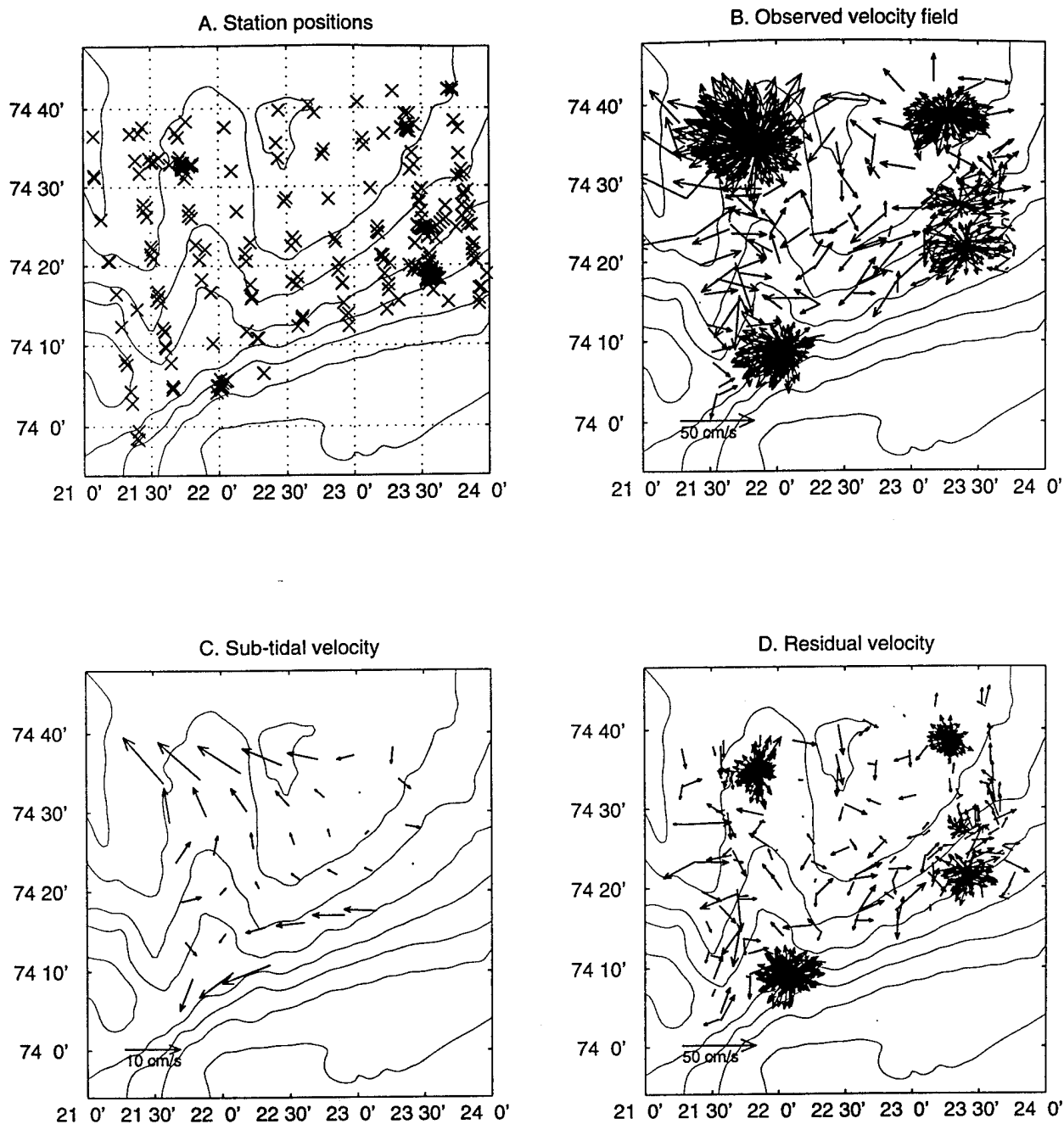


Figure 28: Plan views of velocities from the combined ADCP/current meter data set at 20 m. Shown are (A) input data positions, (B) input current vectors, (C) sub-tidal steady velocity, and (D) model residual velocity. Compare with Figures 6 and 16.

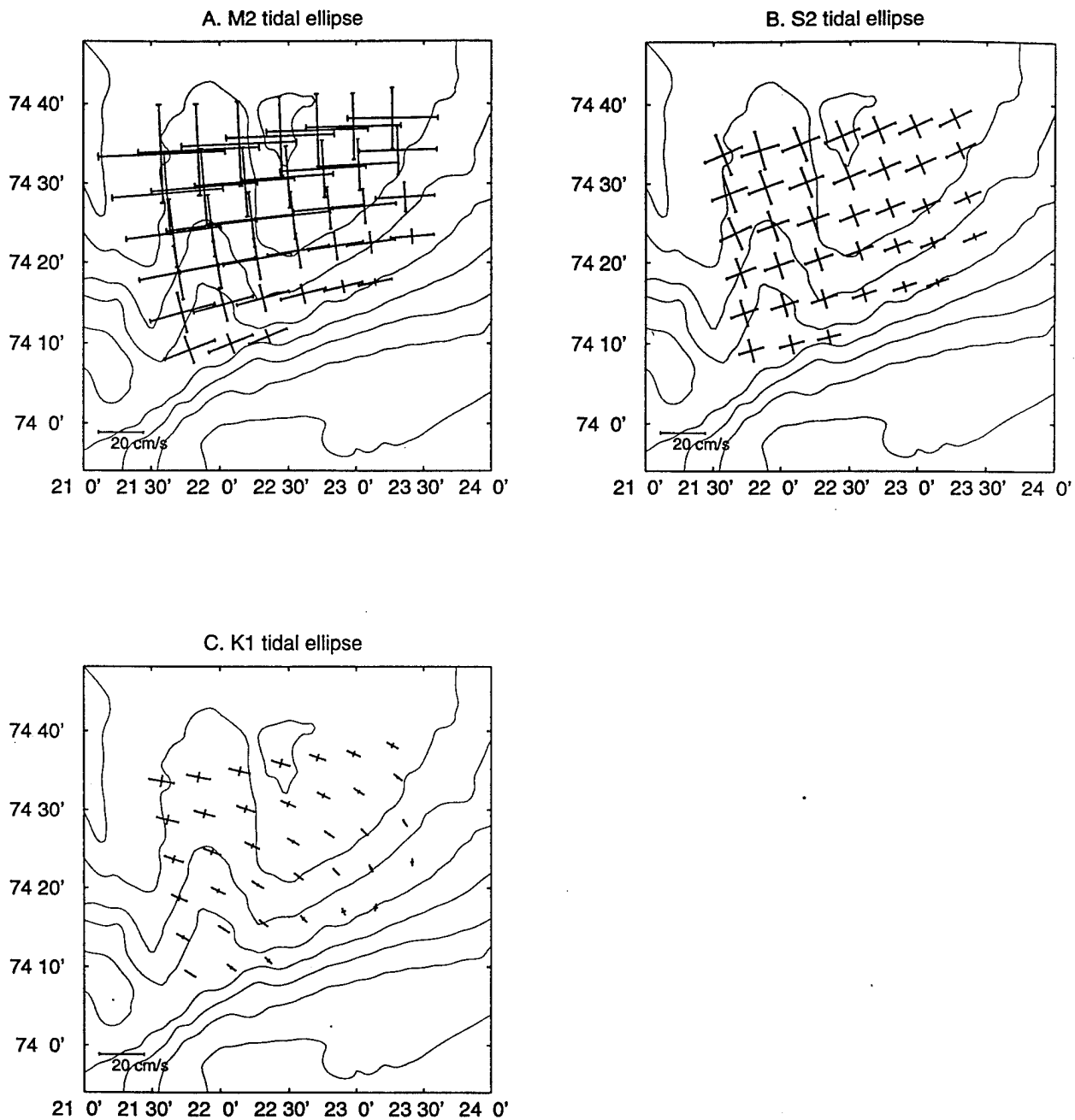


Figure 29: Plan views of model tidal ellipses from the combined ADCP/current meter data set at 20 m depth. Shown are (A) M₂ tidal ellipses, (B) S₂ tidal ellipses, and (C) K₁ tidal ellipses. Compare with Figures 7 and 17.

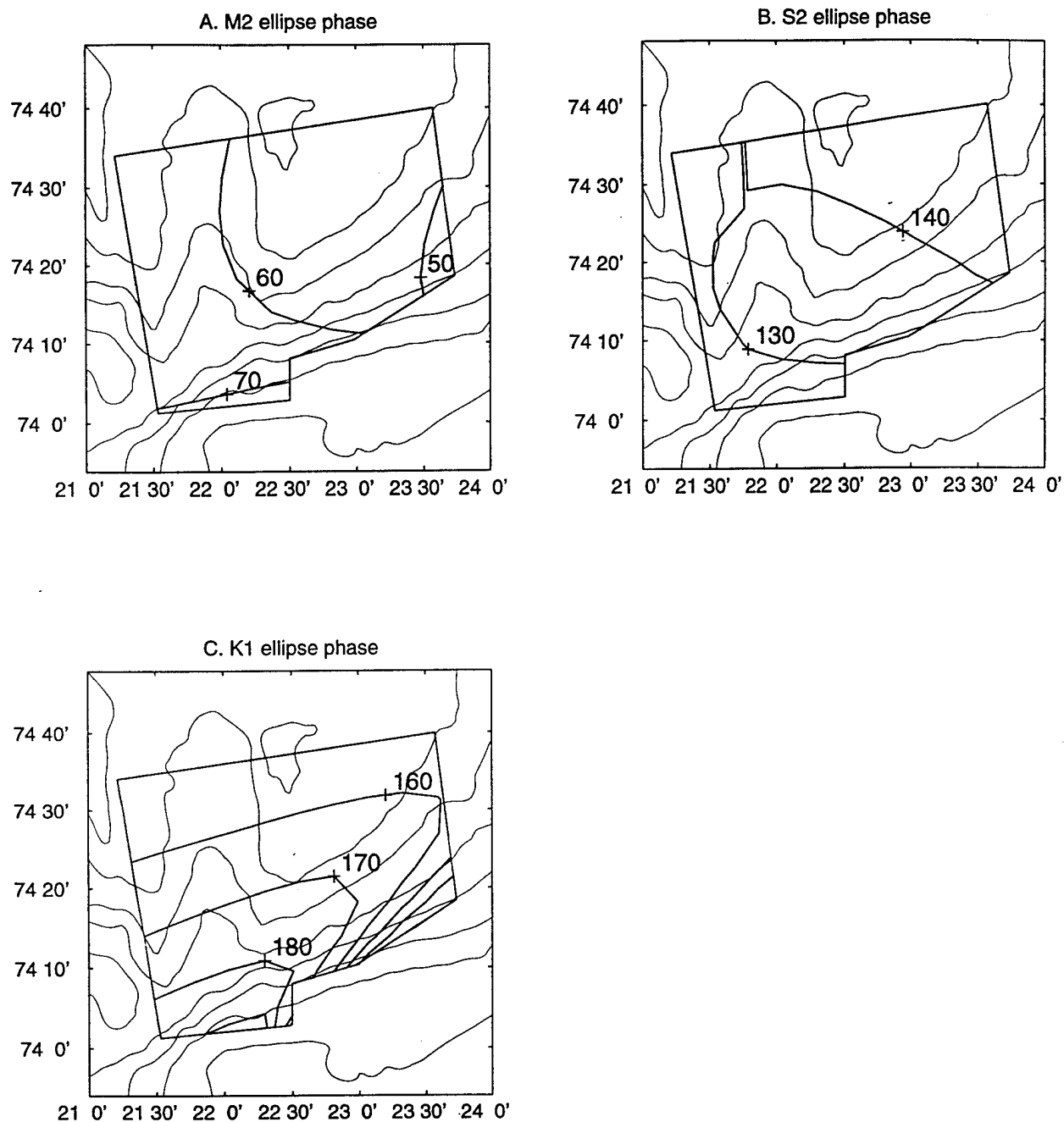


Figure 30: Plan views of model tidal phases from the combined ADCP/current meter data set at 20 m depth. Shown are (A) M_2 tidal phase, (B) S_2 tidal phase, and (C) K_1 tidal phase. Compare with Figures 8 and 18.

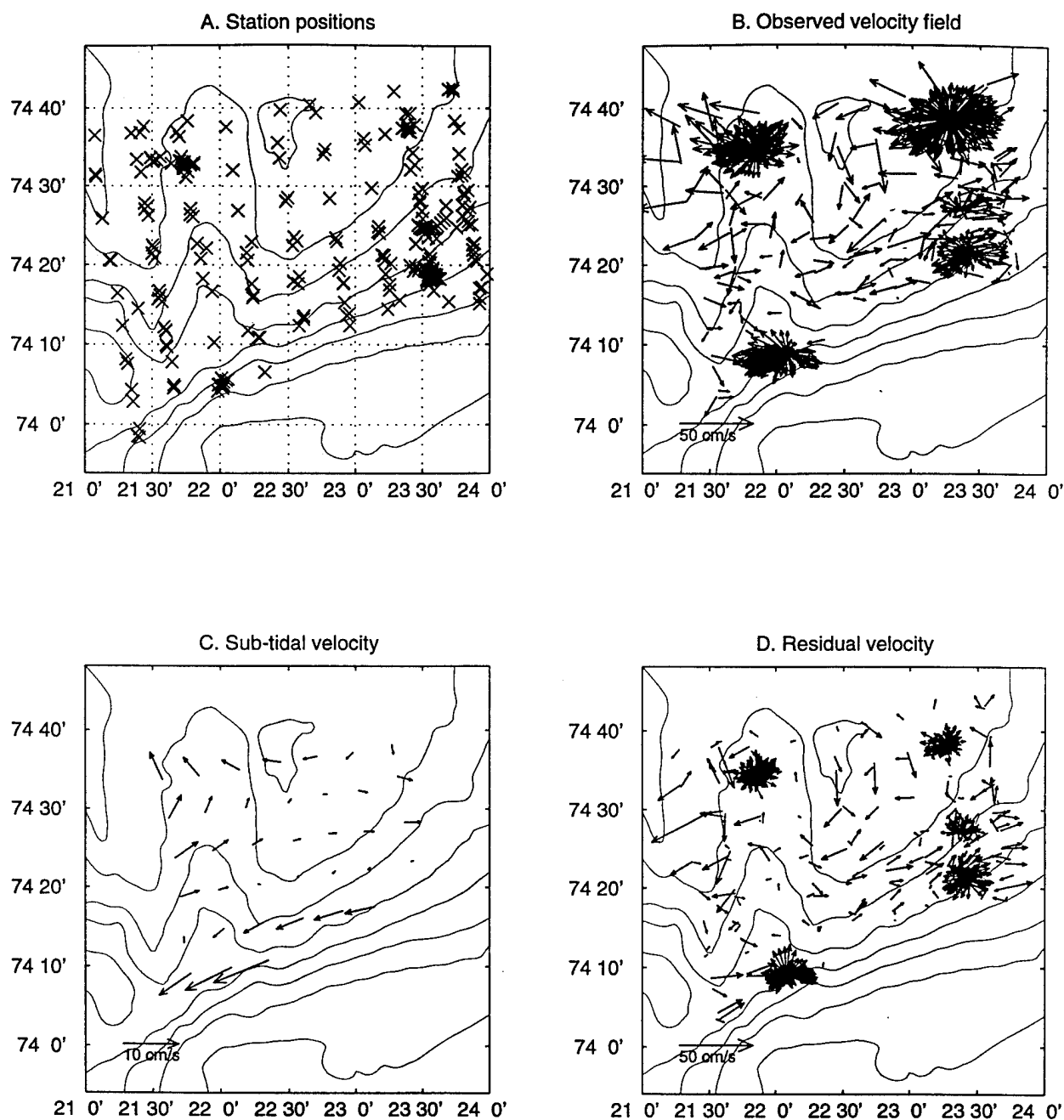


Figure 31: Plan views of velocities from the combined ADCP/current meter data set at 50 m depth. Shown are (A) input data positions, (B) input current vectors, (C) sub-tidal steady velocity, and (D) model residual velocity. Compare with Figures 9 and 19.

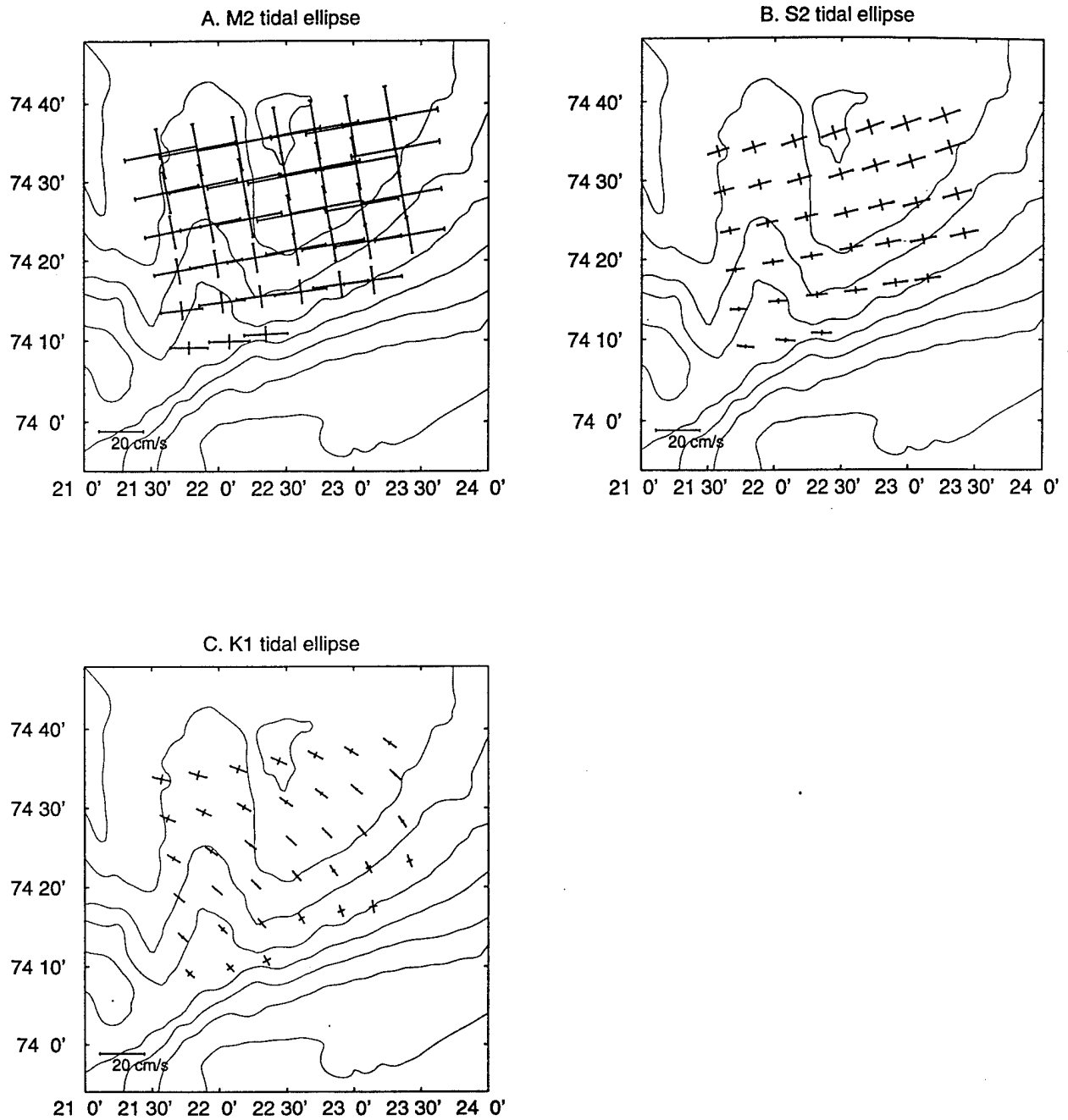


Figure 32: Plan views of model tidal ellipses from the combined ADCP/current meter data set at 50 m depth. Shown are (A) M₂ tidal ellipses, (B) S₂ tidal ellipses, and (C) K₁ tidal ellipses. Compare with Figures 10 and 20.

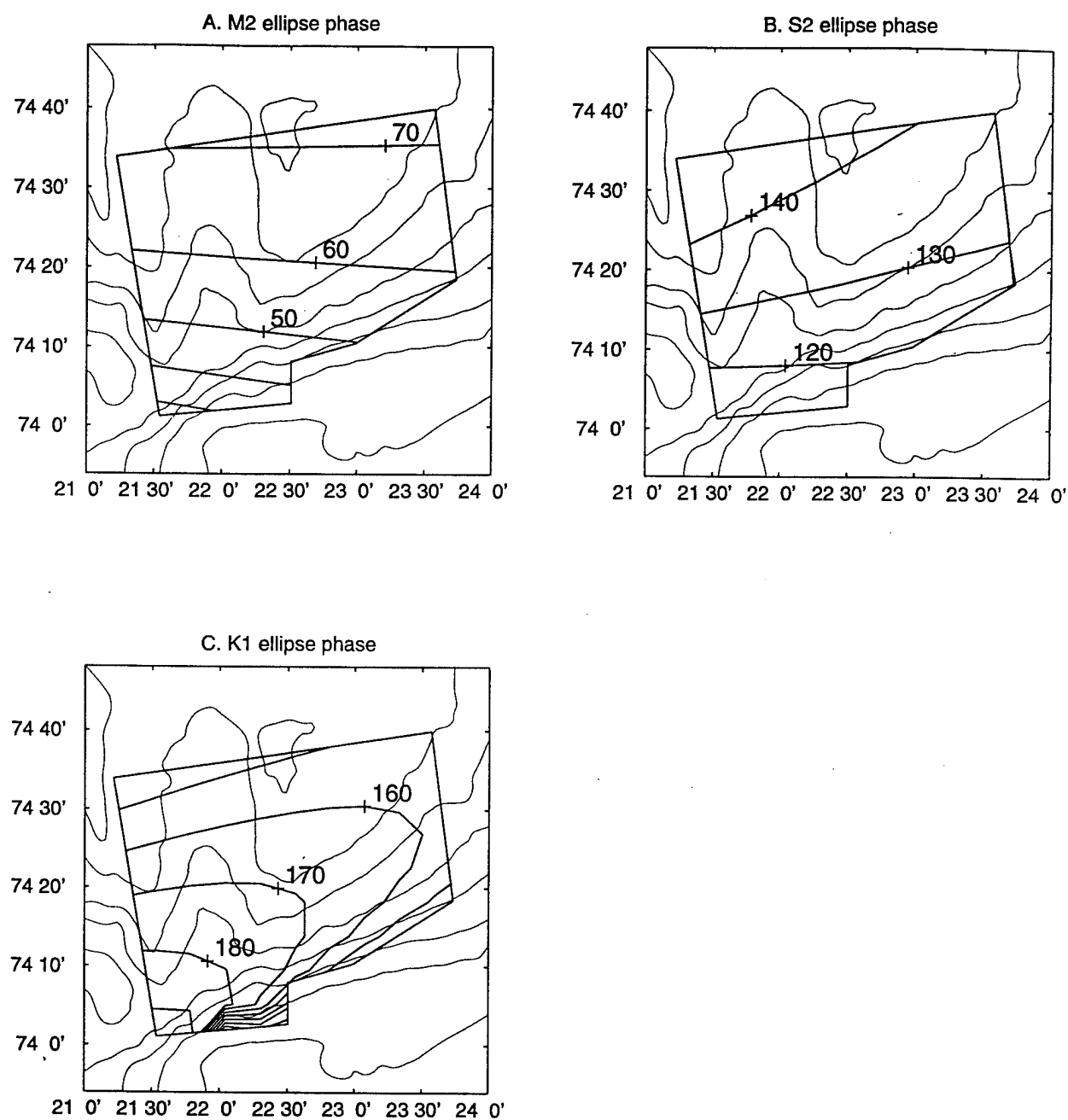


Figure 33: Plan views of model tidal phases from the ADCP/current meter combined data set at 50 m depth. Shown are (A) M_2 tidal phase, (B) S_2 tidal phase, and (C) K_1 tidal phase. Compare with Figures 11 and 21.

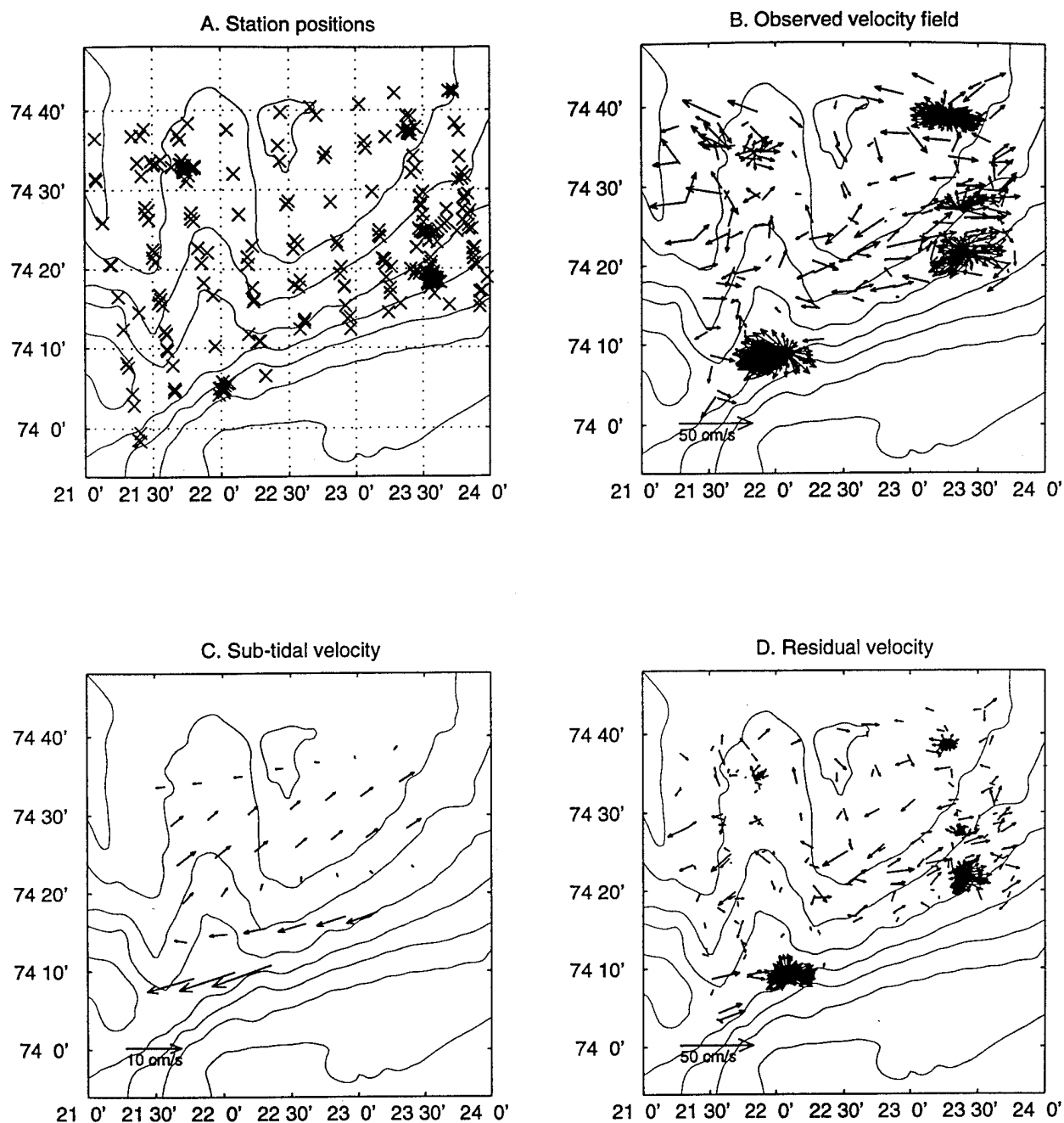


Figure 34: Plan views of velocities from the combined ADCP/current meter data set at 80 m depth. Shown are (A) input data positions, (B) input current vectors, (C) sub-tidal steady velocity, and (D) model residual velocity. Compare with Figure 22.

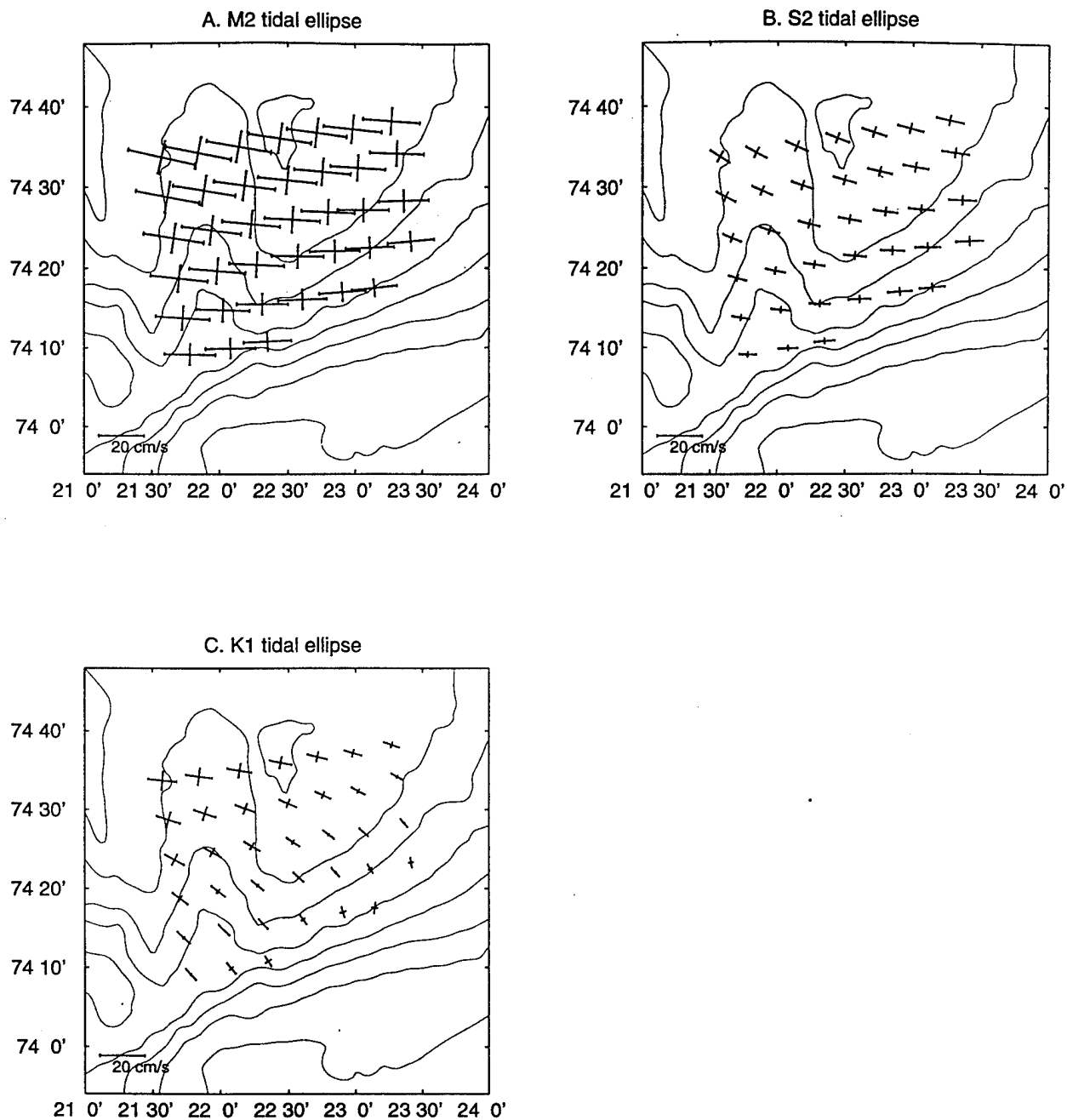


Figure 35: Plan views of model tidal ellipses from the combined ADCP/current meter data set at 80 m depth. Shown are (A) M₂ tidal ellipses, (B) S₂ tidal ellipses, and (C) K₁ tidal ellipses. Compare with Figure 23.

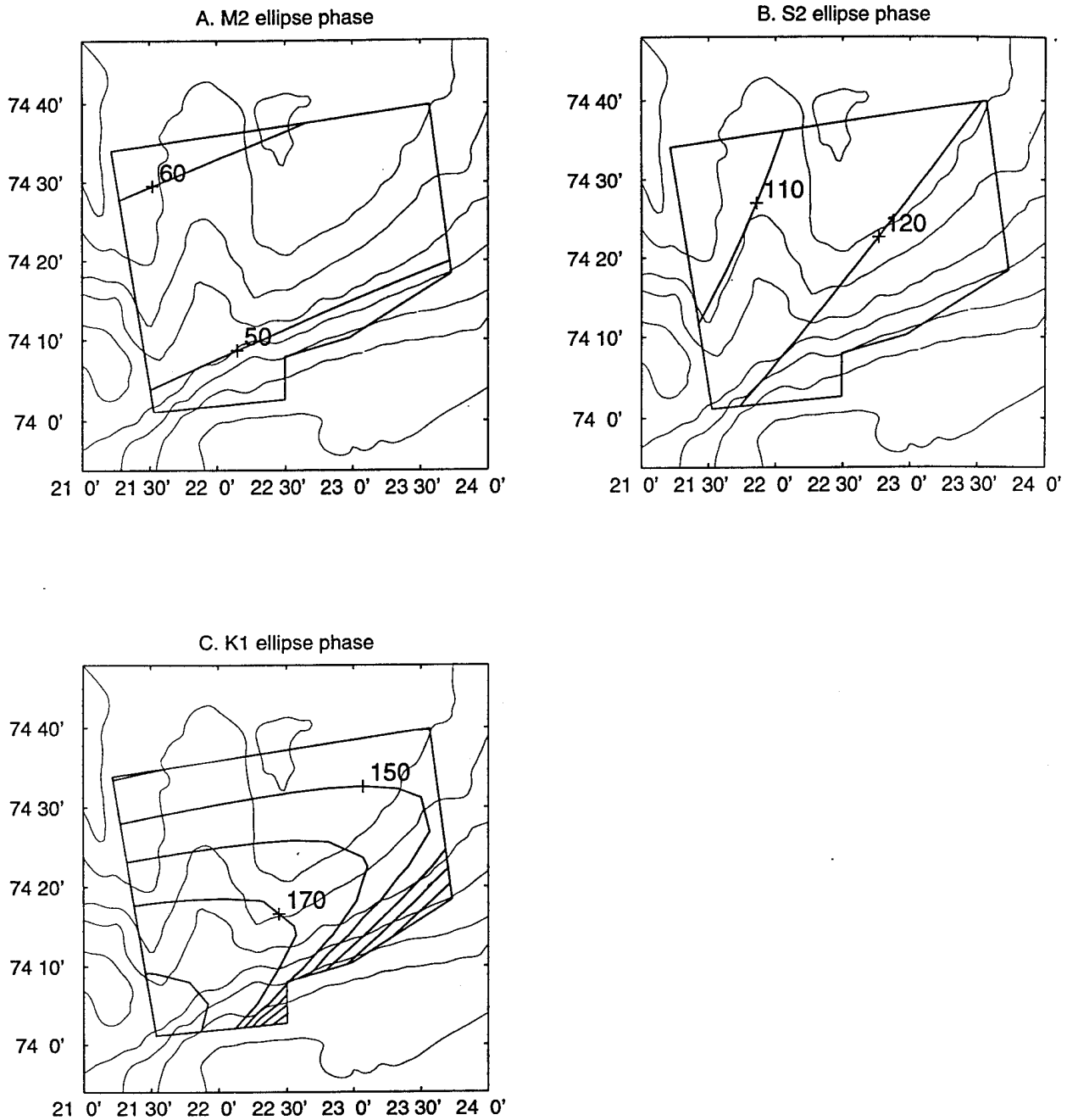


Figure 36: Plan views of model tidal phases from the combined ADCP/current meter data set at 80 m depth. Shown are (A) M_2 tidal phase, (B) S_2 tidal phase, and (C) K_1 tidal phase. Compare with Figure 24.

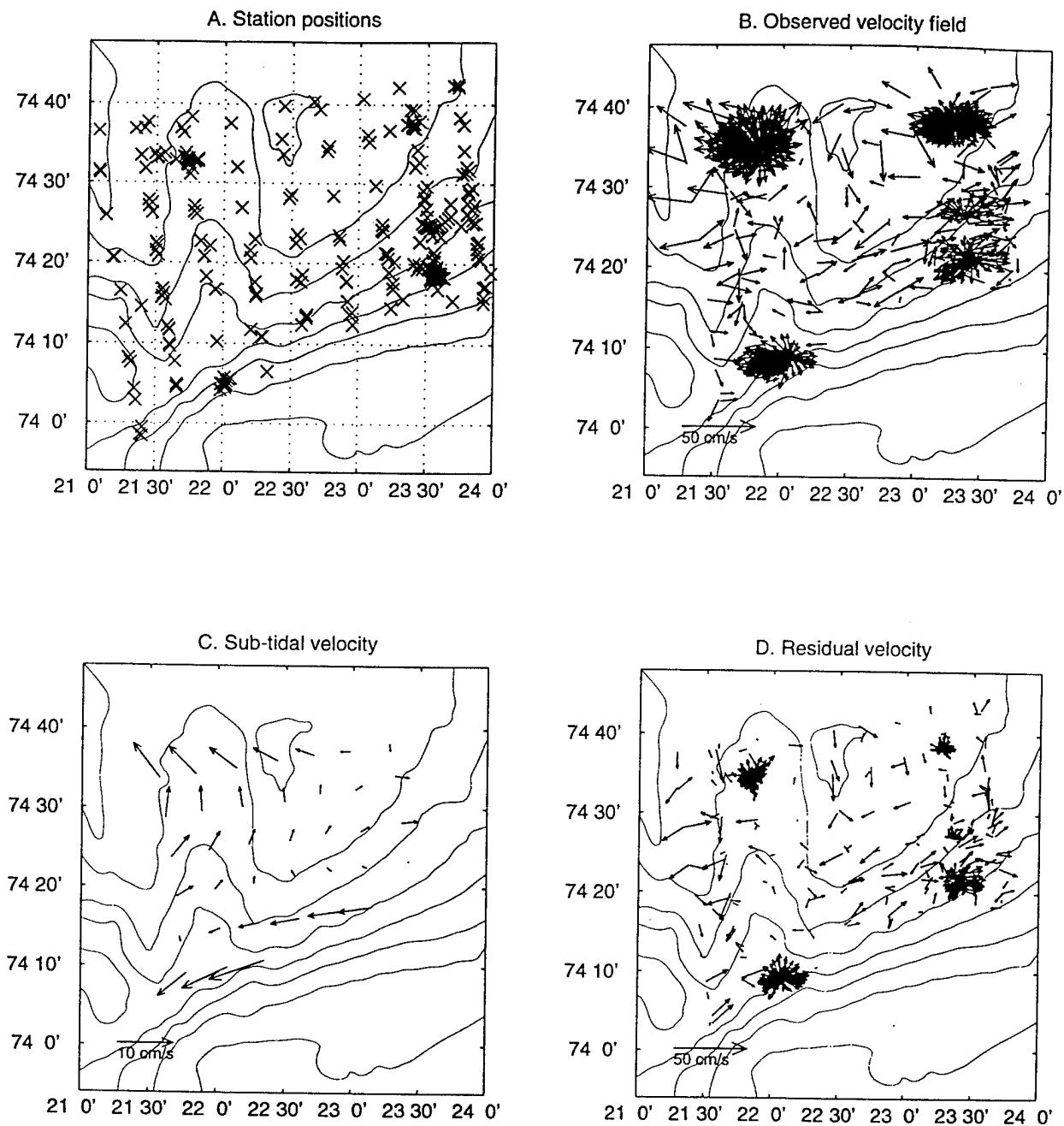


Figure 37: Plan views of velocities from the combined ADCP/current meter data set averaged over 20 m, 50 m, and 80 m depth. Shown are (A) input data positions, (B) input current vectors, (C) sub-tidal steady velocity, and (D) model residual velocity. Compare with Figure 25.

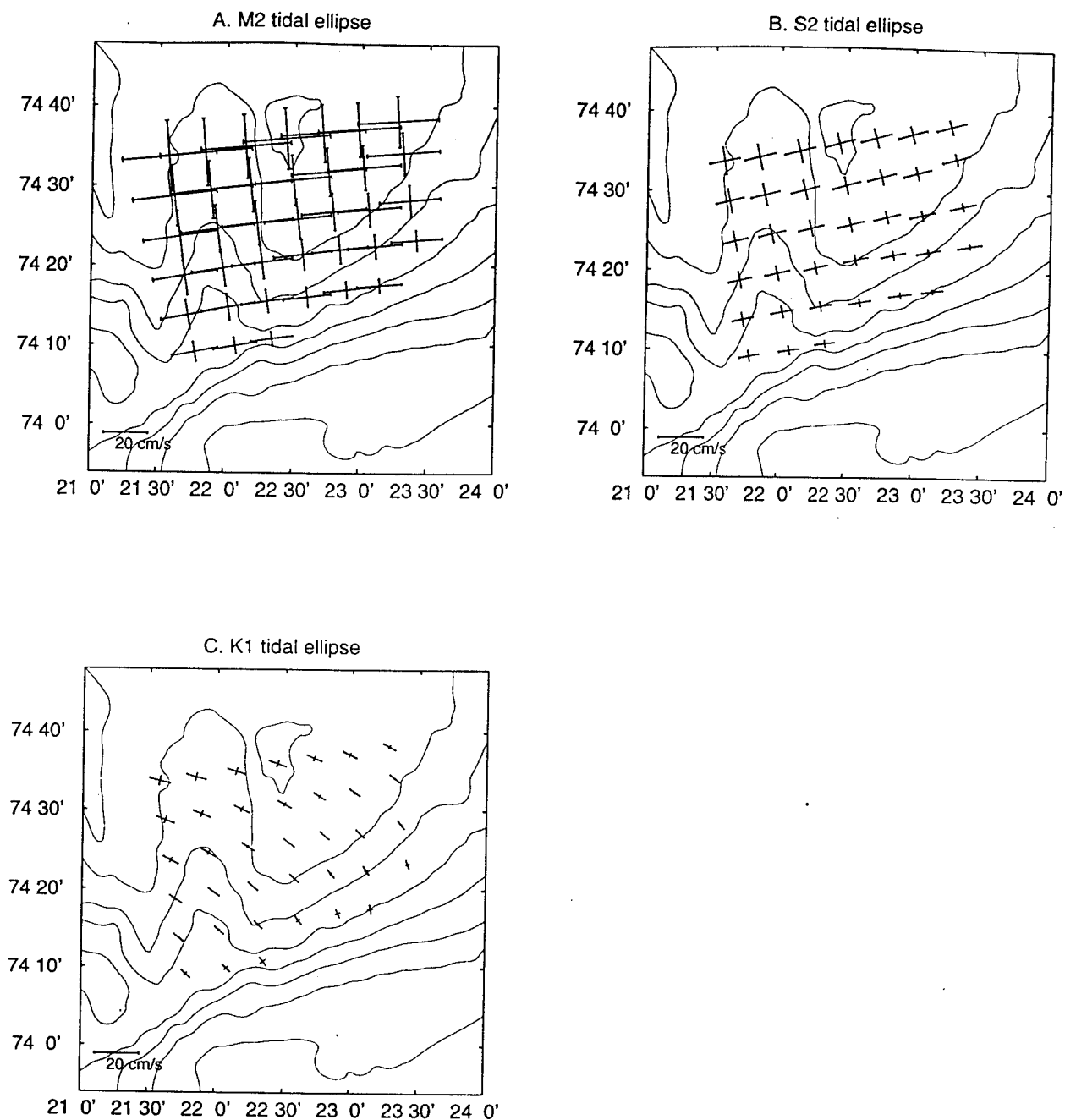


Figure 38: Plan views of model tidal ellipses from the combined ADCP/current meter data set averaged over 20 m, 50 m, and 80 m depth. Shown are (A) M_2 tidal ellipses, (B) S_2 tidal ellipses, and (C) K_1 tidal ellipses. Compare with Figure 26.

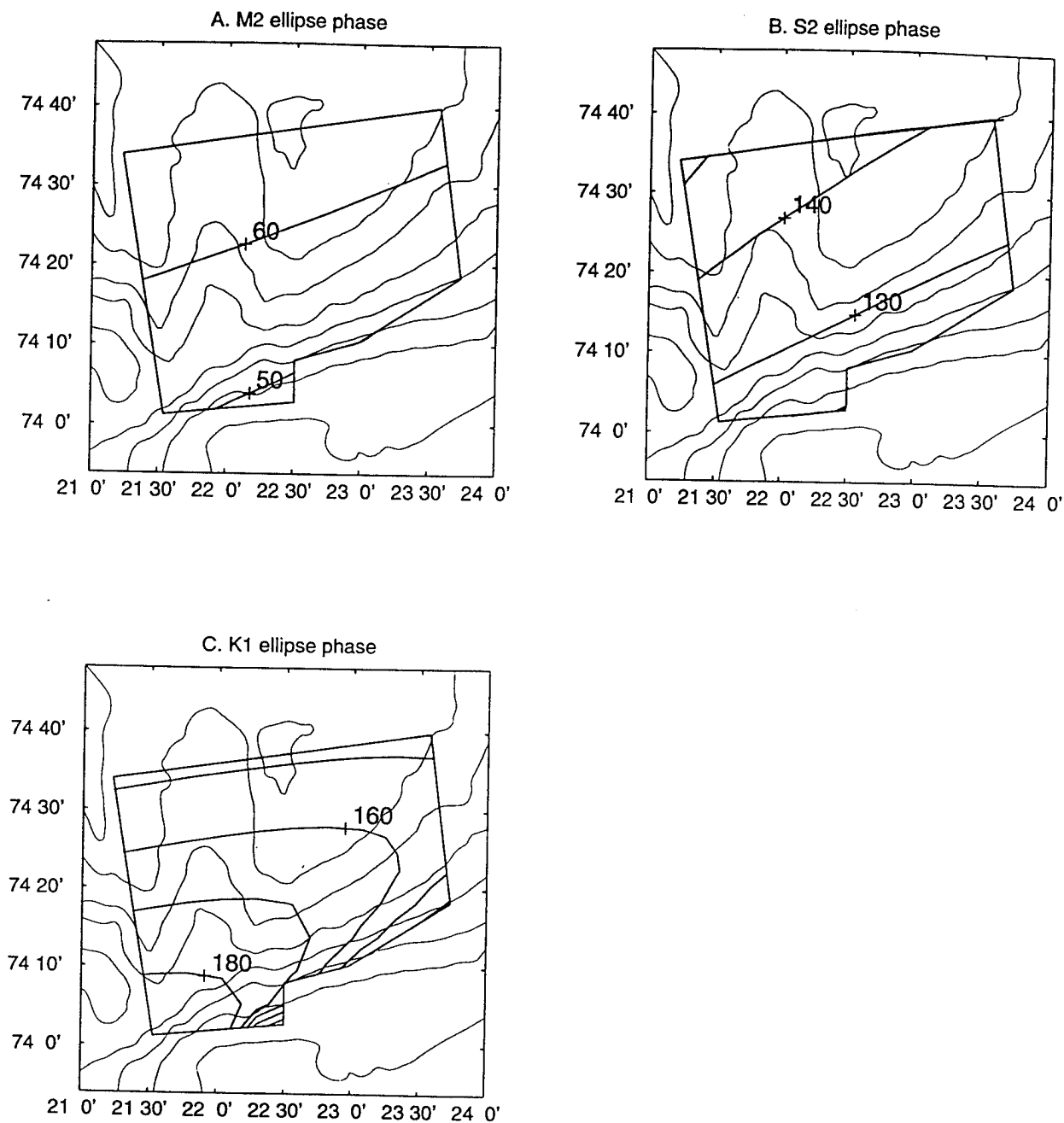


Figure 39: Plan views of model tidal phases from the combined ADCP/current meter data set averaged over 20 m, 50 m, and 80 m depth. Shown are (A) M_2 tidal phase, (B) S_2 tidal phase, and (C) K_1 tidal phase. Compare with Figure 27.

4.4 Sub-tidal error estimates

In this section we first evaluate the effectiveness of the tidal model by considering the reduction of tidal energy after the model fit, and second evaluate the standard error of the sub-tidal flow.

Examining the residual fields (Figures 6, 9, 12, 16, 19, 22, 25, 28, 31, 34, and 37) shows that the residual velocities are of the same order as the sub-tidal flow and that they appear to have periodicity at tidal frequencies. This prompts a further look at the spectral characteristics of the residual field in comparison to the input data and the model fit. The velocity component spectra from a model run with the depth averaged current meter data as input are shown in Figure 40. The spectra confirm that the model captures the majority of the energy in the diurnal and semi-diurnal bands. Comparing the residual to the input data shows that the tidal energy is reduced by about a factor of 10 in the diurnal band and a factor of 100 in the semi-diurnal band. Despite the hundred-fold reduction in energy density, the semi-diurnal peak is still discernable in the residual spectra and accounts for the periodicity in the velocity time series.

The calculation of standard error for the sub-tidal flow is guided by the discussion in Candela *et al.* (1992). Their notation is used here. To calculate the errors, it is necessary to know the number of degrees of freedom in the data. The number of degrees of freedom can be found using the integral of the autocorrelation function of the observations. Due to the periodicity of the tides, the tidal part of the observations has a different number of degrees of freedom than the rest of the data. Therefore, it is necessary to remove the tidal signal from the observations before calculating the number of degrees of freedom.

To this end, the ADCP observations (\mathbf{u} , \mathbf{v}) were low-passed with a three day filter to remove the tidal signal. The resulting time/space series (\mathbf{u}_{lp} , \mathbf{v}_{lp}), were treated as strict time series to find the autocorrelation functions. Letting τ_u be the integral of the autocorrelation coefficients of \mathbf{u}_{lp} from the zeroth lag to the first zero crossing of the autocorrelation coefficients, we calculated ν_u , the number of degrees of freedom in the sub-tidal u flow as $\nu_u = (m\Delta t/\tau_u) - n$ where Δt is the time between observations, m is the number of observation points and n is the number of model coefficients used to resolve the sub-tidal u flow field. The same was done to find ν_v . In this case, $(\tau_u, \tau_v) = (34, 20)$, $\Delta t = 1$ hour, $m = 368$ and $n = 6$ leading to $(\nu_u, \nu_v) \approx (5, 15)$.

Given the model $\mathbf{Ac} = \mathbf{d}$ where \mathbf{A} is an $(m \times n)$ model matrix which depends on the degree of polynomials chosen, \mathbf{c} is an n column vector of the unknown coefficients, and \mathbf{d} is an m column vector of the observations, the method of Candela *et al.* (1992) solves to find $\mathbf{Ac} = \hat{\mathbf{d}}$ where $\hat{\mathbf{c}}$ is the least squares approximation of \mathbf{c} and $\hat{\mathbf{d}}$ is the model estimate of the actual observations \mathbf{d} . The model residual

is $\epsilon = \mathbf{d} - \hat{\mathbf{d}}$. If \mathbf{d} represents the u velocity data then the unbiased variance estimate for the u model is $\hat{v} = \epsilon^T \epsilon / \nu_u$. Likewise for v . Estimates in $\hat{\mathbf{d}}$ then have a standard error $\mathbf{s}_{\hat{\mathbf{d}}} = \sqrt{\hat{v} \text{diag}(\mathbf{A} \mathbf{C} \mathbf{A}^T)}$ where \mathbf{C} is the covariance matrix of the coefficients $\hat{\mathbf{c}}$.

Figure 41 shows the sub-tidal standard errors from the current meter data, Figure 42 shows the standard errors from the ADCP data, and Figure 43 shows the standard error from the combined ADCP/current meter data set. When the ADCP data is used alone we particularly notice the importance of data density in the error estimates. For example, the SE corner of the survey region where the time series and dense section took place shows smaller errors than the rest of the survey region (Figure 42). We note that including the current meter data decreases the errors for two reasons. First, the current meter data have a smaller random error than the ADCP data and, second, the amount of data input to the model is tripled, allowing greater confidence in the model results. Compare Figure 41 to Figure 42 to see the smaller errors from the current meter data versus the ADCP data. Compare Figure 42 with Figure 43 to see how combining the ADCP and current meter data decreases the errors from the ADCP data alone. Finally, we note that the errors are larger at the edges of the survey region where the model polynomials are badly behaved (not shown). Model results at the western, northern, and eastern edge of the survey region are not presented because of these large errors.

It has been shown that the standard errors depend on data density, model input data, and geographic location within the survey region. Rather than laboriously interpreting each individual error field, it is suggested that for many applications of the sub-tidal velocity, more general error guidelines based on Figures 41–43 may be sufficient. Evaluation of several cases involving combined ADCP/current meter data and ADCP data alone suggests (u, v) standard errors of (5, 3) cm/s for the sub-tidal velocity field when the ADCP data is considered alone, and (3, 2) cm/s for the sub-tidal velocity field when the ADCP data is used in conjunction with the current meter data.

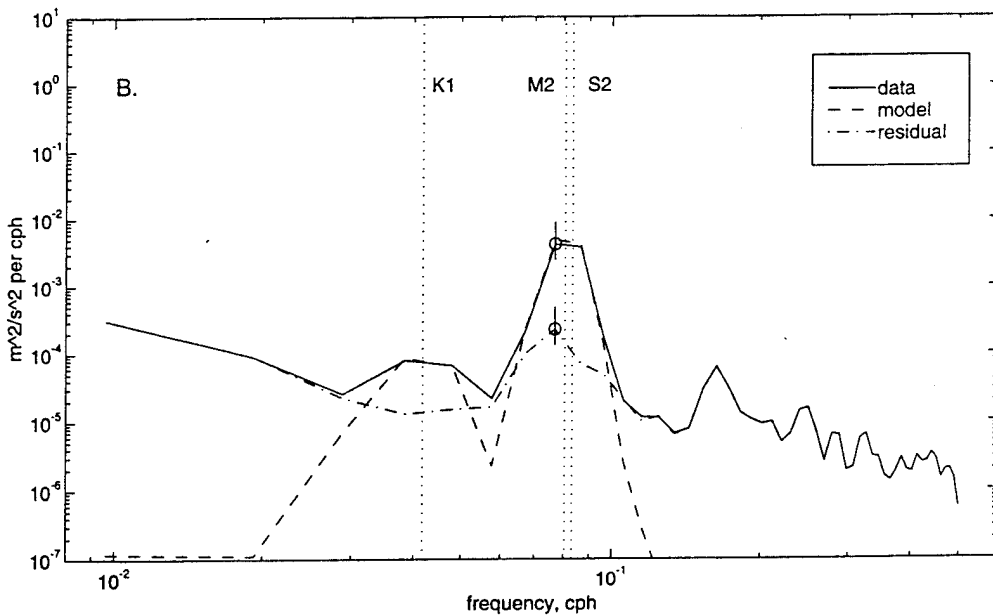
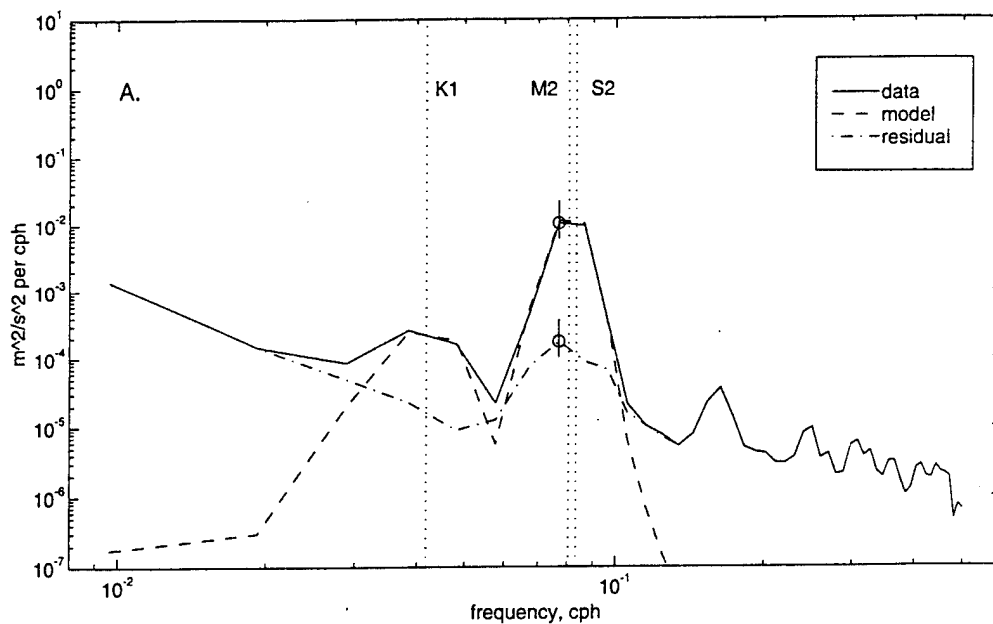


Figure 40: Power spectral density (PSD) of the depth averaged current meter (A) eastward velocity and (B) northward velocity. The PSD was calculated for the depth-averaged data at each mooring and the resulting coefficients were averaged between moorings to construct this figure. The confidence limits are at the 95% level. Shown are the observations (solid line), model tides (dashed line), and model residual (dash-dot line). The three vertical dotted lines indicate the tidal frequencies in the model.

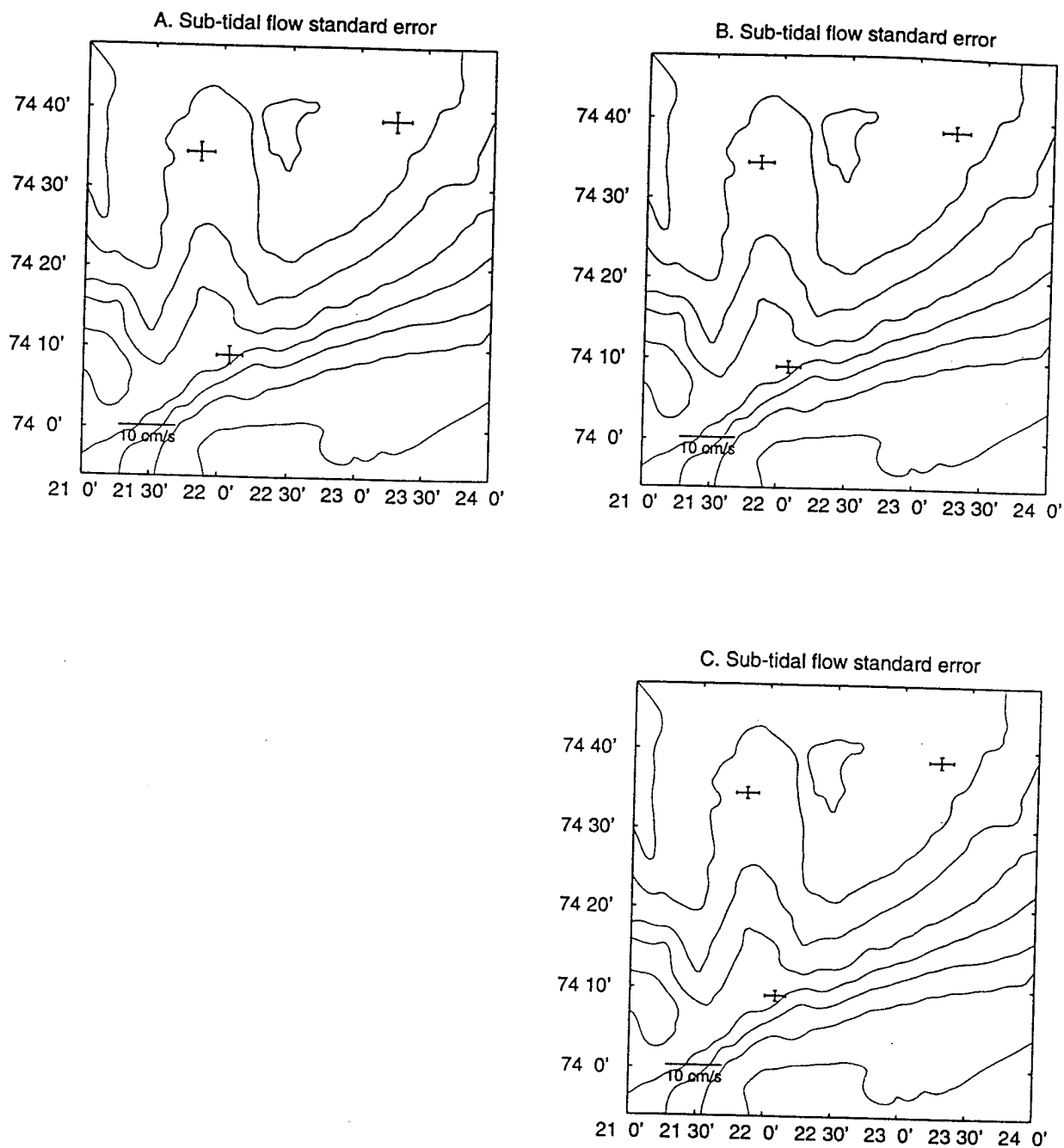


Figure 41: Standard errors of the sub-tidal flow from the current meter data at (A) 20 m depth, (B) 50 m depth, and (C) three depth average.

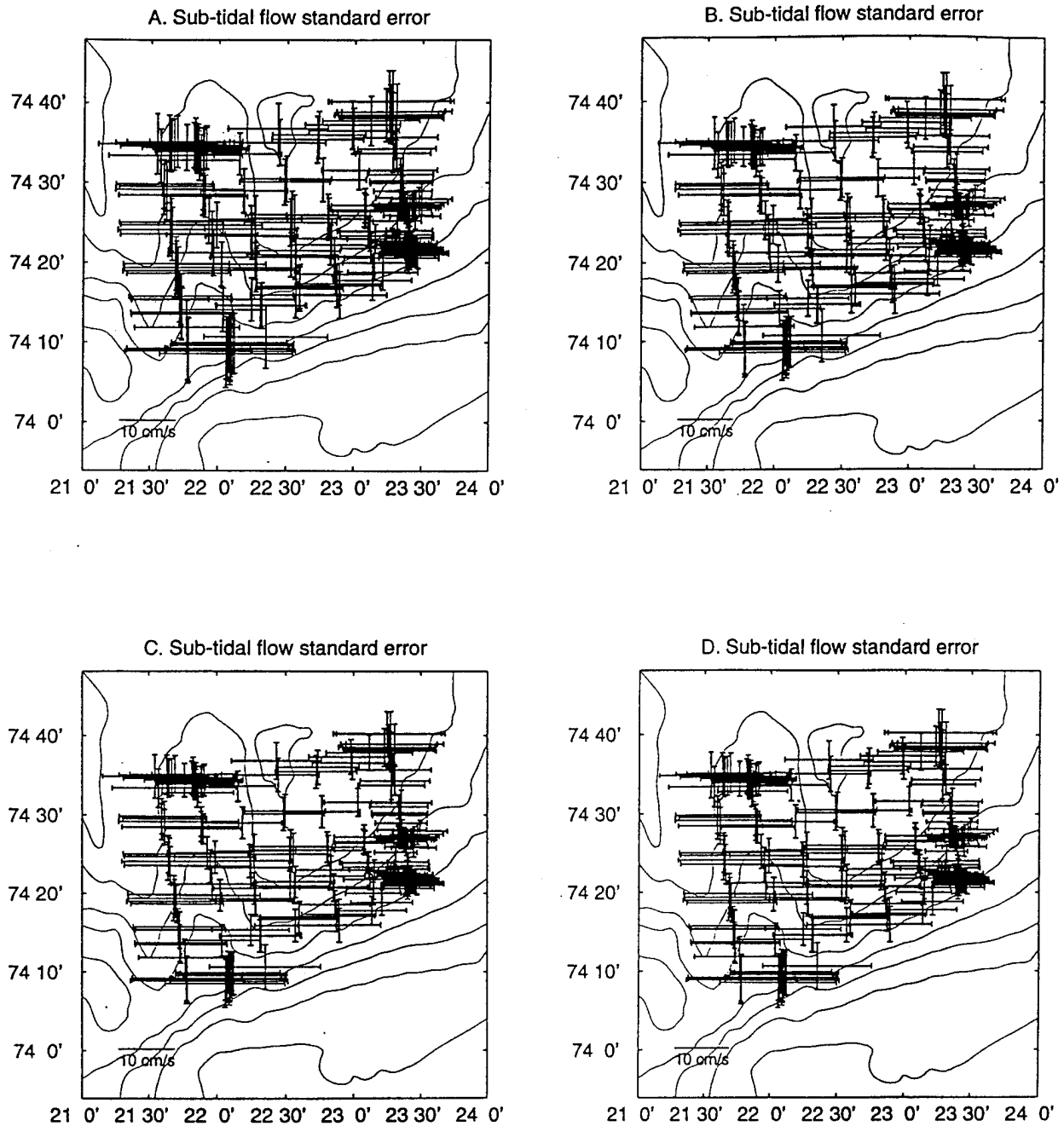


Figure 42: Standard errors of the sub-tidal flow from the ADCP data at (A) 20 m depth, (B) 50 m depth, (C) 80 m depth, and (D) three depth average.

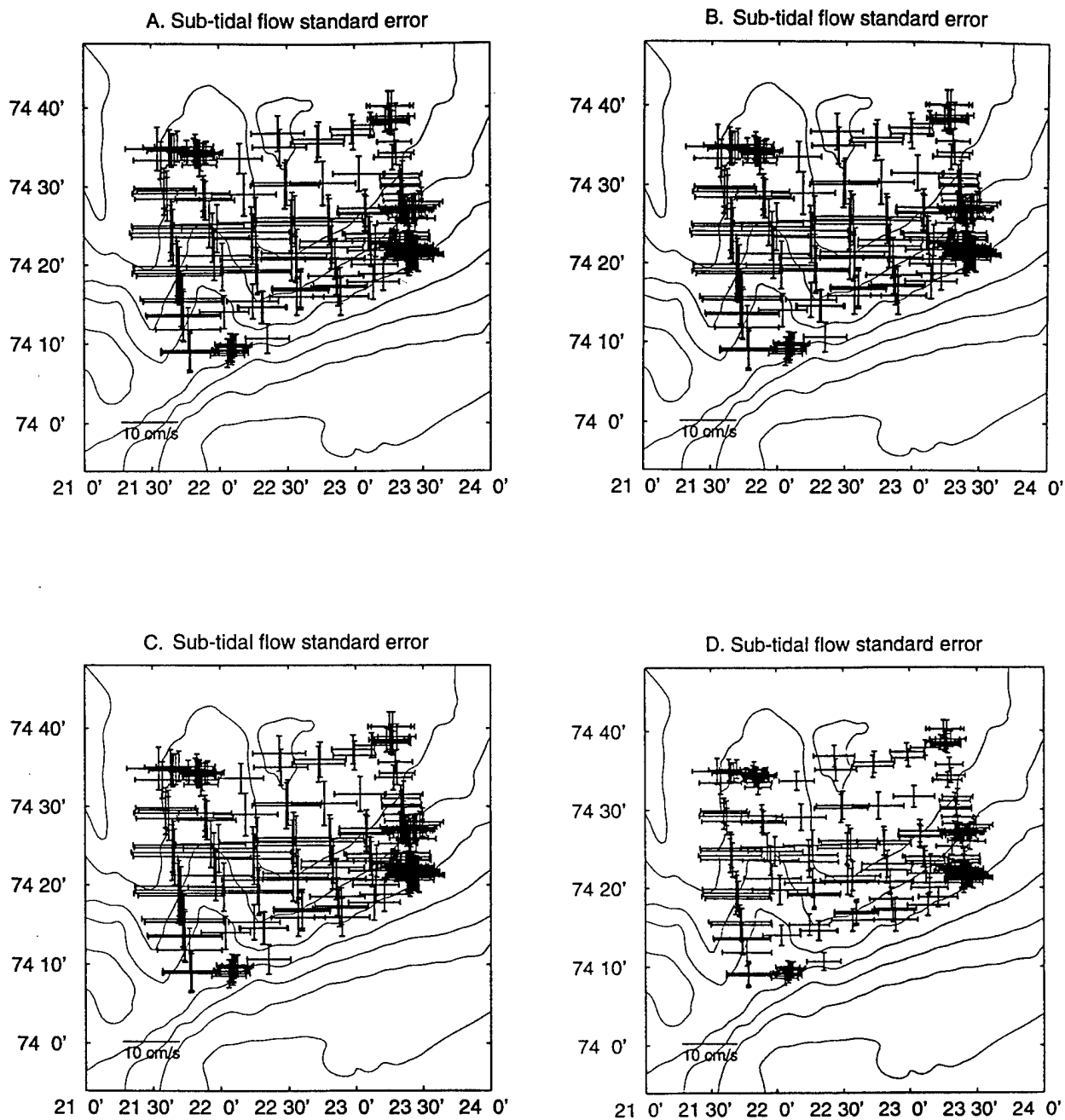


Figure 43: Standard errors of the sub-tidal flow from the combined ADCP/current meter data set at (A) 20 m depth, (B) 50 m depth, (C) 80 m depth, and (D) three depth average.

Acknowledgments

The 1992 field experiment was planned and implemented by the BSPF group: RHB, C. S. Chiu, J. F. Lynch, J. H. Miller, R. D. Muench, and AJP. J. Kemp designed the moorings, supervised mooring deployment and recovery operations, and performed the ADCP installation on the BARTLETT with assistance from J. Bouthiette. N. Galbraith assisted with ADCP data processing. The tide removal algorithm was graciously provided by J. Candela. A. R. Parsons processed the hydrographic and current meter data, generated the composite bathymetry, and contributed to the tidal analyses. The successful field operations would not have been possible without the cooperation and assistance of the Captain and crew of the USNS BARTLETT. This work was funded by Code 322 HL of the Office of Naval Research under Grant Number N00014-90-J-1359.

References

- Candela, J., R. C. Beardsley and R. Limeburner, 1992. Separation of tidal and sub-tidal currents in ship-mounted Acoustic Doppler Current Profiler observations. *J. Geophys. Res.*, 97(C1), 769- 788.
- Joyce, T. M., 1989. On in situ "calibration" of shipboard ADCP's. *J. Atmos. Ocean. Technol.*, 6, 169-172.
- Kowalik, Z. and Proshutinsky, A. Y., 1994. The Arctic Ocean Tides. The Polar Oceans and Their Role in Shaping the Global Environment, Geophysical Monograph 85, American Geophysical Union, 137-158.
- Loeng, H., 1991. Features of the physical oceanographic conditions of the Barents Sea. Pp. 5-18 in Sakshaug, E., Hopkins, C. C. E. and Oritsland, N. A. (eds.): Proceedings of the Pro Mare Symposium on Polar Marine Ecology, Trondheim, 12-16 May, 1990. *Polar Research*, 10(1).
- Parsons, A. R., R. H. Bourke, R. D. Muench, C.-S. Chiu, J. F. Lynch, J. H. Miller, A. J. Plueddemann, and R. Pawlowicz, 1994: The Barents Sea Polar Front in Summer. Submitted to *J. Geophys. Res.-Oceans*.
- Pollard, R. and J. Read, 1989. A Method for Calibrating Shipmounted Acoustic Doppler Profilers and the Limitations of Gyro Compasses. *J. Atmos. Ocean. Technol.*, 6(6), 859-865.
- RD Instruments, 1989. Acoustic Doppler Current Profilers Principles of Operation: A Practical Primer. 36 pp.

DOCUMENT LIBRARY

Distribution List for Technical Report Exchange - May 5, 1994

University of California, San Diego
SIO Library 0175C (TRC)
9500 Gilman Drive
La Jolla, CA 92093-0175

Hancock Library of Biology & Oceanography
Alan Hancock Laboratory
University of Southern California
University Park
Los Angeles, CA 90089-0371

Gifts & Exchanges
Library
Bedford Institute of Oceanography
P.O. Box 1006
Dartmouth, NS, B2Y 4A2, CANADA

Commander
International Ice Patrol
1082 Shennecossett Road
Groton, CT 06340-6095

NOAA/EDIS Miami Library Center
4301 Rickenbacker Causeway
Miami, FL 33149

Library
Skidaway Institute of Oceanography
10 Ocean Science Circle
Savannah, GA 31411

Institute of Geophysics
University of Hawaii
Library Room 252
2525 Correa Road
Honolulu, HI 96822

Marine Resources Information Center
Building E38-320
MIT
Cambridge, MA 02139

Library
Lamont-Doherty Geological Observatory
Columbia University
Palisades, NY 10964

Library
Serials Department
Oregon State University
Corvallis, OR 97331

Pell Marine Science Library
University of Rhode Island
Narragansett Bay Campus
Narragansett, RI 02882

Working Collection
Texas A&M University
Dept. of Oceanography
College Station, TX 77843

Fisheries-Oceanography Library
151 Oceanography Teaching Bldg.
University of Washington
Seattle, WA 98195

Library
R.S.M.A.S.
University of Miami
4600 Rickenbacker Causeway
Miami, FL 33149

Maury Oceanographic Library
Naval Oceanographic Office
Building 1003 South
1002 Balch Blvd.
Stennis Space Center, MS 39522-5001

Library
Institute of Ocean Sciences
P.O. Box 6000
Sidney, B.C. V8L 4B2
CANADA

Library
Institute of Oceanographic Sciences
Deacon Laboratory
Wormley, Godalming
Surrey GU8 5UB
UNITED KINGDOM

The Librarian
CSIRO Marine Laboratories
G.P.O. Box 1538
Hobart, Tasmania
AUSTRALIA 7001

Library
Proudman Oceanographic Laboratory
Bidston Observatory
Birkenhead
Merseyside L43 7 RA
UNITED KINGDOM

IFREMER
Centre de Brest
Service Documentation - Publications
BP 70 29280 PLOUZANE
FRANCE